GAS HYDRATE IN FINE-GRAINED SEDIMENTS

— LABORATORY STUDIES AND COUPLED PROCESSES ANALYSES

A Thesis
Presented to
The Academic Faculty

by

Liang Lei

In Partial Fulfillment
of the Requirements for the Degree
Doctor of Philosophy in the
School of Civil and Environmental Engineering

Georgia Institute of Technology
May 2017

GAS HYDRATE IN FINE-GRAINED SEDIMENTS

— LABORATORY STUDIES AND COUPLED PROCESSES ANALYSES

Approved by:

Dr. J. Carlos Santamarina, Advisor
School of Civil and Environmental Engineering
Georgia Institute of Technology

Dr. Susan E. Burns
School of Civil and Environmental Engineering
Georgia Institute of Technology

Dr. J. David Frost
School of Civil and Environmental Engineering
Georgia Institute of Technology

Dr. Daniel Goldman
School of Physics
Georgia Institute of Technology

Dr. J. Marcelo Sánchez
Department of Civil Engineering
Texas A&M University

Date Approved: 12/14/2016

ACKNOWLEDGEMENTS

I would like to thank my advisor, Dr. J. Carlos Santamarina for the great guidance and support on not just research. His enthusiasm towards research and life, curiosity on knowledge, insights into physical world and passion on teaching and mentoring have guided me into a different world. The past four and a half years have been and will be a great fortune in my life. It was my privilege to meet and learn from him.

I am grateful to my thesis committee members, Dr. Susan E. Burns, Dr. Marcelo Javier Sánchez Castilla, Dr. J. David Frost, and Dr. Daniel Goldman, for insightful comments and constructive suggestions. Special thanks go to Dr. J. David Frost and Dr. Sheng Dai for the warm support.

Early developments in this study were the result of a rich research collaboration between the author and Seth Mallett, a fellow Graduate Research Assistant supported on the same DOE contract at the time. This collaboration was particularly valuable in enabling the design, fabrication, calibration and validation of the micro-focus Cone Beam Computed Tomography system reported in Chapter 2: an iterative design process led to a system which optimized the relationship between systems performance constraints and available system components to produce an affordable safety-centered fully-functional system.

Pleasant discussions and interactions with past and current members and visitors of Particulate Media Research Laboratory and Energy Geo-Engineering Laboratory highly enriched my life: Josbel Cordero Arias, Stefanos Athanasopoulos, Nicolas Augsburger, Minsu Cha, Song-hun Chong, Xunchang Fei, Dante Fratta, Adrian V.

Garcia, Anant Ghumare, Ahmed Hafez, Farizal Hakiki, Enrique Asanza Izquierdo, Junbong Jang, Seunghee Kim, Qi Liu, Cuiying Lu, Chuangxin Lyu, Clara Modenesi, Efhymios Papadopoulos, Junghee Park, Cesar Pasten, Andika Perbawa, Rached Rached, Marisol Salva Ramirez, Xingwei Ren, Miriam Martin-Ruiz, Shahrzad Roshahkhah, Yuanjie Shen, Zhonghao Sun, Marco Terzariol, Aswathy Sivaram, Geralds Useche, Lucio Gerardo Cruz Velasco, Taesup Yun, Alejandro Cardona Ramirez. Especially, I sincerely appreciate the generous advice from Gabrielle E. Abelskamp and Dr. Hosung Shin.

The unconditional love from my parents and family accompanies me every moment. Especially, I could not have accomplished my work without the complete love and steady support from my dear wife, Lingli Pan.

TABLE OF CONTENTS

LIST OF TABLES

LIST OF FIGURES

Page

SUMMARY

Methane hydrates in marine and permafrost sediments are potential energy resources (Boswell 2009; Collett 2002). The total amount of carbon trapped in gas hydrate exceeds the sum of all other forms of conventional fossil fuels (Kvenvolden 1988). However, the dissociation of methane hydrates can accelerate climate change (Archer 2007; Ruppel and Pohlman 2008), cause ground subsidence and trigger seafloor landslides (Grozic 2010; Hornbach et al. 2007). Over 90% percent of the global hydrate mass is found in fine-grained sediments (Boswell and Collett 2008). To date, there has been minimal research in hydrate-bearing fine-grained sediments.

The central themes of this research are the fundamental understanding of hydrate formation and dissociation in fine-grained sediments, and the associated physical processes. The discussion ranges from the particle-scale to the macro-scale. This includes the shift in the phase boundary associated to curvature effects, the particle-displacive morphology, diffusion induced Leisegang bands and two hydrate formation patterns in gas-filled openings. We develop laboratory techniques that emulate natural gas hydrate formations. The experimental results illustrate the hydrate formation process via different strategies that aim to accelerate the gas supply to the hydrate formation front. In addition, simulations of physical properties of hydrate-bearing fine-grained sediments address the segregated morphology of hydrates in fine-grained sediments and the change in physical properties induced by cryogenic suction. We explore potential methods to produce gas from hydrate-bearing fine-grained sediments. The analyses on gas production centers on the technical viability of depressurization, thermal stimulation and chemical stimulation.

CHAPTER 1

INTRODUCTION

1.1 Introduction

Methane hydrates in marine and permafrost sediments are potential energy resources (Boswell 2009; Collett 2002). The total amount of carbon trapped in gas hydrate exceeds the sum of all other forms of conventional fossil fuels (Kvenvolden 1988). However, the dissociation of methane hydrates can accelerate climate change (Archer 2007; Ruppel and Pohlman 2008), cause ground subsidence and trigger seafloor landslides (Grozic 2010; Hornbach et al. 2007; Kvalstad et al. 2005). Hydrate-bearing sands are considered most favorable for future gas production (Boswell 2009; Boswell and Collett 2006; Boswell and Collett 2011). However, over 90% percent of the global hydrate mass is found in fine-grained sediments (Boswell and Collett 2006). To date, there has been minimal research in hydrate-bearing fine-grained sediments.

Fine-grained sediments inherently imply small pore sizes, high specific surface and low hydraulic conductivity. Consequently, the contribution of advection to methane transport in fine-grained sediments is very low, and diffusion is extremely slow (Xu and Ruppel 1999). Capillary effects are pronounced in small pores. This hinders both crystal formation and gas flow. In addition, the compressibility of fine-grained sediments implies high volume changes when subject to variations in effective stress, cryogenic suction or gas pressure.

This thesis explores the fundamental understanding of hydrate formation in fine-grained sediments and ensuing morphology. We develop laboratory techniques that emulate natural formations, utilize analytical tools and numerical models to predict physical properties, and explore gas production alternatives to recover methane from hydrate-bearing clayey sediments.

1.2 Thesis Organization

The central themes of this research are the fundamental understanding of hydrate formation and dissociation in fine-grained sediments, and the associated physical processes.

Chapter 2 focuses on the design and assembly of a customized micro-focus X-ray tomographic system to study gas hydrates under the high-pressure and low-temperature conditions. This chapter was developed in collaboration with Seth Mallett.

Chapter 3 analyzes the fundamental physics of hydrate formation in fine-grained sediments. The discussion ranges from the particle-scale to the macro-scale. This includes the shift in the phase boundary associated to curvature effects, the particle-displacive morphology, diffusion induced Leisegang bands and two hydrate formation patterns in gas-filled openings.

Chapter 4 documents and analyzes a laboratory experimental study on hydrate formation in fine-grained sediments. The results illustrate the hydrate formation process via different strategies that aim to accelerate the gas supply to the hydrate formation front.

Chapter 5 investigates the physical properties of hydrate-bearing fine-grained sediments. Simulations address the segregated morphology of hydrates in fine-grained sediments and the change in physical properties induced by cryogenic suction.

Chapter 6 explores potential methods to produce gas from hydrate-bearing fine-grained sediments. The analyses centers on the technical viability of depressurization, thermal stimulation and chemical stimulation.

Chapter 7 summarizes salient conclusions from this work.

CHAPTER 2

DESIGN OF A HIGH-RESOLUTION CONE BEAM X-RAY TOMOGRAPHER FOR GEOTECHNICAL APPLICATIONS

2.1 Introduction

The discovery of X-rays in 1895 (Wilhelm Röntgen, 1845-1923) stimulated wide spread innovation, largely driven by medical applications. More recent developments in radiography equipment and software have included micro-focus tubes, digital detectors and 3D-scanning techniques (Kak and Slaney 1988; Kalender 2006; Prince and Links 2006; Rangayyan 2004). The development of X-ray computed tomography CT by Hounsfield and Cormack led to the Nobel Prize award for Physiology or Medicine in 1979.

The geoscience field began to embrace radiography in the 1960s when scientists began scanning sediment cores (Baker and Friedman 1969; Bouma 1964; Calvert and Veevers 1962; Hamblin 1962). Roscoe (1970) mapped strain localization and shear band formation in soils with the use of 2-D X-ray technology. Radiography allows for high frame rate imaging of dynamic geo-processes.

X-ray computed tomography provides 3D images of the specimen and its evolution over time. However, it remains under-utilized in geotechnical engineering due to high initial costs and potential radiation-related safety concerns (Viggiani et al. 2015). Arising geotechnical challenges frequently involve abnormal temperatures, high pressures, high effective stress, mixed fluid conditions (oil, gas and brine) and phase transformations (gas to liquid, and liquid to solid). X-ray CT offers exceptional opportunities to gain unprecedented insight into these processes; however, the system must be designed to accommodate geotechnical test requirements. Therefore, there is a need for customized and economically viable X-ray CT systems in geo-engineering and science.

This chapter provides the knowledge base required for X-ray tomography and presents the step-by step design of a versatile and economically accessible CT scanner.

2.2 X-ray Physics

X-rays traverse soils and rocks. Therefore, detected X-ray intensities provide information about the internal structure of geomaterials.

2.2.1 X-ray generation

X-ray beams generated from X-ray tubes typically consist of Bremsstrahlung radiation and characteristic spikes (Compton and Allison 1935; Selman and Thomas 1985). Bremsstrahlung radiation is the continuous X-rays generated when a strong electrical field scatters electrons. The energy levels are quantized and one can determine the atom type based on the characteristic X-rays. This X-ray emission occurs when an electron with sufficient energy knocks an orbital electron out of the inner electron shell, and higher energy level electrons fall in to fill the vacancy. Voltage and current in an X-ray tube determines the electrical field potential that accelerates the electrons to bombard the target material and the number of electrons that reach the target. Figure 2.1 illustrates the intensity spectrum generated by a Tungsten target when the voltage is 100 and 60 kV respectively. Emitted low-energy component is adsorbed at the window that separates the vacuum tube and the environment. Note that the X-ray beam does not display homogeneous intensities across the conical beam.

2.2.2 X-ray attenuation

X-rays attenuate as they traverse a material. The attenuation of low-energy X-rays (<1 MeV) results from photoelectric effects and both Rayleigh and Compton scattering effects (Jaeger 1968). Rayleigh scattering is often neglected (Alvarez and Macovski 1976; Rebuffel and Dinten 2007). Then, the total mass attenuation coefficient μ_m combines the photoelectric effect τ and the Compton scattering σ (applies to photon energy E<500KeV and the atomic number Z≤29):

$$\mu_m = \tau + \sigma \approx \alpha Z^{4.5} E^{-3} + \beta Z E^{-1} \tag{2.1}$$

where α and β are constants.

The total attenuation coefficient is a function of both the material type and the photon energy level. The photoelectric effect dominates when the atomic number is high and the photon energy is low. The total attenuation coefficient in the Compton scattering dominated zone is approximately proportional to the material density. The electron number to mass number ratio is approximately 1:2 for most atoms except hydrogen. Therefore, the mass density of the material is proportional to the electron density that dominates the Compton scattering effect. Density logging of geological formations utilizes this relationship (Gluyas and Swarbrick 2013). By contrast, the atomic number of the material determines the total attenuation coefficient in the photoelectric effect dominated zone.

The intensity of the X-ray beam is the integral of the number of photons at a particular energy level. The intensity I attenuates exponentially along the travel path. Beer's Law describes the change in the X-ray intensity of a narrow, mono-energetic beam in a homogeneous medium,

$$I = I_0 \cdot \exp\left(-\int \mu(s) ds\right) \tag{2.2}$$

where I_0 is the initial intensity, μ is the linear attenuation coefficient, and s is the path length. The linear attenuation coefficient μ is a function of the mass attenuation coefficient μ_m and the density ρ, $\mu = \rho \times \mu_m$. Figures 2.2a and 2.2b show the linear attenuation coefficient as a function of photon energy for common materials found in geotechnical engineering and used to build the high-pressure chamber and X-ray shield (see NIST database for a comprehensive list (Berger 2010)). X-ray beams generated from X-ray tubes are polychromatic; it follows from Figure 2 that X-ray components with lower energy levels attenuate faster than components with higher energy levels.

2.2.3 X-ray detection

The scintillation material in the detector absorbs the incoming X-ray photons and emits visible lights. The detector then transforms the light intensity into a greyscale digital signal. Quantum detection efficiency QDE refers to the detector efficiency relative to an ideal detector. QDE varies with photon energy level. Therefore, the grayscale value is an integral of the X-ray beam spectrum and different energy spectra could result in the same grayscale value.

2.3 Hardware System Design

Table 2.1 provides three X-ray system configurations for different cost levels. Figure 2.3 illustrates the micro-focus Cone Beam Computed Tomography CBCT system designed and built for this study; it falls in the intermediate cost category. The selection of the X-ray CT system components starts with decisions related to specimen size, material type, desired image resolution and budget. The iterative design process involves various trade-offs between constrains and available system components. Table 2.2 lists parameters associated with system components and achievable specifications of the overall system. The design process is summarized next.

2.3.1 Geometry design and resolution

Figure 2.4a sketches the typical geometrical relationships in a CBCT system. These relationships provide a basis for the analyses below.

Rotation precision. The rotation precision δ is critical to resolution and image quality (Figure 2.4b). The periphery error on the edge of the object *ds* is the product of rotation error δ and the radius of the object *r*, $ds=r\times\delta$. Then the induced geometrical shift on the detector *dL* satisfies,

$$\frac{ds}{dL}=\frac{SOD-r}{SDD} \tag{2.3}$$

where SOD is the source-to-object distance, and SDD is the source-to-detector distance. The geometric relationship between the object radius r and the detector length L is

$$\frac{2r}{L} = \frac{SOD}{SDD}\cos\left(\frac{\eta}{2}\right) \tag{2.4}$$

where η is the utilized beam angle. In addition, $r/SOD=\sin(\eta/2)$ and the detector length $L=M\times PS$ where M is the number of pixels across the detector, and PS is the pixel size. Let's assume that a precise rotation requires the image shift dL on the detector to be less than 1/10 of the pixel size PS, then,

$$\delta \le \frac{1}{5M}\cdot\left[\cos\left(\frac{\eta}{2}\right)\right]^{-1}\cdot\left(1-\sin\left(\frac{\eta}{2}\right)\right) \tag{2.5}$$

If the beam angle η is small, the accuracy of the rotary stage is inversely proportional to the number of pixels across the detector:

$$\delta \le \frac{1}{5M} \tag{2.6}$$

Therefore, the accuracy of the rotary stage requires $\delta\le 0.011°$ in the case of a detector with 1024×1024 pixels.

Focal spot size and geometry resolution. Reconstruction algorithms assume a point. The focal spot finite size results in blurred images on penumbra effect (Figure 2.4c). The geometric resolution limit λ is related to the focal spot size FS and the pixel size PS and the relative position of the object χ=SDD/SOD (Yester and Barnes 1977),

$$\lambda = \frac{\sqrt{PS^2 + \left[FS(\chi-1)\right]^2}}{\chi} \tag{2.4}$$

When the object is close to the focal spot, $\chi\to\infty$ and the geometric resolution λ approaches the focal spot size FS. By contrast, when the object is close to the detector χ=1, the pixel size PS dominates the geometric resolution $\lambda\to PS$. This analysis provides the upper limits of the resolution (there are other factors that hinder resolution, such as the rotary precision, mechanical deflection, and vibrations). The resolution limit for the

X-ray system in this study is 127μm when the object is close to the detector and 7.5μm when the object is closed to the X-ray source window.

2.3.2 Other factors

Specimen characteristics. The smallest specimen size that an X-ray CT system can resolve depends on the spot-to-window spacing SWS inside the source, and the source to detector distance SDD (Figure 2.4a). On the other hand, the detector size limits the maximum specimen size (d<L). The specimen material and thickness determine the required voltage and current. In addition, the total weight of the specimen and the specimen holder/cell must not exceed the load capacity of the rotary stage.

Scan time duration. The total scan time must be much shorter than any internal time scale in the specimen. The minimum scan time of an X-ray system depends on the maximum speed of the rotary stage, and the frame rate of the detector. A fast frame rate relies on high voltage and signal intensity to attain adequate signal-to-noise ratio in projection images, however contrast is sacrificed in tomographic inversions.

2.3.3 Safety and operational procedures

The total effective dose a person can receive is limited to five rems per year (Federal Nuclear Regulatory Commission). Table 2.2 summarizes the consequences of exposure to X-ray radiation to the human body.

Appropriate safety equipment and operational procedures are critical to minimize radiation exposure. Lead is a common shield component due to its large attenuation coefficient (Figure 2.2). The shield thickness should limit the emitted radiation to less than 0.5 miliRoentgen per hour at any point five centimeters outside the external surface of the shield' (Chalmers 2005; Food and Administration 2015). A dual interlock switch on the cabinet door prevents the operation of the X-ray source when the external door opens. In addition, an emergency switch is mounted outside the shielded area.

Standard operating procedures must incorporate, 1) mandatory X-ray safety training for all the operators, 2) operational log books, 3) emergency response plan, 4) periodic assessment of radiation leak, 5) dosimeter badges on all users whenever the X-ray is in use, and quarterly radiation assessment of badges to track the operators' accumulated radiation dose, and 6) clear signage of the radiation source in the area.

2.4 Software — Reconstruction and Visualization

2.4.1 Tomography — inverse problem solving

The 3D structure of a soil or rock specimen is 'reconstructed' from individual X-ray projections obtained at multiple angles. The Feldkamp, Davis and Kress FDK inversion method provides the foundation for the most widely used reconstruction methods in CBCT systems (Feldkamp et al. 1984). FDK evolves from 2-dimensional fan-beam reconstruction theory and belongs to the family of filtered back-projection algorithms. The radiology literature contains numerous adaptations of this technique for specific applications (Grass et al. 2000; Li et al. 2011). Note that the method is only strictly accurate for voxels within the central plane.

CT imaging starts with high resolution and signal-to-noise ratio data and requires efficient reconstruction algorithms that account for artifacts. Open-source software for tomographic reconstruction include OSCaR (Rezvani et al. 2007), ImageJ (Rasband 1997) and the Reconstruction ToolKit (Rit et al. 2014). Commercially available software such as VolumeGraphics and Octopus are more time and memory efficient, and can correct for beam hardening and geometric artifacts.

2.4.2 Image processing and visualization

The final step, visualization, is equally critical. Color thresholding is the most common "trick" and helps produce high contrast reconstructions with clear topological features.

Image J is a powerful public-domain, Java-based image processing and visualization software (Rasband 1997). A large variety of complementary algorithms and functions contributed from developers worldwide are available online. The customers can also develop their own functions. Commercial available visualization software includes VGstudio MAX and VTK.

2.4.3 Artifacts and corrections

Artifacts are ubiquitous to X-ray CT images. Some are deeply rooted in the physical limitations and geometrical setups, whereas others are due to the reconstruction algorithm.

Beam-hardening artifact. Edges appear brighter than the center in reconstructed column-shaped specimens (Figure 2.5). The underlying "beam-hardening" effect is inherent in CT systems with polychromatic X-ray sources: as shown in Figure 2.2, the low energy spectrum attenuates faster than the high-energy spectrum. Therefore, the low energy spectrum loses the majority of its energy within a shorter path, and the beam is hardened while travelling through the scanned object due to the increasing proportion of high energy spectrum. The attenuation value inverted for each voxel is an average of the attenuation experienced by various spectral components. Alternatively, the short path for the X-ray beam in the edge appears to be more efficient in attenuating the X-rays. Consequently, short paths render relative higher attenuation coefficients in comparison to long paths. Theoretically, this beam-hardening effect does not occur if the X-ray beam is monochromatic. The scintillation material of the detector is more sensitive to the soft part of the X-ray beam, which increases the beam hardening effect (Mengesha and Valentine 2002).

Ring artifact. Ring artifacts result from inadequate calibration and damaged cells in the detector that consistently yield high or low values (Figure 2.6). Therefore, a careful detector calibration and a detailed documentation of the bad points on the detector are needed to prevention and correct for ring artifacts. The ring in the reconstructed image appears as a line in the polar transformation of the image. Therefore, a low-pass frequency filter applied to the polar image corrects ring artifacts.

Metal artifact. This is commonly known as ‘starburst’ and metal strike artifacts (Figure 2.6). The artifact appears when the sediment contains highly attenuating inclusions. Thermocouples buried in sediments to monitor thermal effects cause these strikes.

Partial volume effect. The attenuation coefficient of features smaller than the voxel size is averaged with other voxel components. This may bias image interpretation. For example, the edge of an aluminum chamber wall could average with the attenuation of air to yield a fictitious water layer artifact. Therefore, the smallest distinguishable feature in an X-ray image should occupy at least 2×2 pixels, or 2×2×2 voxels. This effect creates problems when separating the different features of an object.

2.5 Operation

Each component of the CT system includes with its own operation software. While one can operate each hardware component separately, a single interface that coordinates all software increases system efficiency (See (Ionita et al. 2008) Ionita et al., 2008 for an open-source Labview interface to operate micro-focus CBCT systems).

2.5.1 Voltage and current

There are several guidelines that assist with the determination of optimum voltage and current. Low voltage increases the image contrast but worsens the beam-hardening artifact. High voltage increases the ability of the X-ray beam to penetrate materials (Figure 2.2) but decreases the contrast. The increase in voltage and/or current increase the focal spot size and signal-to-noise ratio in projection images but decrease the geometrical resolution (Equation 2.5). The voltage and current optimization process frequently involves an element of trial and error.

2.5.2 Filters and spectra design

Bowtie-shaped filter. The shadow of the scanned object does not completely cover the detector, and parts of the detector receive the full energy spectrum from the X-ray source.

Bowtie filters resolve saturation issues, protects the detector from the radiation damage (Figure 2.4a), and reduce the beam-hardening artifact.

The use of a filter decreases the overall intensity of the beam, and absorbs a larger portion of the soft X-rays in comparison to the hard. Thus, the scattering and beam hardening artifacts simultaneously reduce. The low energy component is more sensitive to small density changes. For low contrast or small sized samples, filters must be thin enough to allow for the low energy X-rays to distinguish between the minute density changes of the sample material.

Spectra design. There is a sudden increase in the attenuation coefficient of materials with high atomic numbers when the photon energy is close to its characteristic energy. X-ray photons with higher energy are able to expel K-shell electrons. This is an additional mechanism of the material to attenuate the photons. Figure 2.5a demonstrates the attenuation coefficient of Holmium as a function of photon energy. The sudden increase in the attenuation coefficient enables the Holmium filter to efficiently absorb the photons with energy higher than 55.62 KeV. Figure 2.5b illustrates the X-ray spectrum that passes through the filter. The use of low atomic number materials as high-pass filters and high atomic number materials as low-pass filters enables the design of the X-ray spectra.

2.5.3 Frame rate and stacking

A low frame rate yields a better quality image. The signal-to-noise ratio decreases with the increase in frame rate. Exposure time increase or stacking removes the random noise but inherently increases scan time. Alternatively, high frame rate at higher voltage or current compensate for the loss of signal intensity but hinders contrast and resolution. Flat panel detectors usually provide a binning feature that allows the detector to work at a higher frame rate with binned pixel size. Long exposure times subjects to object movements that include system vibration, continuous specimen rotation, and biological movement thus apply to time-invariant system. In addition, the detector is very sensitive to variations in temperature.

2.5.4 Geometry calibration

Geometrical calibration for rotation axis tilt angle and offset, source to object distance and source to detector distance is critical to the reconstruction quality (Cho et al. 2005; Johnston et al. 2008; Panetta et al. 2008; Yang et al. 2006). Common methods use steel balls to obtain their ellipsoidal traces on the detector. The fitted parameters that define the ellipses are then implemented to back calculate the geometrical calibration parameters.

2.5.5 CT generated heat

The maximum voltage and current determine the power of the X-ray source. This power for a normal X-ray tube can exceed 200 watts; however, the power for a micro-focus X-ray tube is often less than 20 watts. Less than 1% of the energy transfers to the X-ray beam; the rest of the power is released as heat. The scanned object absorbs part of the transmitted X-ray beam energy, and the rest reaches the detector. Consequently, the power absorbed per volume of the specimen is very small and can be disregarded in the overall thermal balance in most cases. However, the thermal change within the shield can be pronounced and proper cooling may be required.

2.5.6 Life span and reliability

The life span of the X-ray source and detector is critical to economical and sustainable CT system. Environmental conditions such as high humidity and dust harm the lifespan of both the source and detector. Usage factors that damage the source include the consistent use of high voltages, repeatedly switching on and off, and numbers of warmup cycles. In addition, the detector subjects to radiation damage, especially at high voltage. Therefore, bowtie shaped filters during the scan and thick lead X-ray shutters in the warmup process improves the lifespan of the detector.

2.6 Applications and Advances in Geotechnical Engineering

Table 2.4 lists the properties and processes associated geotechnical engineering studied in the literature.

2.6.1 X-ray and high-pressure chamber design

X-ray transparent chambers use low density and small atomic number Z materials such as beryllium (Z=4), aluminum (Z=13), aluminum-beryllium alloy and carbon fiber (Z=6). Beryllium has a very low attenuation coefficient due to its low density and small atomic number, *Z=4*. The attenuation coefficient of beryllium is close to that of soil, and therefore, the use of beryllium lessens beam hardening and metal artifacts; however, beryllium is brittle under low temperatures. Aluminum has a higher attenuation coefficient than beryllium (Figure 2.2), yet its higher strength enables a thinner chamber wall design; furthermore, aluminum is relatively ductile even at low temperatures. The aluminum-beryllium alloy lies between the two. Hybrid cells use carbon fiber walls and metal caps to have feedthroughs.

2.6.2 Visualization of the inner 3D structure

A very common aim of the CT technique is to obtain images of the inner 3D structure without destruction of the specimen. Figure 2.8a-2.8d illustrates the structure of selected objects scanned by the micro-CT system in this study. The thresholding and segmentation then allow for the construction of 3D volume or surface models of specimens (Figure 2.8e and 2.8f).

2.6.3 Grain and fluid tracer

Roscoe (1970) developed the Grain Tracer technique that utilizes lead shots distributed in the soil. The shadow of the high-density lead shots traces the displacement and enables the interpretation of strain. Fluid tracer techniques date back to the invention of cerebral angiography by Egas Moniz in 1927. Iodine-based salt is the common

additive used in the technique that increases the attenuation coefficient of the tracer fluid, due to iodine's high atomic number (Z=53) induced significant photoelectric effect. Researchers use a mixture of potassium iodide and urografin that has the same viscosity as water to characterize the water flow in porous rock(Fukahori et al. 2010; Fukahori et al. 2006).

2.6.4 Particle-tracking in triaxle test

Recent studies that integrate X-ray CT scanning systems with triaxial testing equipment has led to particle-scale research of shear strains and the associated localization effects (Charalampidou et al. 2011; Charalampidou et al. 2010; Lenoir et al. 2004; Viggiani et al. 2004). This uses high resolution image correlations between the time-lapse 3D structures captured during different steps of the triaxle test. The motion, rotation, and breakage of each particle, and the slip between particles provide the particle-scale detail and their relationships to the global stress-strain behavior (Alikarami et al. 2015; Kawamoto et al. 2016; Lim et al. 2016; Salvatore et al. 2016).

2.6.5 Dual energy radiography and CT

Alvarez and Macovski (1976) were the first researchers to publish results on the concept of dual energy X-ray techniques. This technique utilizes dual energy detectors or two successive scans with two different photon energy levels through the design of X-ray spectra (Figure 2.9). Therefore, the doubled information allows for the decoupling of the photoelectric effect and Compton scattering. Consequently, the determination of the effective atomic number and material density is achievable with careful calibration (Remeysen and Swennen 2006; Van Geet et al. 2000). In addition, the use of dual energy techniques can effectively correct beam hardening in CT reconstruction (Rebuffel and Dinten 2007).

2.6.6 Synchrotron X-ray diffraction

X-ray photons follow Bragg's law, when the X-ray beam is directed through substances. The detection of the diffraction patterns can reveal the structure of the crystal or amorphous material (Lester and Aborn (1925), Nobel Prize). When the crystal structure varies with changes in pressure, temperature or stress, the diffraction pattern reflects this change. Consequently, the interpretation of the diffraction pattern of well-calibrated crystals can provide data on their state. Note that the direct measurement of this pattern is the volume-averaged lattice strain. The interpretation of the strain to stress, pressure, and temperature relies on the constitutive model. Researchers that use this technique are able to determine the strain tensor of silica sand particles in single columns (Alshibli et al. 2013), refer residual stress in the material (Hauk 1997), and characterize stress distribution in granular materials (Hall et al. 2011; Wensrich et al. 2013; Wensrich et al. 2012).

2.7 Conclusions

X-ray CT is a non-destructive testing method that provides insight into a number of geotechnical processes and phenomena. This manuscript highlighted the fundamental aspects of X-ray physics and safety, hardware selection, frame design and software options for the fabrication of an integrated X-ray CT.

Our experience with the design, fabrication and operation of such an X-ray CT system shows that:

- It is technically and economically viable for geotechnical researchers and engineers to build a fully customized X-ray CT system using readily available components. The system can be made versatile to address various geotechnical engineering needs
- X-ray CT technology provides a 3-D view of geomaterials and can be used to monitor phenomena in time. Imaging is based on attenuation contrast, which varies with mass density and power. This allows for ingenious imaging methods.

- Heat transfer directly from X-ray photons to scanned objects is negligible. However, the hardware components could result in a significant temperature increase within the shield environment and external cooling may be required.
- High pressure chambers designed for X-ray CT scans are made with high-strength, low-attenuation materials, such as carbon fiber, aluminum and copper-beryllium. The chamber size must consider the balance between X-ray transparency and experimental pressure and test-size requirements.
- Imaging biases emerge from inherent physical and mathematical intricacies. Alert users will avoid associated pitfalls. Similarly, experienced users will apply imaging tricks and post-processing techniques to remove artifacts and to enhance sought features.
- Safety is paramount. Safety relies on proper shield thickness, interlock and emergency switches, and strict operation procedures.

Table 2.1 X-ray devices for geotechnical applications by price point

Price Point		Low	Intermediate	High
Hardware	Source	OEM Cone Beam/ Microfocus	Microfocus	Microfocus/ Synchrotron/ Dual Sources
	Detector	Image Intensifier & CCD camera	Flat Panel	Flat Panel/ Multiple Detectors
	Motion control	Rotary Stage	Rotary Stage	Full - X,Y,Z, and Rotational
	Shielding	Cabinet	Cabinet	Cabinet/Room
Software	Operation	Self-built	Commercial-integrated	Commercial-integrated
	Reconstruction	Open-Source	Commercial-basic	Commercial-advanced
	Visualization	Open-Source	Commercial-basic	Commercial-advanced

Table 2.2 Parameters for components in an X-ray CT system.

Components	Parameters	Brief explanations	Affected factors
X-ray tube	Voltage V and Current C.	Capability to penetrate specimen; e.g. V=130 kV & C=500 μA → d=60cm kaolinite specimen, V=220 kV & C=1 mA → d=200cm rock specimen.	ρ_s, d_{max}, Z, t_{scan}
	Focal spot size FS	Approximately circular shaped X-ray emission spot.	λ, d_{min}
	Spot to window spacing SWS	Determines the minimum source to object distance; affects capabilities to scan small objects.	d_{min}
	X-ray beam and beam Angle θ	The open angle of the 3D conical beam; affects the geometry configuration of the overall system.	d_{max}, d_{min}
X-ray detector	Pixel size PS	Center-to center distance between adjacent pixels.	λ
	Pixel number $M \times N$	Equals the number of pixels in the projection images.	λ, d_{max}
	Pixel area	Size equals $(PS \times M) \times (PS \times N)$.	d_{max}
	Frame Rate	Analogy to shutter speed of cameras.	t_{scan}
	Energy range	Dependent on the type of scintillation material; less sensitive outside this range but not blind; should match the voltage of the X-ray source	
Rotary stage	Rotation precision	See section 2.3.1 for analysis.	λ
	Rotation speed	Maximum rotation speed.	t_{scan}
	Load capacity	Limits the overall weight on the rotary stage; varies with different configurations.	ρ_s, d_{max}

Note: ρ_s = object density, Z = representative atomic number of the object, d_{max} = maximum object diameter, d_{min} = minimum object diameter, λ = achievable system resolution, and t_{scan} = scan time.
Parameters for the system in this study: V_{max}=130 kV, C_{max}=500 μA, FS_{min}=6 μm, SWS=14 mm, θ=52°, PS=127 μm, $M \times N$=1024×1024, pixel area=130×130 mm, maximum frame rate=60 frames/second, rotation precision=0.1°, maximum speed=13.2°/s, and load capacity=20 kg.

Table 2.3 Potential damage to human bodies due to different X-ray dose ranges (Simplified from Military Medical Operations, Armed Forces Radiobiology Research Institute, 2003).

Radiation dose (rad)	Phase of syndrome	Latent-No symptoms	Manifest illness	Mortality
0-100	None	>2wk	None symptoms	None
100-200	5-50% Nausea Minimal decreased LC[a]	7-15d	Moderate leukopenia	Minimal
200-600	50-100% Nausea LC<1000 at 24h CI[b] for 6-20h	0-7d	Severe leukopenia, purpura, hemorrhage, pneumonia, hair loss after 300 rad, damage to hematopoietic and respiratory systems	Low with therapy
600-800	75-100% Nausea LC<500 at 24h CI>24h	0-2d		High
800-3000	90-100% Nausea LC decreases in hours CNS[c] function incapacitation	None	Diarrhea, fever, electrolyte disturbance, damage to GI tract and Mucosal systems	Very high
>3000	100% Nausea LC decreases in hours CNS function incapacitation	None	Convulsions, ataxia, tremor, lethargy, damage to CNS function.	Very high

[a]LC=Lymphocyte Count, [b]CI=Cognitive Impairment, [c]CNS=Central Nervous System.

Table 2.4 Properties and processes studied in the literature.

	Solid phase	Void space	Flow in porous media	Mechanical Localization
Properties and processes	Bulk density[a,b] Particle characteristics[c] Soil fabric[d]	Porosity[e,f,g] Pore structure[h] Fracture geometry[i,j] Fracture aperture distribution[k,l] Water content[m] Water retention[n] Water saturation evolution[o]	Pore structure for flow simulation[p,q] Tracer-aided flow[r,s] Fluid flow in fractures[t] Multiphase flow[u]	Shear banding and local deformation[v,w,x,y,z]

References are as follows: a, (Anderson et al. 1990); b, (Zeng et al. 1996); c, (Masad et al. 2005); d, (Wang et al. 2004); e, (Bloom et al. 2010); f, (Peyton et al. 1992); g, (Alshibli et al. 1999); h, (Zhou et al. 2012); i, (Otani and Obara 2004); j, (Montemagno and Pyrak-Nolte 1999); k, (Bertels et al. 2001); l, (Pyrak-Nolte et al. 1997); m, (Anderson and Gantzer 1989); n, (Scheel et al. 2008); o, (Schnaar and Brusseau 2006); p, (Coles et al. 1998); q, (Wildenschild et al. 2002); r, (Fukahori et al. 2010); s, (Fukahori et al. 2006); t, (Watanabe et al. 2011); u, (Kumar et al. 2010); v, (Desrues 2004);w, (Ando et al. 2012); x, (Alshibli and Sture 1999); y, (Viggiani et al. 2004); and z, (Watanabe et al. 2013).

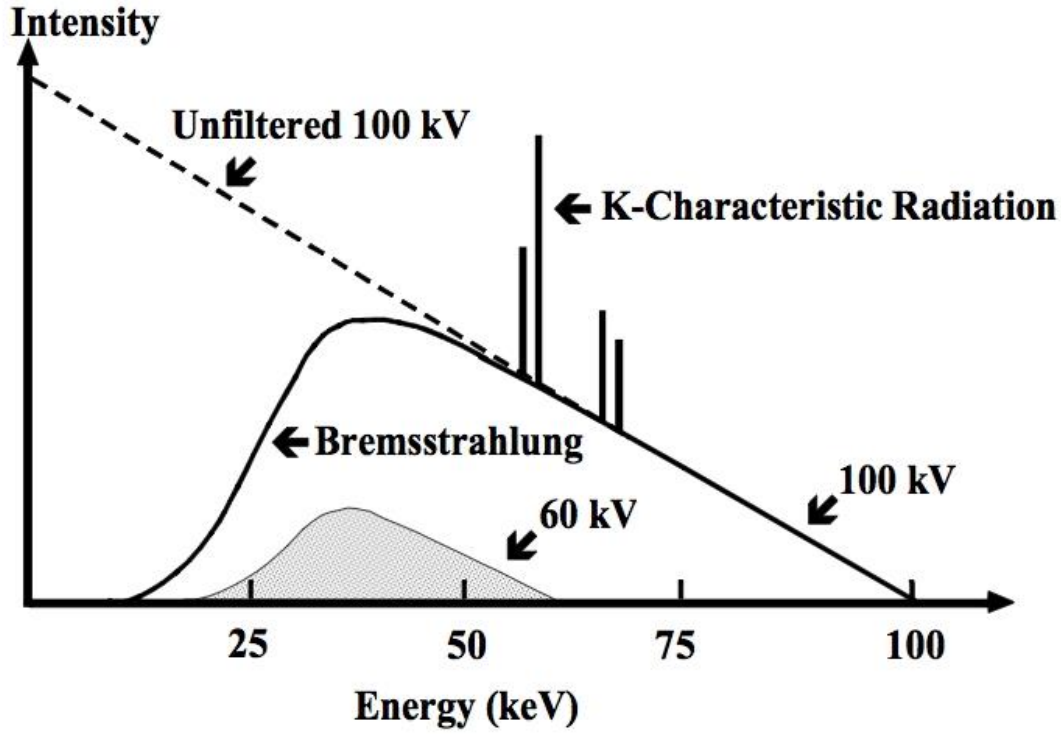

Figure 2.1 X-ray intensity spectrum of a Tungsten-target X-ray tube. (Heggie et al., 2001)

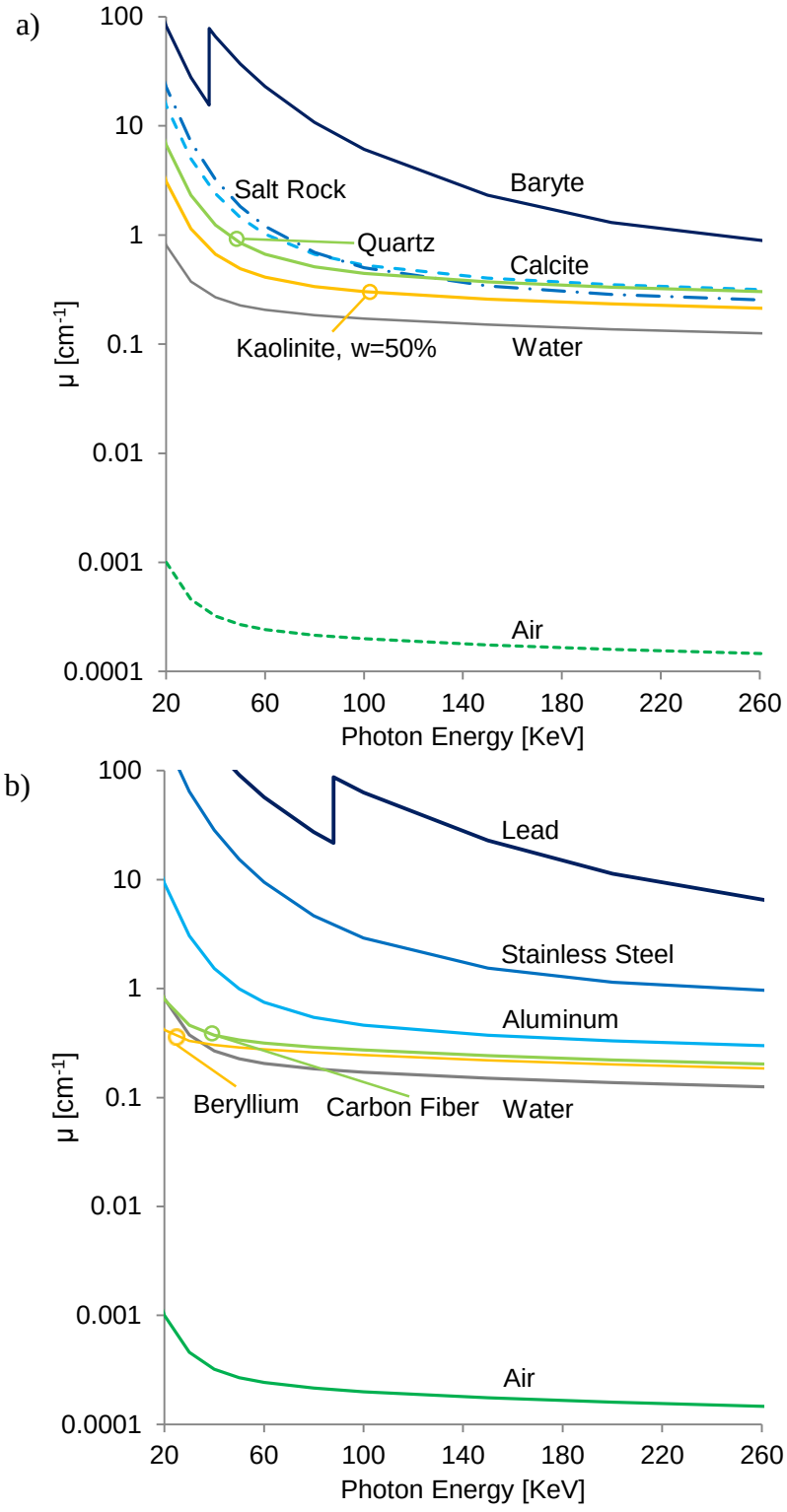

Figure 2.2 Attenuation coefficients of common materials in geotechnical engineering and high-pressure chamber design (Data from Berger et al., 2010. NIST XCOM database).

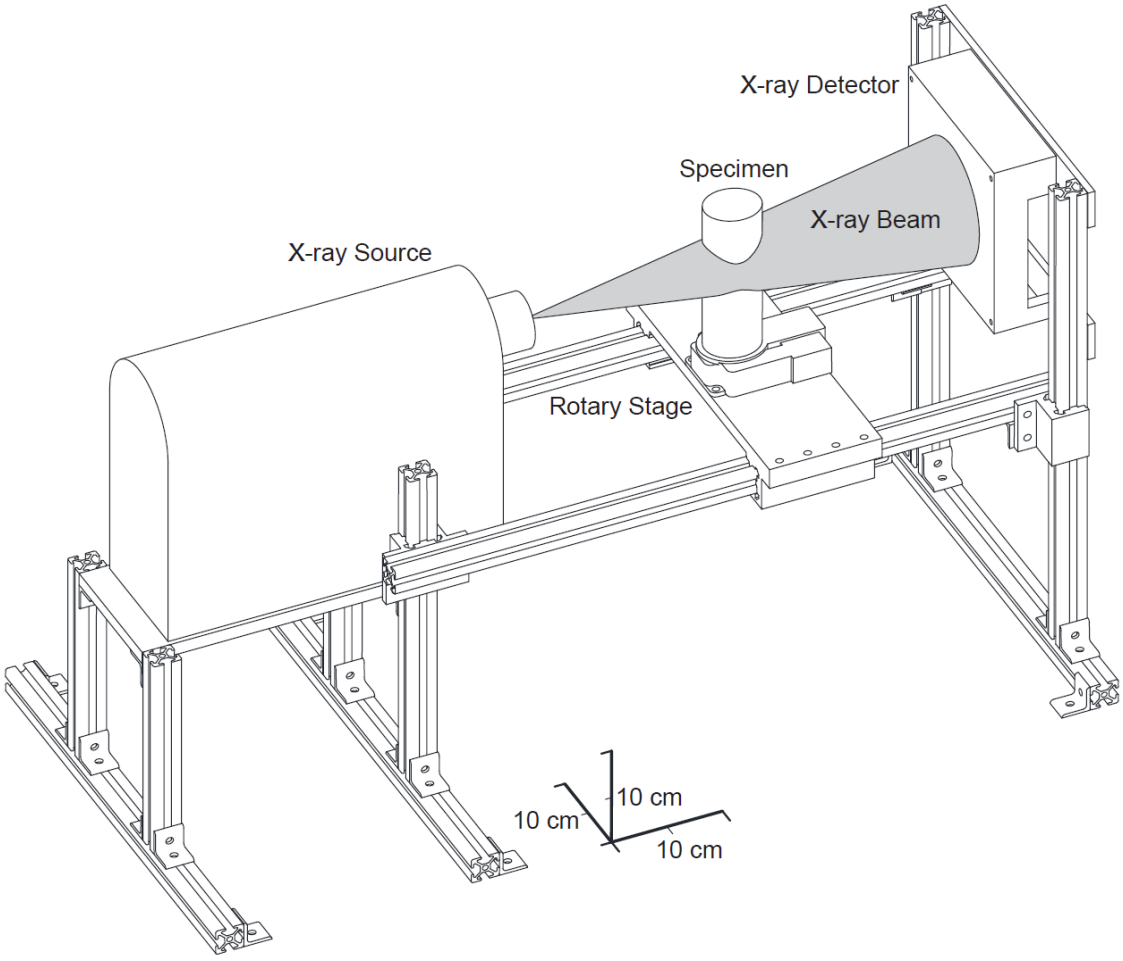

Figure 2.3 Schematic of the micro-CT system at PMRL.

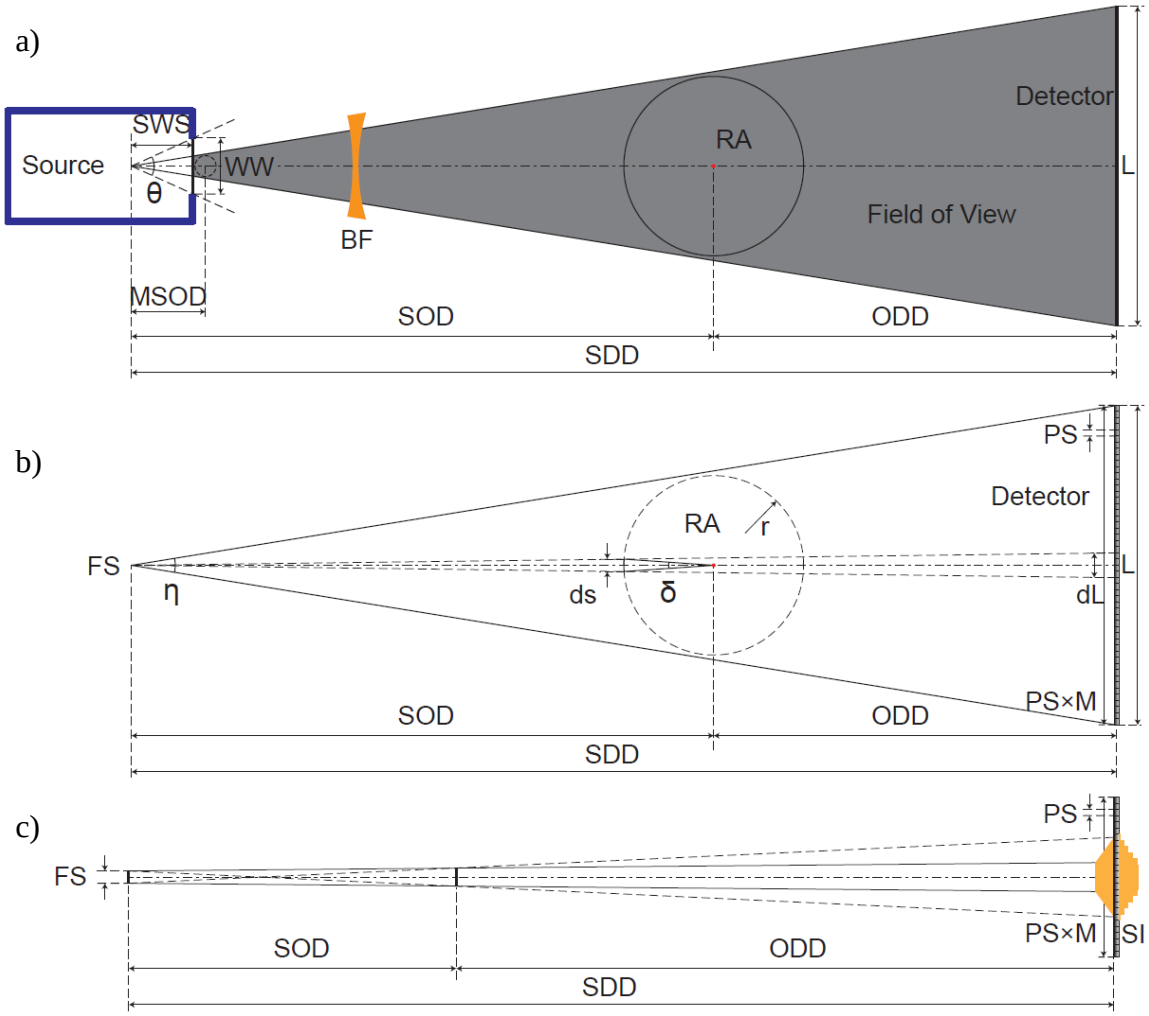

Figure 2.4 Geometrical schematic of an X-ray CT system. SWS = Source to window spacing, WW = Window width, BF = Bowtie filter, RA = Rotary axis, θ = Beam angle, MSOD = Minimum source to object distance, SOD = Source to object distance, ODD = Object to detector distance, SDD = Source to detector distance, FS = Focal spot size, SI = Signal intensity. a) General geometrical layout of a cone-beam CT, b) Rotation precision and its influence on image resolution, and c) the blurring effect and geometrical resolution analysis.

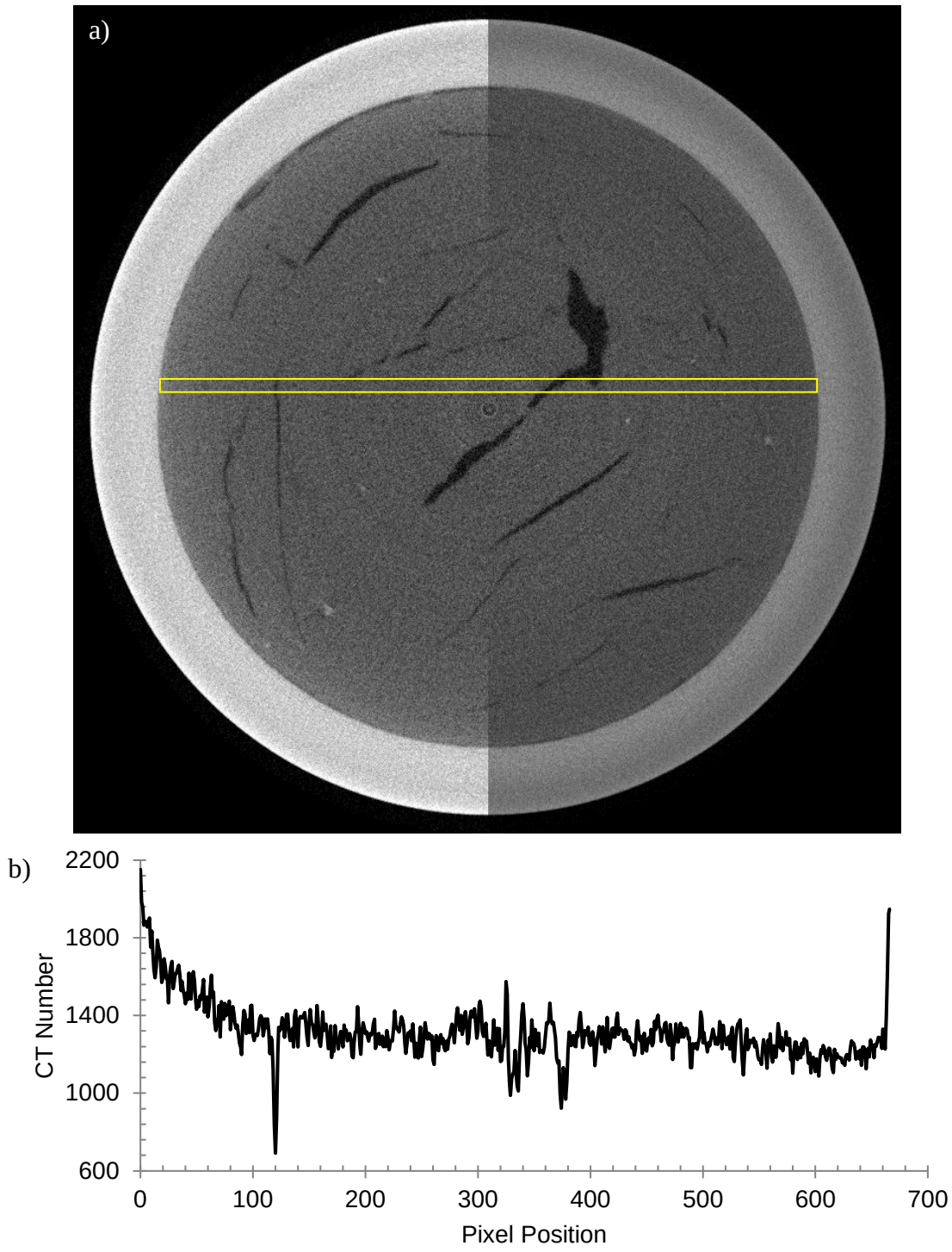

Figure 2.5 Gas driven fractures in a dry diatom specimen hosted in an aluminum chamber. a) Reconstructed images with beam hardening (left half) and after correction (right half), and b) the CT number along the long axis of the yellow rectangle in a).

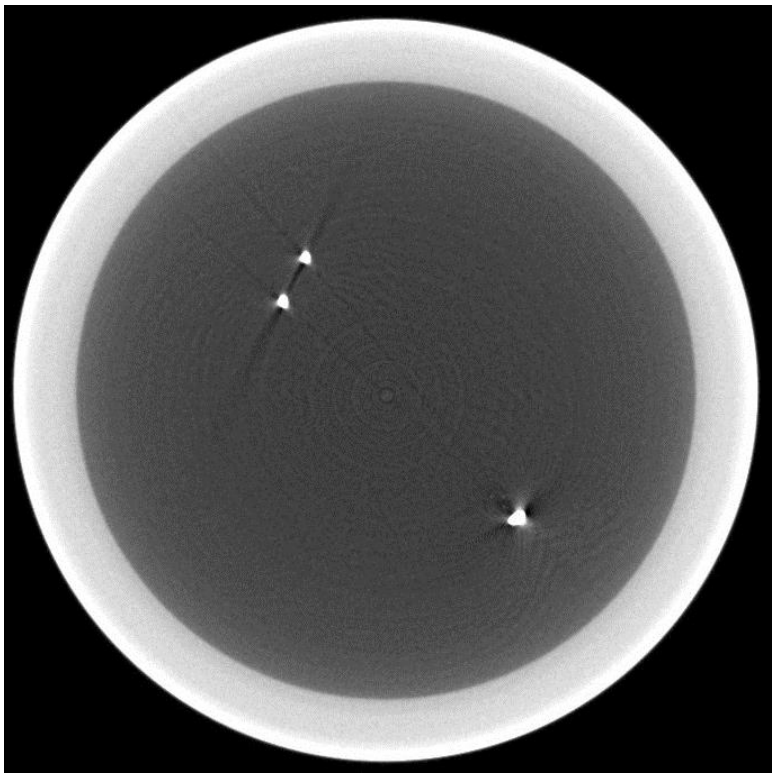

Figure 2.6 Ring artifact caused by imperfect detector calibration and metal stike artifact induced by two pairs of thermocouple in a bentonite specimen housed in an aluminum chamber.

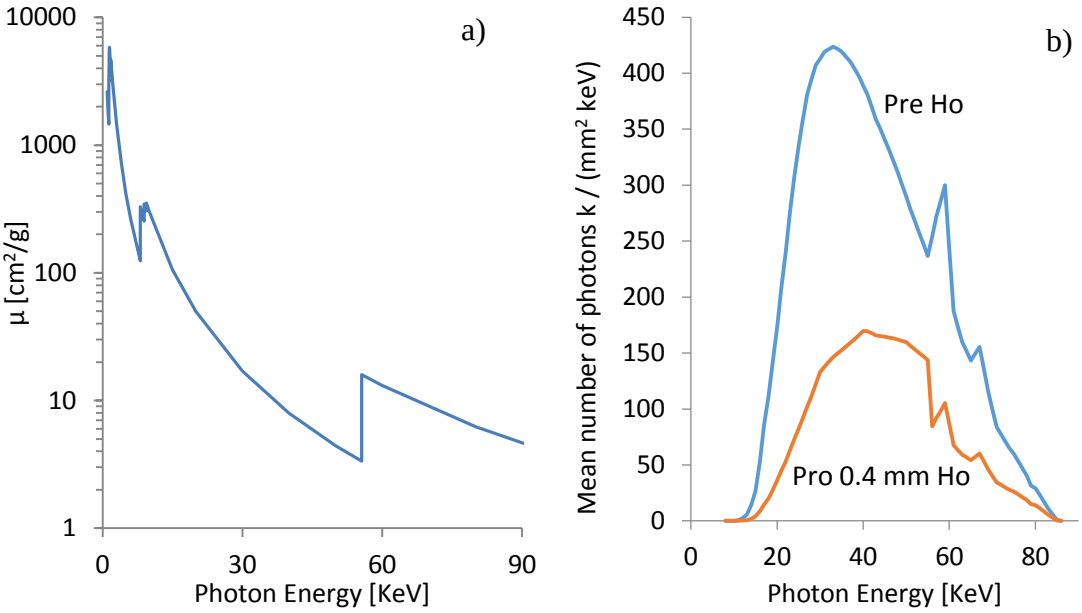

Figure 2.7 Filter technique used in X-ray spectra design. a) Attenuation coefficient of Holmium as a function of photon energy, and b) the comparison between the pre-filtered X-ray spectrum and the pro-filtered X-ray spectrum with a 0.4mm thick Holmium filter. (Data from Berger et al., 2010. NIST XCOM database)

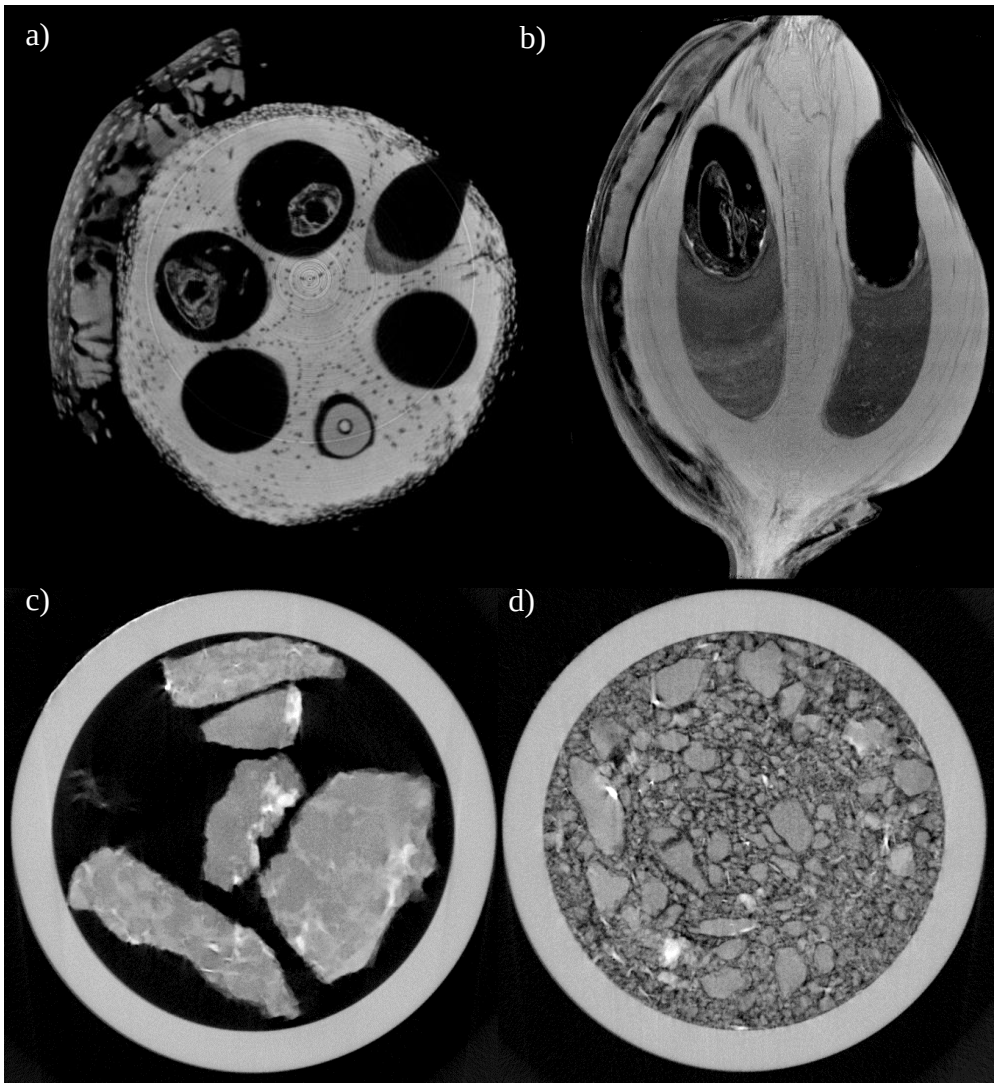

Figure 2.8 Slices of 3-D reconstructed images obtained with the micro-CT at PMRL. a) and b) Horizontal and vertical slices of the same nut, c) horizontal slice of gravels in an aluminum chamber and d) horizontal slices of well-graded sand in an aluminum chamber.

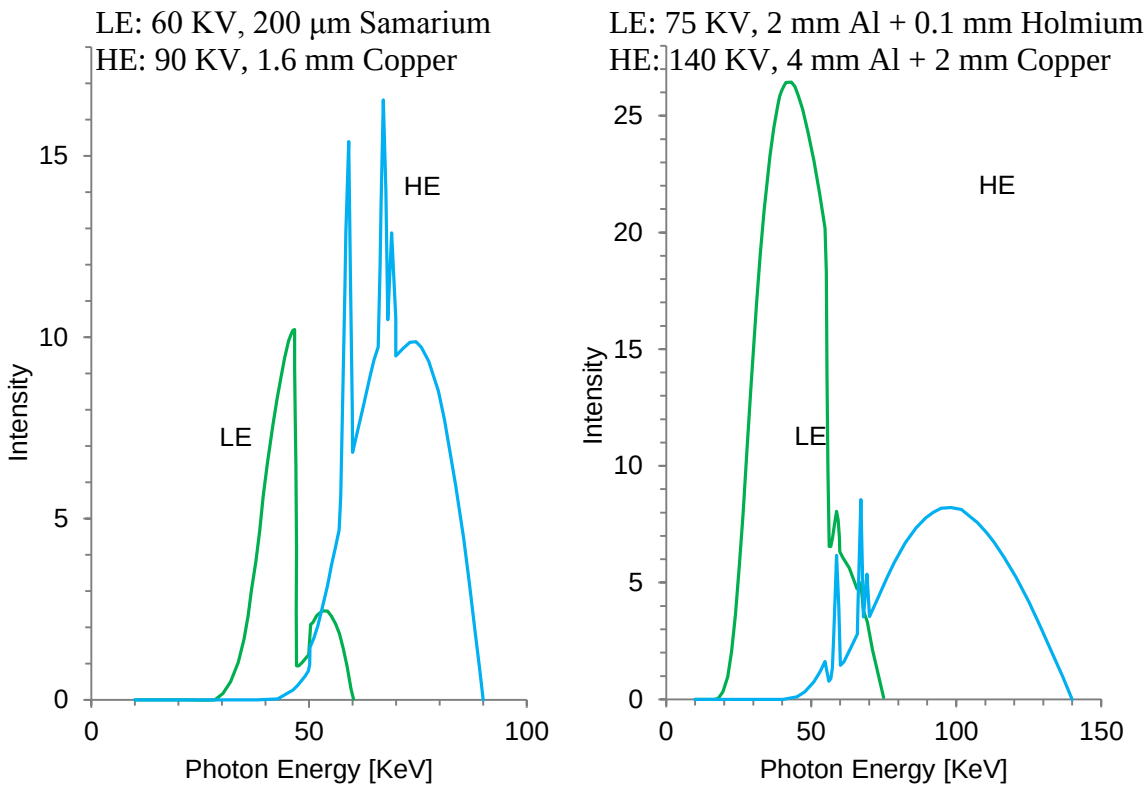

Figure 2.9 Dual energy techniques X-ray spectra design (Rebuffel and Dinten 2007).

CHAPTER 3

GAS HYDRATE FORMATION IN FINE-GRAINED SEDIMENTS

3.1 Introduction

Fine-grained sediments host over 90% percent of the global gas hydrate accumulations (Boswell and Collett 2006). Methane solubility in water is 0.102mol/kg (5MPa, 273.15K), the equivalent to one methane molecule in 550 water molecules. By contrast, there is one methane molecule per 6 to 7.4 water molecules present in the methane hydrate structure (Sloan and Koh 2007). Therefore, methane hydrate formation from dissolved gas is inherently gas limited.

Dissolved methane transport involves diffusive and advective contributions. The contribution of advective transport decreases in sediments with a high specific surface and low hydraulic conductivity, and hydrate tends to accumulate in coarse clean sands. Furthermore, small pores affect the phase boundary of gas hydrate (Handa and Stupin 1992; Seshadri et al. 2001; Uchida et al. 2001), and a segregated rather than a pore-filling hydrate morphology develops in fine-grained sediments (Dai et al. 2012).

This chapter focuses on the fundamental understanding of gas hydrate nucleation and growth in fine-grained sediments. The analyses address: the phase boundary shift, segregated hydrate morphology, alternative gas supply methods, hydrate topology and emerging crystal growth patterns.

3.2 Gas Hydrate Nucleation

State of knowledge. Water and gas molecules continuously vibrate and form small ordered clusters prior to hydrate nucleation. These clusters are not stable until they exceed the critical nucleation size. The induction time reflects the inherent stochastic nature of the process. Average induction times decrease with the increase of supersaturation and temperature depression in hydrate formation experiments (You et al. 2015).

The critical nucleation size differs in homogeneous and heterogeneous nucleation. In particular, a complete nuclei-wetting flat surface decreases a nucleus Gibbs free energy by half and promotes the nucleation process (Fletcher 1958; Kashchiev and Firoozabadi 2002; Lee et al. 2007). The critical nucleous size decreases with the increase in the degree of super-saturation, over-pressure and temperature depression. Estimations of critical nucleation size for methane hydrate range from 14.5 Å to 170 Å (Baez and Clancy 1994; Radhakrishnan and Trout 2002; Westacott and Rodger 1998).

Renewed Analysis. Hydrate nucleation in porous media experiences additional constraints. Consider an isolated pore diameter d_p and a critical nuclei size diameter d_c (Figure 3.1). The solute concentration before nucleation is c_s, and the solute concentration after nucleation c_{p0} is in equilibrium with the formed crystal. Under these conditions, the minimum pore size for nucleation within a "closed" pore without solute exchange with adjacent pores is computed from mass conservation of the solute:

$$c_s \frac{3\pi}{32}\left(d_p\right)^3 = \frac{3\pi}{32}\left(d_c\right)^3 + c_{p0}\frac{3\pi}{32}\left(\left(d_p\right)^3 - \left(d_c\right)^3\right) \tag{3.1}$$

$$d_p = d_c\left(\frac{1-c_{p0}}{c_s - c_{p0}}\right)^{1/3} \tag{3.2}$$

where the concentrations are specified in terms of the volume of solute/volume of solution. Note that in the case of the methane hydrate, the solute is $CH_4 \cdot nH_2O$ rather than CH_4, assume $c_s \approx 1.2 c_{p0}$ and n=6, $c_{p0} \approx 1.34\%$ (equivalent to 0.102 mol/kg). Therefore, $d_p/d_c \approx 7.2$. That is, for a critical nuclei size d_c= 40 Å, the pore size should be d_p= 288 Å. Therefore, this analysis highlights the low probability of stable hydrate nucleation in small pores and preferential nucleation in large pores as the diffusive transport between the pores may not be fast enough to sustain an incipient nucleation growth.

3.3 Gas Hydrate Phase Boundary in Fine-grained Sediments

The hydrate phase boundary is different in fine-grained sediments to that of bulk hydrate. The following discussion reframes previous analyses under the unifying concept of curvature rather than pore size.

3.3.1 The unification of the Kelvin and Gibbs-Thomson equations

The Kelvin and Gibbs-Thomson equations are equivalent to each other under ideal conditions in single substance condensation processes. The integrated form of the Clapeyron equation is the connection between these two equations (McDonald 1953). This section explores new analyses in the context of hydrate formation.

Kelvin's equation. The interface between water and vapor at a particular capillary rise is in equilibrium with the vapor pressure at the height of the capillary rise, which is different to the vapor pressure at the flat water-air interface (Thomson 1872). (von Helmholtz 1886) derived the modern form of the equation,

$$\ln \frac{P_g}{P_{g0}} = \kappa_{wg} \Gamma_{wg} \frac{V_m}{R_g T} \tag{3.3}$$

where P_g is the actual vapor pressure, P_{g0} is the saturated vapor pressure, $\kappa_{wg}=1/r_1+1/r_2$ is the curvature of the interface (r1 and r2 are the principle radii of curvature), Γ_{wg} is the surface tension between the liquid/crystal and its vapor, V_m is the molar volume of the liquid/crystal, R_g=8.314 J/(mol·K) is the gas constant, and T is the temperature. The curvature of the interface $\kappa_{wg}=2\cos(\theta)/r_t$ when in a cylindrical tube, where θ is the contact angle and r_t is the radius of the capillary tube.

At the molecular scale, the number of bonds connected to a water molecule on a concave interface is greater than for a water molecule on a flat interface. Therefore, a water molecule on a concave interface has lower activity and a lower tendency to jump into the vapor phase (Figure 3.2). The trend reverses on a convex interface: the vapor pressure against a convex water-vapor interface is higher than against a concave interface. Therefore, water vapor will migrate from convex to concave interfaces. Similar processes take place at the hydrate-water interface, including mass transfer.

The Clapeyron equation. This equation captures the pressure-temperature interdependency in the phase transformation process. The slope of the phase boundary on a pressure-temperature diagram is,

$$\frac{dP}{dT} = \frac{L}{T\Delta V} \tag{3.4}$$

where P is the external pressure of the overall system, L is the molar latent heat of the phase transition, and ΔV is the volume change of the overall system. Equation 3.4 could be rewritten as:

$$\frac{dT}{T} = \frac{dP}{L}\Delta V = \frac{dP}{P}\frac{P\Delta V}{L} = d\ln(P)\frac{P\Delta V}{L} \tag{3.5}$$

where $P\Delta V = ZR_gT$, and Z is the gas compressibility. The integrated form of the Clapeyron equation is,

$$\ln\left(\frac{P_g}{P_{g0}}\right) = \frac{L}{ZR_g}\left(\frac{1}{T_1} - \frac{1}{T_2}\right) \tag{3.6}$$

The Gibbs-Thomson equation. Kelvin's Equation 3.3 and Clapeyron Equation 3.6 combines into the equation in an ideal gas case (Z=1),

$$\frac{\Delta T}{T_B} = \kappa_{wg}\Gamma_{wg}\frac{1}{H_f\rho_h} \tag{3.7}$$

where ΔT is the temperature depression from the bulk phase boundary; T_B is the temperature at the bulk phase boundary; H_f is the bulk enthalpy of fusion; ρ_h is the hydrate density. Note $L=H_fV_m\rho_h$. The latent heat for the hydrate-water equilibrium L_{hw} combines the latent heat from the hydrate-water-gas equilibrium L_{hwg} and the heat of solution L_s, that is $L_{hw}=L_{hwg}+L_s$ (Anderson 2004). A common assumption for the contact angle for the hydrate-water interface and hydrate-gas interface is 180° (Anderson et al. 2009; Kwon et al. 2008; Sun and Duan 2007).

3.3.2 Curvature effect on hydrate phase boundary

The phase boundary of methane hydrate involves more than two phases. However, the Clapeyron's equation still applies to the whole system. The volume of gas locked in hydrate dominates the volume change in the hydrate-water-gas system (the volume difference between hydrate and water is relatively negligible especially when the

pressure is not very high (Sloan and Koh 2007). Therefore, the volume change approximates the gas volume $\Delta V \approx V_g$, then $P\Delta V \approx PV_g = ZR_gT$. Then we derive the modified Kelvin equation for hydrate by the substitution of Equation 3.7 to 3.6,

$$\ln \frac{P_g}{P_{g0}} = \frac{2\Gamma_{wg}}{r} \frac{V_m}{ZR_gT} \tag{3.8}$$

Figure 3.3 illustrates the comparison between the estimations of the Gibbs-Thomson and modified Kelvin equations. The two match well under low-pressure conditions, but deviate at high-pressures. This is primarily due to the increase in the volume difference between the hydrate and water as the gas density increases. Note the compressibility Z in Equation 3.8 used here corresponds to the gas pressure on the shifted phase boundary, and calculations require an iterative solution.

3.3.3 Solubility as another dimension in hydrate phase diagram

Methane solubility in water varies with pressure and temperature and is different whether hydrate is present or not (Konrad and Lankau 2005; Lu et al. 2008). Hydrate is in equilibrium with the methane saturated water in a two-component system. Therefore, the hydrate phase P-T boundary in the 2D pressure-temperature space is the projection of a 3-D boundary in the pressure-temperature-concentration space (Figure 3.4). Clearly, a certain pressure-temperature condition could be either inside or outside the stability field.

Figure 3.5 summarizes published experimental results and theoretical predictions for methane solubility in a hydrate-water equilibrium system. A common assumption is that the solubility of methane in water decreases to form more hydrate as the pressure increases (Lu et al. 2008). Experimental results that utilize the Raman spectroscopy (Lu et al. 2008) support this trend and infer that hydrate could be in equilibrium with a lower concentration solution with an increase in pressure. However, other experiments fail to demonstrate a clear correlation between the methane concentration and pressure (Servio and Englezos 2002) (Kim et al. 2003; Seo et al. 2002). (Hashemi et al. 2012) developed a thermodynamic model that captures the trend observed in Sevio and Englezos (2002).

Super-saturation and crystal curvature. The partial vapor pressure of a certain condensed matter is actually the concentration of the vapor phase. Hence, the Kelvin equation applies to the equilibrium between the hydrate interface with curvature and concentration of the water-methane solution (Adamson and Gast 1997; Correns and Steinborn 1939; Scherer 1999; Steiger 2005). This analysis assumes that the activity coefficient of methane dissolved in water is a constant number under conditions of low methane solubility. Then the methane concentration could represent the activity. Therefore,

$$\ln\frac{c}{c_0}+n\ln a_w=\frac{2\Gamma_{hw}}{r}\frac{V_m}{R_gT} \tag{3.9}$$

where c is the concentration of methane in the super-saturated solution, c_0 is the methane solubility in equilibrium with the bulk hydrate, and a_w is the water activity.

Mineral surfaces suppress the water activity due to water attraction to hydrophilic walls. The growth of hydrate in small pores should also consider the water activity change. Water activity in capillary tubes is,

$$\ln a_w=\frac{2\Gamma_{wg}\cos(\theta)}{-r}\frac{V_{mw}}{R_gT} \tag{3.10}$$

Note that the water curvature uses a different sign to the hydrate curvature. Finally, Equation 3.9 becomes,

$$\ln\frac{c}{c_0}=\frac{2\Gamma_{hw}V_{mh}+2n\Gamma_{wg}\cos(\theta)V_{mw}}{rR_gT} \tag{3.11}$$

Equation 3.11 implies that both the increase in the hydrate potential and the subsequent decrease in the water activity levels contribute to the super-saturation of methane. The super-saturation in this scenario is in equilibrium with the curved-surface shaped hydrate. This compares to the methane concentration which is in equilibrium with the bulk hydrate. Homogeneous nucleation in bulk water does not involve a change in water activity and Equation 3.9 simplifies into,

$$\ln\frac{c}{c_0}=\frac{2\Gamma_{hw}}{r}\frac{V_m}{R_gT} \tag{3.12}$$

A concentration gradient arises between small and large nuclei and large crystals grow at the expense of small crystals (Ostwald Ripening). This process involves the diffusion of solvents from the small to large nuclei, driven by the concentration gradient.

Any point within the 3D phase stability field in the pressure, temperature and methane-concentration space corresponds to either temperature depression, methane super-saturation or over-pressure. The three are equivalent to each other in terms of the chemical potential. The chemical potential difference from the bulk phase enables the solution to equilibrate with a curved hydrate-water interface. Consequently, the solubility of methane must be included besides pressure and temperature to characterize the curvature effect.

3.4 Gas Hydrate Morphology and Mechanical Equilibrium with Sediment

Gas hydrate morphology in fine-grained sediments depends not only on the behavior of the crystal but also on the interaction between the crystal and the sediments.

3.4.1 Interfacial properties

Hydrate-water Interface and Pre-melting. The concept of a pre-melting ice surface has been present for over half a century (Bowden and Hughes 1939; Dash et al. 1995). Pre-melting of the ice surface commences at -33°C, and furthermore, the structure does not totally solidify until 0K (Li and Somorjai 2007). The thickness of the pre-melting layer rapidly increases as the overall temperature approaches the bulk melting temperature. The contact between the ice and other solid surfaces is the interaction of the two solid surfaces via a liquid-like layer (Rempel 2007), as opposed to the direct contact between two solid surfaces. Currently, no direct measurement of the hydrate-water interfacial tension exists (Sun and Duan 2007). Researchers generally assume that the value is the same as the ice-water interfacial tension (Clennell et al. 1999; Henry et al. 1999). Reported ice-water interfacial tension varies from 25 to 33mJ/m^2 (Anderson 2003; Hillig 1998).

Water-gas Interface and Pressure. The interfacial tension between water and gas decreases with the increase in pressure. This value approaches the asymptote, which is the value between the water and liquid gas (Massoudi and King Jr 1974). The surface tension between the water and methane reduces by approximately 10%, with an increase in pressure from 0 to 7.5 MPa when the temperature is at 25°C. However, the interfacial tension between water and liquid CO_2 is not sensitive to pressure increases (Espinoza and Santamarina 2010).

Hydrate-gas Interface. Here we assume that the hydrate-gas interfacial tension equals the ice-gas interfacial tension of 109mJ/m^2 (Mason 1971).

3.4.2 Equilibrium in capillary tubes

Section 3.3 discusses the thermodynamic effect of an interfacial curvature on hydrate stability. This section details the consequent mechanical equilibrium. The Laplace equation characterizes capillary pressure between the two phases separated by the interface as,

$$P_{capillary} = \frac{2\Gamma \cos\theta}{r} \tag{3.13}$$

Figure 3.6 illustrates several cases of hydrate formation. The contact angle is assumed to be 180°. Hydrate initially forms in the large pores as the required temperature depression here is less than in the small pores. The increase in the temperature depression promotes the hydrate crystal growth through the pore throats and the consequent invasion into the adjacent pores. The pressures relationship is: $P_h = u_w + P_{capillary}$, where P_h is the hydrate pressure, and u_w is the water pressure. The hydrate internal pressure increases with the decrease in the interfacial curvature.

In a three-component system where hydrate, water and gas coexist (Figure 3.6c), water is subjected to the suction from both the gas and hydrate fronts.

$$P_g - P_{capillary,wg} = u_w = P_h - P_{capillary,hw} \tag{3.14}$$

Calculations assume the same pressures for the gas and hydrate. Then the capillary pressure between the gas and water should equilibrate to that between the hydrate and water,

$$\frac{4\Gamma_{gw}\cos\theta}{d_1} = \frac{4\Gamma_{hw}}{d_1} \tag{3.15}$$

The contact angle that satisfies this relation (θ^*) is 65° when the interfacial tension between the hydrate and water Γ_{hw} is 32 mJ/m^2 and between the water and gas Γ_{wg} is 76 mJ/m^2. When the contact angle is less than θ^*, the suction from the gas front exceeds the suction from the hydrate front. The hydrate then invades into the pore. By contrast, when the contact angle is larger than θ^*, the suction from the hydrate front surpasses that from the gas front. The hydrate then grows with the water extracted from the pores. Consequently, the hydrate growth occurs outside the pores.

3.4.3 Equilibrium between hydrate crystal and the sediment

Studies of the pore size effect frequently assume that the pore shape does not change during the crystal formation and dissociation processes. However, pores cannot exist without a container, which creates the separated pore space. A small crystal is in a state of self-reacted equilibrium in bulk water. The pore wall, which is the container in porous media, holds the pressure difference between the crystal and the fluid.

The crystal growth in the pores could damage and degrade the porous media when the crystal pressure exceeds the strength of the porous media (Valenza and Scherer 2006). The strength of the pore wall depends on the tensile strength of the material such as rock and concrete. However, particulate materials such as non-cemented sediments have no tensile strength. The effective stress then characterizes this pore wall strength. The stress generated by the hydrate crystal growth balances the effective stress in fine-grained marine sediments. Effective stress in the sediments could be much less than the capillary pressure between the crystal and fluid, particularly in shallow marine sediments. Alternatively, the sediments skeleton is not strong enough to constrain the stress induced

by the crystal growth. Consequently, crystal growth enlarges the pores. This enlargement process is the mechanism involved in the particle-displacive formation (Figure 3.6d).

We define the characteristic pore throat size in a particular sediment as d^*. This pore size corresponds to a characteristic capillary pressure $P_{capillary}^*$ (Laplace equation) and a characteristic temperature depression ΔT^* (Gibbs-Thomson equation). Note that the temperature depression is equivalent to the over-pressure and super-saturation in terms of the chemical potential. We use temperature depression here for convenience and assume an unlimited methane supply for this analysis.

Table 3.1 summarizes hydrate sediments locations, effective stress, pore pressure, temperature and sediment particle sizes. Figure 3.7 plots the effective stress σ' normalized by the characteristic capillary pressure $P_{capillary}^*$ versus the temperature depression ΔT and normalized by the characteristic temperature depression ΔT^*.

The hydrate crystal pressure is in equilibrium with the summation of effective stress and fluid pressure, $P_h=u_w+\sigma'$,

$$\sigma' = P_{capillary} = \frac{2T_{hw}}{r} \Rightarrow r = \frac{2T_{hw}}{\sigma'} \tag{3.16}$$

Substitute Equation 3.16 to the Gibbs-Thomson equation (Equation 3.7),

$$\Delta T' = \frac{\sigma'}{H_f \rho_h} T_B \tag{3.17}$$

where $\Delta T'$ represents the temperature depression that a given effective stress can hold on the crystal. The diagonal line in Figure 3.7 represents Equation 3.17. Six zones then emerge due to the separation of this space.

<u>*Zone N1.*</u> $\Delta T<\Delta T'$ & $\sigma'<P_{capillary}^*$. The effective stress limits crystal formation. The temperature depression in this region is insufficient to enable the crystal to push particles away. The condition typically occurs in deep marine fine-grained sediments in areas where the temperature depression is low due to the geothermal gradient, and the effective stress is relatively high.

<u>*Zone N2.*</u> $\Delta T<\Delta T^*$ & $P_{capillary}^*<\sigma'$. This is the true pore size effect dominated zone. The characteristic capillary pressure limits crystal growth. When $P_{capillary}^*<\sigma'$, the hydrate

crystal growth cannot displace the particles. Therefore, the crystal growth does not alter the pore geometry. The temperature depression in this zone does not permit the crystal to invade into adjacent pores.

Zone Y1. $\Delta T \geq \Delta T'$ & $\Delta T < \Delta T^*$. Hydrate does not have the capability to invade into the sediment pores due to the capillary pressure. However, hydrate crystals can grow by the displacement of the sediment particles (Figure 3.8a). The condition typically occurs in shallow fine-grained sediments. An analysis by pore size effect negates the possibility of hydrate formation in this zone. However, field explorations frequently observe extensive segregated hydrate formations.

Zone Y2. $\Delta T \leq \Delta T'$ & $\Delta T \geq \Delta T^*$. Hydrate formation in this zone is pore-filling. The soil fabric does not change due to the hydrate formation (Figure 3.8b).

Zone Y3. $\sigma' < P_{capillary}^*$ & $\Delta T \geq \Delta T^*$. The hydrate formation in this zone is primarily particle-displacive. The temperature depression is sufficient to enable hydrate formation in small pores. However, even in the presence of pore-filling crystals, these crystals display a larger curvature than the particle displacive crystals. Consequently, the large displacive crystals with less pronounced curvature grow at the expense of the small pore-filling crystals due to the Ostwald ripening, illustrated in Figure 3.8c.

Zone Y4. $P_{capillary}^* < \sigma'$ & $\Delta T \geq \Delta T'$. Hydrate crystals are primarily pore-filling although the temperature depression enables the crystal to balance the effective stress. Theoretically, hydrates can invade into the pores by process of creep when in the presence of segregated hydrate crystals. Pore-filling hydrate may be present in the fine-grained sediments in this zone. However, the crystal size should be in the same order as the pore size, which is usually invisible without magnification. When the pore size is significantly larger than the hydrate crystal curvatures, contact-cementing, grain-coating and pore-filling morphology can exist (Figure 3.8d).

When the hydrate formation behavior is particle-displacive, the so-called pore size effect on the hydrate phase boundary is actually a function of the effective stress. The effective stress in this scenario is not the vertical stress, but rather it is perpendicular to the crystal surface. Note that the definition of temperature depression subjects to a particular methane concentration and pressure.

We define the temperature depression in the sediments as:

$$\Delta T = \begin{cases} \dfrac{\sigma'}{H_f \rho_h} T_B & if \quad \sigma' < P^*_{capillayr} \\ \Delta T^* & if \quad \sigma' \geq P^*_{capillayr} \end{cases} \tag{3.18}$$

Therefore, the revision of the bottom simulator reflector (BSR) depth calculation should include not only the pore size but also the effective stress.

3.4.4 Crystal Morphology

Crystal Morphology without Boundaries. Due to the molecular structure, the crystal lattice subject to certain temperature and pressure conditions favors particular structures that minimize the energy of the system. The energy required to create a surface depends on the surface orientation. The distance of any stable crystal surface from the center of the crystal is proportional to its surface tension (Adamson and Gast 1967). For a polyhedron crystal, the equilibrium shape usually coincides with the lattice structure of the crystal.

However, natural crystals larger than a particular size do not usually display the most stable shapes, dependent on the formation conditions. In addition, crystal defects such as dislocations and imperfections introduced during the dynamic formation process could alter the morphology. Consequently, crystals do not share identical morphologies due to the variations in formation conditions.

Particle-displacive Crystal Morphology with Boundaries. The sediments contain interconnected water that surrounds the hydrate crystals. Therefore, we assume that the salinity, methane concentrations and other solvents that could alter the phase equilibrium are in the same state in the environment around the hydrate crystal. The assumption only applies when the system is in a state of equilibrium. Consequently, the crystal surface has the same curvature wherever it contacts the water, and there is no deviatoric stress in the crystal. Note that the above assumption does not apply in a dynamic system as the required time scale to diffuse the excluded ion or methane could be longer than the time scale of the dynamic formation and dissociation processes.

A hydrate crystal in the sediment is a balloon-like structure that bears the same effective stress and the fluid pressure from all directions. The morphology of the crystal, in this case reflects the adjacent effective stress distribution in the sediments.

3.4.5 Sediment consolidation induced by hydrate growth

Sediments inhibit the formation of hydrate by pore size limitation and effective stress, and the growth of hydrate crystals displaces the particle and consolidates the sediment. The consolidation effect in this discussion only applies to the particle-displacive hydrate morphology.

The degree of sediment consolidation. The capillary pressure between the hydrate and pore fluid applies additional pressure to the soil skeleton. Therefore, the effective stress on the soil skeleton is larger with the presence of hydrate than without. The effective stress in the sediment that surrounds the hydrate corresponds to the curvature of the hydrate crystal surface. This curvature corresponds to the chemical potential of the hydrate crystal. The chemical potential in the sediments could be in the form of a temperature depression, or an over-pressure or a super-saturation. Therefore, the effective stress after hydrate formation is,

$$\sigma' = \frac{\Delta T}{T_B} H_f \rho_h = \ln \frac{c}{c_0} \frac{R_g T}{V_m} = \ln \frac{P_g}{P_{g0}} \frac{Z R_g T}{V_m} \tag{3.19}$$

Calculation of the effective stress in geological sites depends on the degree of super-saturation and the available pressure-temperature data. Alternatively, the effective stress in the sediments informs the degree of super-saturation. In-situ test data indicates an increase in the effective stress of 40-60 kPa in hydrate-bearing fine-grained sediments in comparison to normally consolidated sediments (Sultan et al. 2010).

3.5 Formation Mechanisms and Topology

3.5.1 Gas supply

Initial gas content and solubility. Methane solubility in water varies, dependent on the presence or absence of gas hydrate in the solution. This variation in solubility induces the formation of a 4mm thick hydrate lens within a 1m thick cubic solution (Jang and Santamarina 2016). The formation of this amount of hydrate develops with the methane dissolved in the solution and does not involve a long distance supply.

Subsequent gas supply. The Péclet number decreases with particle and pore size. Therefore, diffusion dominates the mass transfer in fine-grained sediments. The estimated time scale for diffusion-controlled gas hydrate to form a 200-m-thick methane hydrate zone can be up to tens to hundreds of millions of years (Xu and Ruppel 1999). For laboratory experimental purposes, gas diffuses through a 2-cm-thick specimen over the course of 7 days. The time required is proportional to the squared specimen thickness.

However, diffusion is not the only gas supply path into fine-grained sediments (Figure 3.10). Ocean explorations in a variety of sites report abundant pockmarks on the ocean floor. Pockmarks indicate an historical gas release from the bottom of the ocean (Paull et al. 1995). Furthermore, active gas plumes can coexist with gas hydrate-bearing sediments (Wood et al. 2002). The height of one plume reached 1400m in an extreme case (Gardner et al. 2009). These observations indicate the extensive and disruptive gas flow through the hydrate stability zone. Additionally, in-situ testing results demonstrate the presence of gas-filled cavities in shallow marine sediments (Sultan et al. 2014). Experimental results in Chapter 4 illustrate that gas driven fractures can remain open in consolidated fine-grained sediments when the gas flow ceases.

3.5.2 Diffusion dominated hydrate formation

Hydrate formation by diffusion is a diffusion-reaction process. Similar natural processes create Liesegang bands or rings (Figure 3.9). Methane diffusion through the sediments follows the methane concentration gradient. When the first band of hydrate forms, the ion exclusion increases its concentration near the hydrate formation front. The

capillary effect consolidates the nearby sediments and decreases the pore size. The combination of these two effects results in a suppression of hydrate nucleation in the near field. Meanwhile, the hydrate in this condition yields a high methane concentration due to salinity and curvature effects. Therefore, hydrate could independently nucleate and form away from the pre-formed hydrate in areas where the methane concentration is relatively lower. However, these areas contain larger pore sizes and lower ion concentrations. The process continues with successive bands of hydrate. Consequently, hydrate could form the Liesegang bands.

However, this is a time intensive process, and interruptions such as gas driven fractures could easily disturb the diffusion front and alter the hydrate topology.

3.5.3 Gas-driven fractures formation

The conditions for gas-driven (immiscible fluid) fractures to form in water-saturated sediments are (Figure 3.10):

$$u_w + k_0\sigma'_v \le P_{gas} \le u_w + \sigma'_v \tag{3.20}$$

$$P_{gas} - u_w \le P_{capillary,wg} \tag{3.21}$$

where u_w is the pore water pressure, k_0 is the horizontal stress coefficient, $\sigma'_v = (\gamma_m-\gamma_w)z$ is the vertical effective stress (γ_w and γ_m are the density of water and sediments, and z is the depth of the sediments on top of the gas phase), P_{gas} is the gas pressure and $P_{capillary,wg}= \kappa_{wg}\Gamma_{wg}$. Equation 3.20 provides the relationship between gas pressure and the overall pressure. If the pore throats in the sediments are sufficiently small, gas will not invade into the sediment pores but will create fractures (Equation 3.21).

Equation 3.20 and 3.21 yields:

$$k_0\sigma'_v \le P_{gas} - u \le P_{capillary,wg} \tag{3.22}$$

Gas pressure originates from the buoyancy force at the bottom of the gas zone. Free gas accumulates beneath the hydrate stability zone and eventually reaches a critical

thickness that propagates gas fractures. Assume the thickness of the gas zone is h, and then the gas pressure of the top gas zone satisfies (Figure 3.10):

$$P_{gas} - u = h(\gamma_w - \gamma_g) \tag{3.23}$$

Equations 3.20 and 3.23 inform:

$$k_0 \frac{(\gamma_m - \gamma_w)}{(\gamma_w - \gamma_g)} \leq \frac{h}{z} \leq \frac{(\gamma_m - \gamma_w)}{(\gamma_w - \gamma_g)} \tag{3.24}$$

Equation 3.24 provides a range of gas zone thickness that could trigger gas driven fractures with a known thickness of the hydrate stability zone. Note that the density of the methane under high pressure is much higher than the methane density when subjected to the atmospheric pressure despite the same temperature (15MPa, 10°C, 128 kg/m^3).

3.5.4 Gas driven fracture accelerated hydrate formation

Hydrate forms on the interface between water and gas inside the fracture. The subsequent hydrate growth extracts water from the sediments, which shares the same mechanism as cryogenic suction. The two mechanisms of film and exo-pore patterns could both exist at this stage.

Film pattern formation. A thin porous hydrate film forms, thickens and solidifies on the hydrocarbon-water interface (Taylor et al. 2007; Uchida et al. 1999). The final long-term methane hydrate film thickness ranges from 20 to 100 μm, as the sub-cooling increases from 4 to 13.5°C (Taylor et al. 2007). Further hydrate growth relies on either gas diffusion through this film to the water-hydrate interface or water diffusion through the film to the hydrate-gas interface. The diffusion coefficient of tritium in natural ice at -10°C is approximately 2×10^{-11} cm^2/s (Ramseier 1967). This is 6 orders of magnitude slower than the H_2 diffusion coefficient in liquid water 4.5×10^{-5} cm^2/s (Cussler 2009), which is already significantly slow. CH_4 diffusion in solid is even slower than tritium due to its larger molecule size. In a worse scenario, if the water in the sediment is not initially saturated with gas, the methane dissolved in the water near the hydrate film diffuses into the far field. The hydrate film then dissolves into the water. This scenario can both occur

in laboratory and natural conditions. The negative feedback system dramatically limits the thickness of the hydrate formation. The hydrate growth starts at a high rate but significantly decreases when the solid film of hydrate forms and prevents the direct contact between the gas and water. We propose that the film pattern mechanism in hydrate formation could occur on the hydrocarbon-sediment interface in gas-filled openings (Figure 3.11).

Laboratory CO_2 hydrate formation experiments in fine-grained sediments demonstrate this film pattern when the film thickness exceeds the resolution of the micro-CT system (Chapter 4). Experimental results do not detect a film pattern hydrate growth thicker than 100 μm.

Exo-pore pattern formation. The curvature effect shifts the hydrate phase boundary to a lower temperature. Therefore, it is easier to form hydrate outside than within the pores due to the temperature depression. Crystal initially nucleates on the end of the pore, and the subsequent hydrate growth depends on the water supply from the sediment and the gas supply from the gas-filled openings (Figure 3.11). The hydrate formation front is on the interface between the hydrate and water. The capillary pressure between the hydrate and water drives the water supply from the sediment, termed cryogenic suction. Simultaneously, gas filled openings provide a direct gas supply to the hydrate formation front. The hydrate-phobic mineral surface tends to repel the hydrate. Consequently, the hydrate automatically rises from the root.

Figure 3.12 illustrates a number of natural examples that result from this pattern. We also observe this pattern in laboratory gas hydrate formation experiments, either on the surface of the fine-grained sediments or within the gas-filled openings (Chapter 4). This same mechanism produces up to 5 cm long crystals in 3 to 4 hours (Chapter 4,(Hofmann et al. 2015) .

The subsequent gas hydrate formation consumes the gas in the openings and decreases the gas pressure. This process eventually collapses the openings and consolidates the hydrate. Porous hydrates that do not fully solidify frequently exist in shallow marine fine-grained sediments (Sultan et al. 2014).

The horizontal stress near the hydrate crystal could be much higher than in the far field, as the cryogenic suction consolidates the sediments. Consequently, the hydrate formation densifies the adjacent sediment. The subsequent gas plume can occur in other sediment locations in areas of relatively lower strength. This trend continues until the whole field reaches a high hydrate saturation rate.

3.6 Conclusions

This chapter explored the fundamentals of hydrate formation in fine-grained sediments. The discussion details the molecular, particle and macro scale processes that are involved. The understanding of hydrate formation is critical to research on hydrate distribution (morphology and topology), to the anticipation of physical properties of hydrate-bearing sediments, and to the generation of potential gas production strategies. These analyses support the following conclusions:

- *Nucleation.* Hydrate nucleation requires a critical pore size that is significantly larger than the critical nucleation size. This critical pore size decreases with the increase in the degree of super-saturation.
- *Gas supply.* Methane supply to the hydrate formation front could take place through diffusion transport of dissolved methane gas, or through gas-driven fractures; the latter one is a much more efficient transport process.
- *Hydrate phase boundary.* The hydrate phase boundary in fine-grained sediments shifts accordingly to the curvature of the hydrate-water interface. The characterization of the hydrate phase boundary should consider the methane concentration as an additional critical factor in determining the chemical potential of curved-surface hydrate. The Gibbs-Thomson, modified Kelvin, and Kelvin-like super-saturation equations are equivalent to each other in the characterization of this curvature.
- *Morphology - Capillary pressure.* When the effective stress is larger than the characteristic capillary pressure, the hydrate formation is pore-filling. Hydrate tends to form particle-displacive morphology in other conditions.

- *Temperature depression.* The temperature depression that corresponds to the curvature of the hydrate-water interface is a function of the pore size when the effective stress is larger than the characteristic capillary pressure. By contrast, this temperature depression is a function of the effective stress when the characteristic capillary pressure is larger than the effective stress.
- *The equilibrium between hydrate and the sediments.* Sediments inhibit hydrate formation, because of either pore size limitations or effective stress. Conversely, the hydrate crystal repels the particle and consolidates the sediment.
- *Liesegang bands and hydrate topology.* Hydrate formation and growth by diffusion-controlled gas supply could develop Liesegang bands.
- *Film and exo-pore patterns.* Hydrate formation in gas-filled openings exhibits two patterns: hydrate films can form along the gas/sediment interface and exo-pore patterns that enable water suction from the sediment and forms a porous structure that guarantees the continuous gas and water supply to the formation front.

Table 3.1 Geological conditions present in natural hydrate-bearing sediments [a]

Location	σ' (MPa)	P_0 [b] (m)	D_{10} (μm) Mean	D_{10} (μm) s.dev.	T [c] (°C)	P_{pb} [d] (MPa)	T_{pb} [e] (MPa)	C^*_{gw} (MPa)	References [f]
Mallik	9.137	9.137	285	8.5	7.5	5.79	13.8	0.004	a,b,c
	9.03	9.03	108.4	76.02	7.2	5.60	13.7	0.010	a,b,c
	8.93-10.88	9.9	150	50	8.5	6.48	14.5	0.008	a,b,c
Blake Ridge	2.59	30.58	0.16	0.11	12.9	10.51	25.4	7.057	d,e,f
	3.30	31	0.001	0.0007	15.9	14.50	25.6	1129	d,e,f
	0.03	27.82	0.2	0.14	4.2	3.98	24.5	5.645	g,h,f
Nankai Trough	2.08-2.6	11.79	100	70.13	13.0	10.63	16.2	0.011	i,j
	0.9-1.4	47.99	10	7.01	8.5	6.48	30.1	0.113	k,j
NGHP	0.6	13	0.2	0.14	6.7	5.29	17.1	5.645	l,m,n,o
	0.58	11.07	1.6	1.12	6.7	5.29	15.6	0.706	p,n,o
Cascadia Margin	0.03	6.78	4	0.3	5.5	4.62	11.0	0.282	q,r
	0.13	6.87	2.5	0.2	6.3	5.06	11.1	0.452	q,r,s
Offshore Peru	1.41	39.61	0.01	0.01	8	6.13	28.1	113	t,u
	1.66	52.36	23	8	9.1	6.93	31.0	0.049	u,v
OKushiri Ridge	0.88-0.98	27.16	100	70.13	15.9	14.50	24.3	0.011	w
	0.88-0.91	27.16	0.01	0.01	15.3	13.60	24.3	113	w,x
	0.91	26.62	0.2	0.1	15.4	13.75	24.1	5.645	w
Ulleung Basin	1.36	21	1.5	1.05	7.3	5.66	21.7	0.753	y,z
	1.40	22.18	0.2	0.14	9.6	7.32	22.3	5.645	z,aa
Orca Basin, GOM	0.2-0.4	24.25	0.001	0.0007	4.4	4.07	23.1	1129	ab,ac,ad,ae
Alaminos Canyon, GOM	4	31.3	80	56.10	9.1	6.93	25.7	0.014	af,ae
Sea of Okhotsk	0.02-0.03	8.4	0.45	0.25	2.3	3.19	13.0	2.509	ag,ah
	0.02-0.03	6.7	0.4	0.2	2.3	3.19	10.9	2.823	ag,ah
Mt. Elbert	6.2	6.2	200	140.26	0	2.43	10.2	0.006	ai,aj,ak
	6.61	6.61	80	56.10	1	2.74	10.8	0.014	ai,aj,ak
	6.2	6.2	17	11.92	0	2.43	10.2	0.066	al
Atwater Valley, GOM	0-1.58	13.7	0.01	0.01	5.5	4.62	17.6	113	am,ae
Hydrate Ridge	0.05-1.06	9.46	0.2	0.14	11.2	8.74	14.1	5.645	an,ao,ap

[a]Effective stress, water pressure, and particle size are in agreement with Dai and Santamarina, 2012.
[b]Field water pressure calculations use water depth.
[c]Field site temperature calculations use sea floor temperatures and geothermal gradients if direct data is unavailable.
[d]Pressure calculations at the phase boundary use the bulk hydrate phase boundary and assume that the field temperatures do not change during gas production.
[e]Temperature calculations at the phase boundary use the bulk hydrate phase boundary and assume that the field pressure does not change during gas production.
[f]References are as follows: a, (Uchida et al. 2000); b, (Kulenkampff and Spangenberg 2005); c, (Bily and Dick 1974); d, (Matsumoto et al. 2000); e, (Collett and Wendlandt 2000); f, (Ruppel 1997); g, (Winters 2000); h, (Winters 1995); i, (Uchida et al. 2004); j, (Yamano et al. 1982); k, (Taira et al. 1991); l, (Yun et al. 2010); m, (Collett et al. 2008); n, (Mandal et al. 2014); o, (Kumar et al. 2014); p, (Winters et al. 2008); q, (Hovland et al. 1995); r, (Camerlenghi et al. 1995); s, (Westbrook et al. 1994); t, (von Huene et al. 1987); u, (Kvenvolden and Kastner 1990); v, (Hill and Marsters 1990); w, (Tamaki et al. 1990); x, (Holler 1992); y, (Lee et al. 2011); z, (Kim et al. 2011); aa, (Kwon et al. 2011); ab, (Pflaum et al. 1986); ac, (Thayer et al. 1986); ad, (Bryant et al. 1986); ae, (Milkov and Sassen 2001); af, (Boswell et al. 2009); ag, (Luan et al. 2008); ah, (Dang et al. 2010); ai, (Stern et al. 2011); aj, (Winters et al. 2011); ak, (Hunter et al. 2011); al, (Dai et al. 2011); am, (Yun et al. 2006); an, (Tan et al. 2006); ao, (Liu and Flemings 2006); ap, (Milkov 2004).

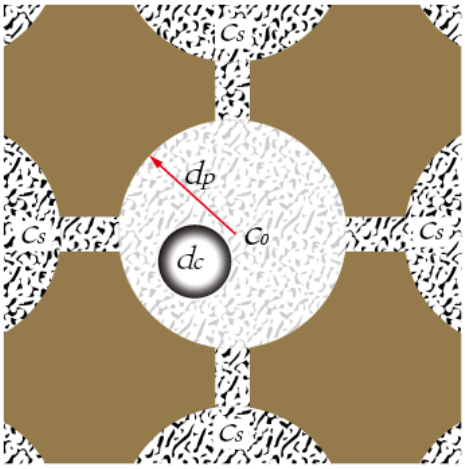

Figure 3.1 Mass conservation and crystal nucleation in pores.

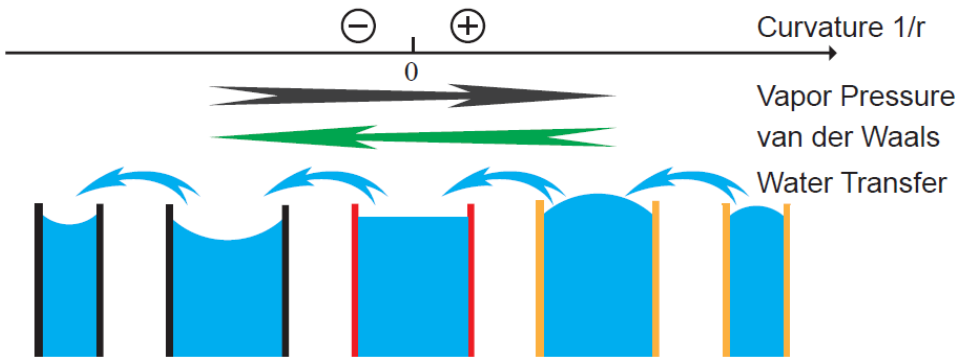

Figure 3.2 Kelvin equation implications.

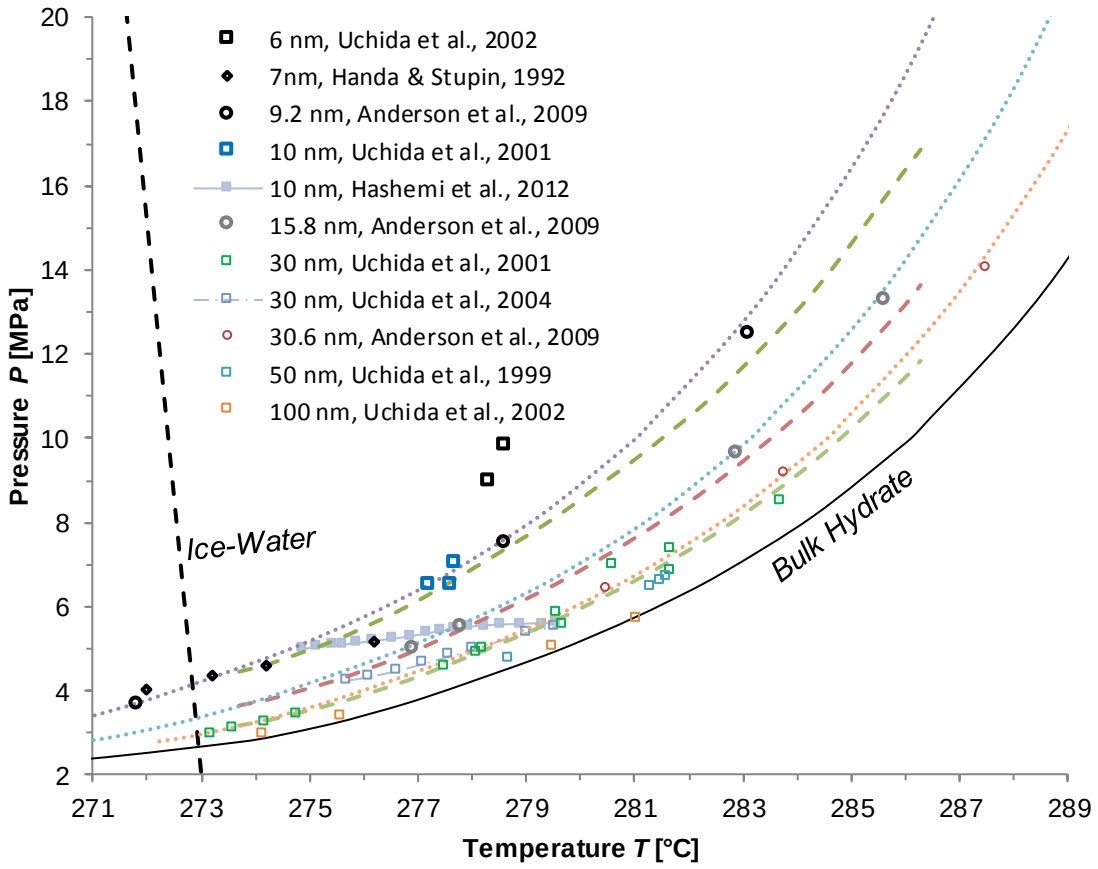

Figure 3.3 Temperature depression due to the curvature effect. Note the data from (Hashemi et al. 2012) and (Uchida et al. 2004) corresponds to continuous hydrate dissociation in porous media with pore size distribution. The dotted lines are the prediction from the Gibbs-Thomson equation, and the broken lines demostrate the estimation from the modified Kelvin equation. (Handa and Stupin 1992; Uchida et al. 2002) Anderson, 2009 #1886}(Uchida et al. 1999; Uchida et al. 2001; Uchida et al. 2002)

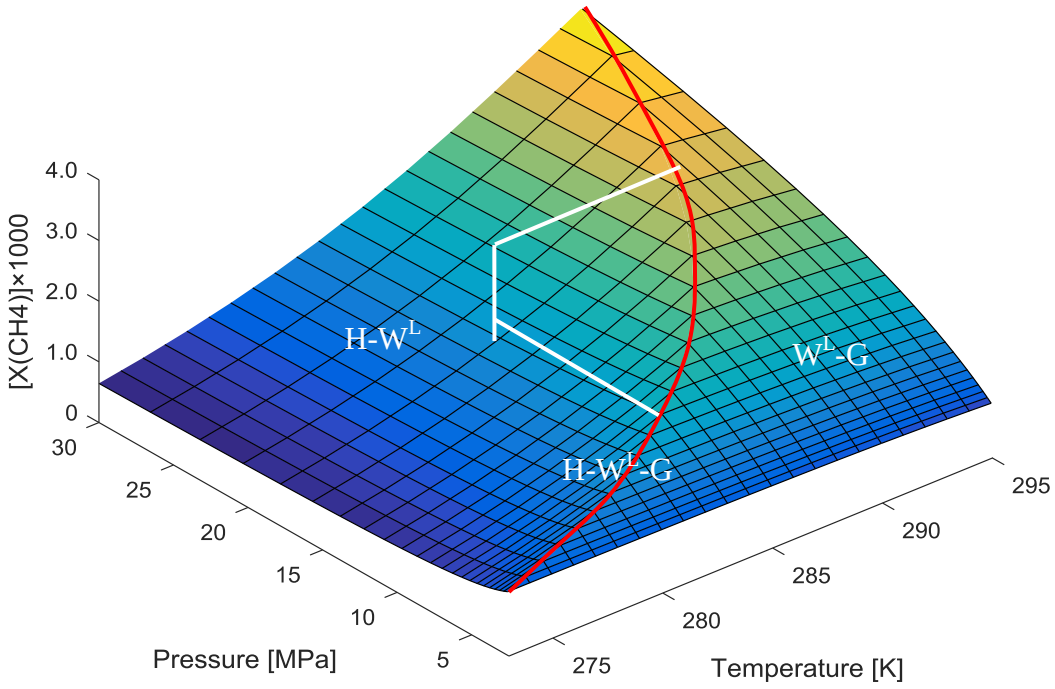

Figure 3.4 Methane concentration as an additional dimension of the hydrate phase boundary. Surfaces are defined based on data points generated using the simulator by Sun and Duan, 2007.

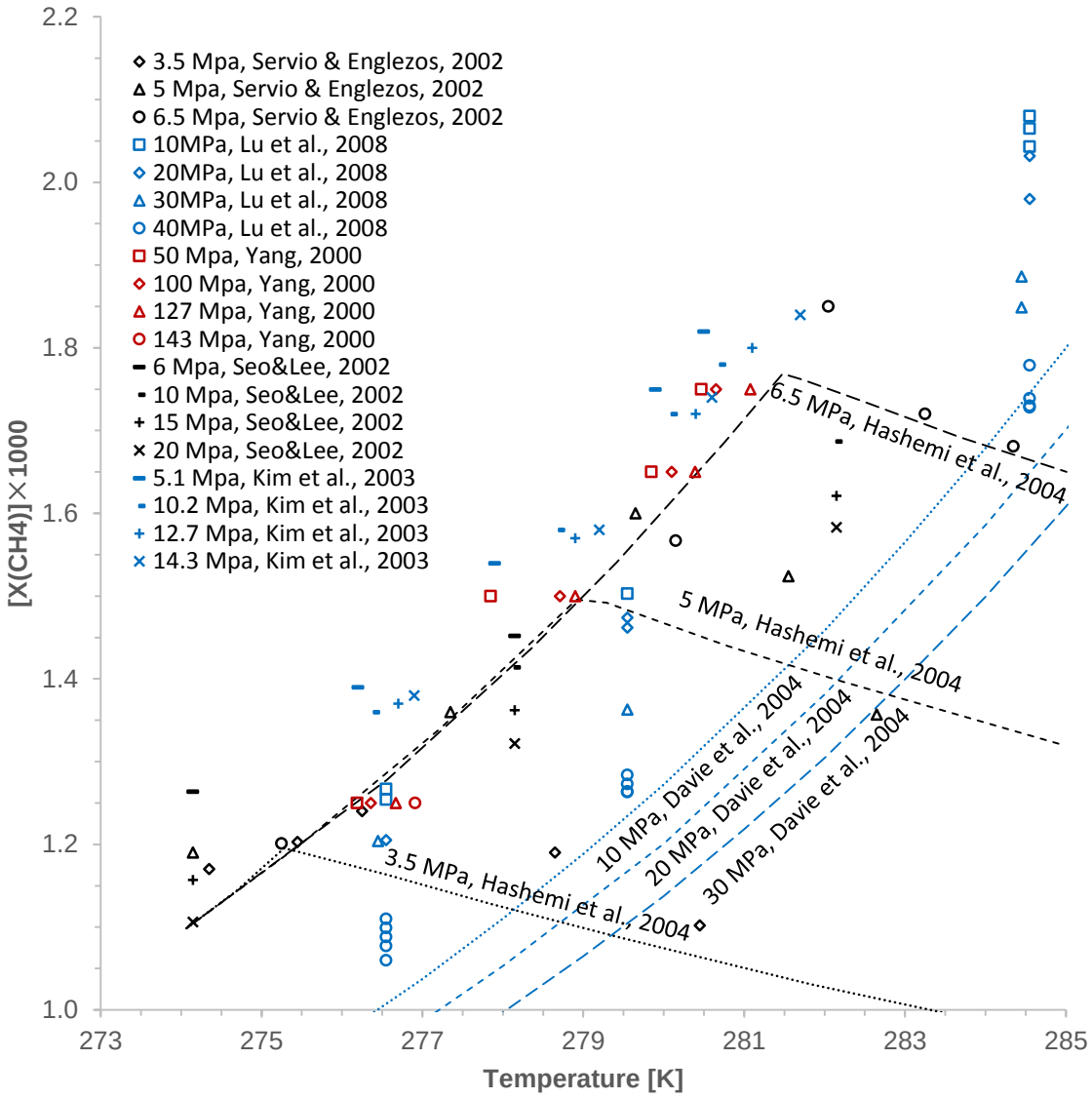

Figure 3.5 Methane solubility versus temperature (Seo et al. 2002; Yang et al. 2001).

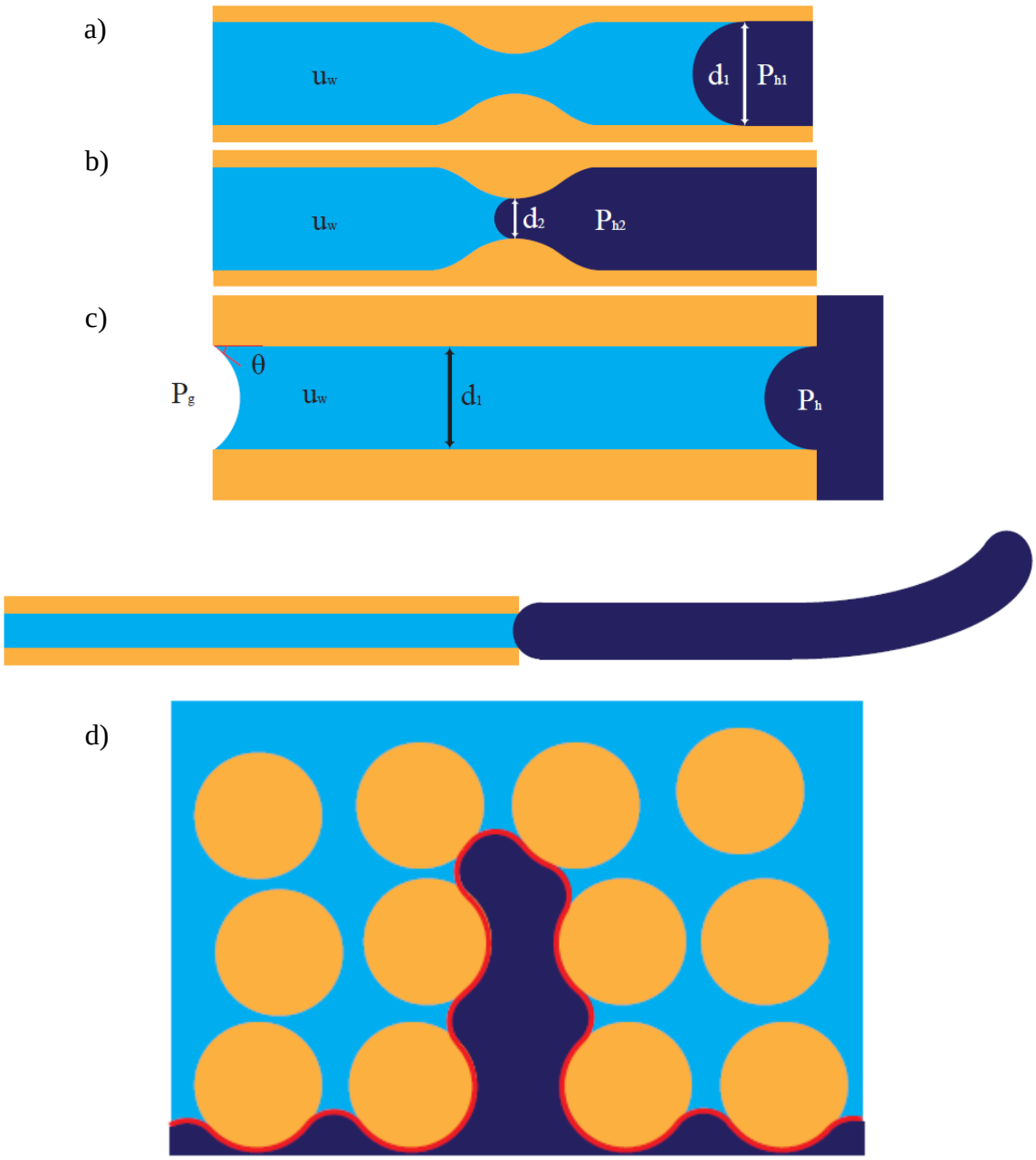

Figure 3.6 Pore-scale equilibrium between hydrate, water and particles in the sediments.

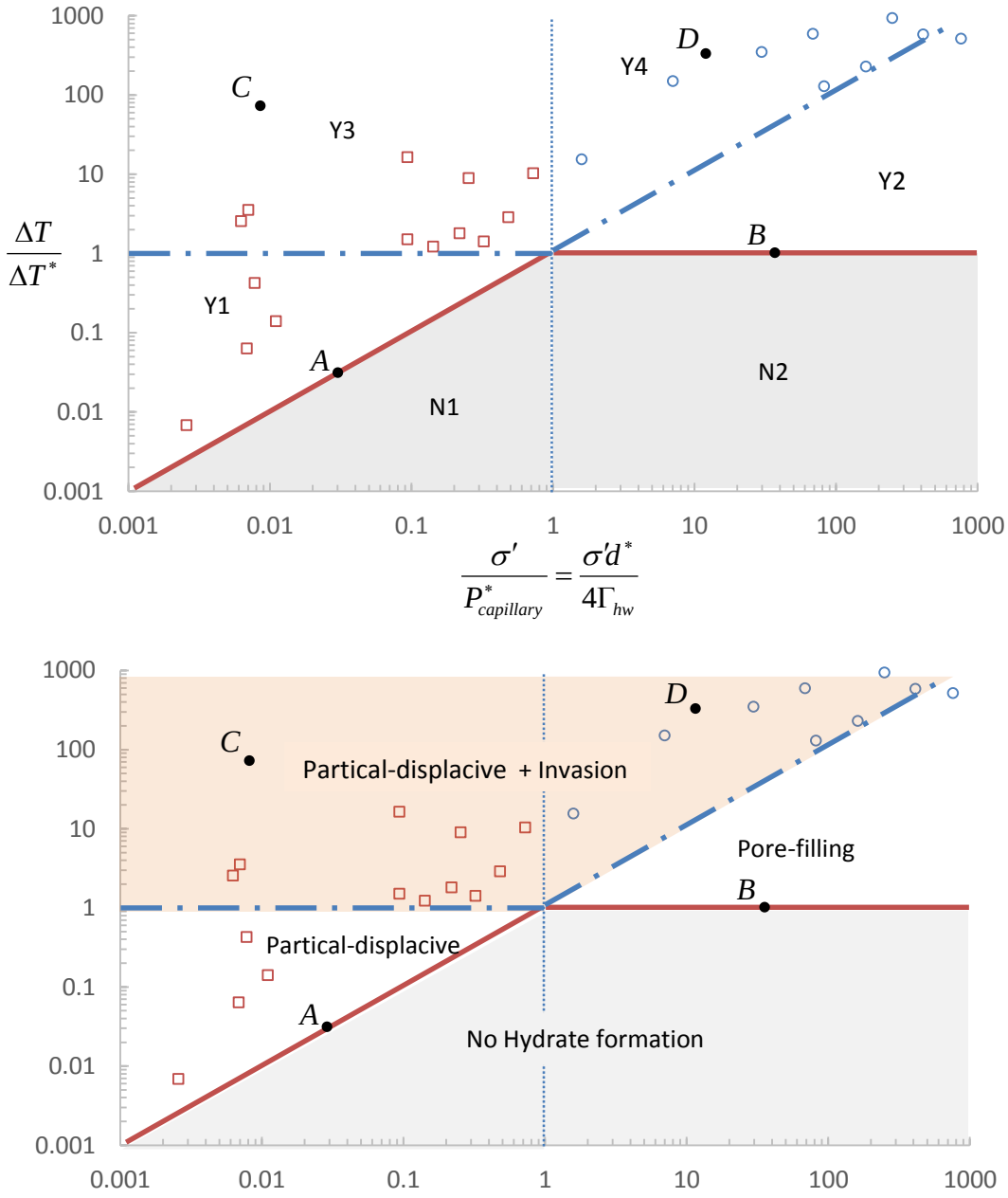

Figure 3.7 Temperature depression, capillary pressure and effective stress dominated hydrate morphology. The gray area illustrates the temperature depression. Analyses assume sufficient methane supply and that the methane concentration automatically reaches equilibrium. Particle displacive hydrate morphology (□). Pore-filling hydrate morphology (○).

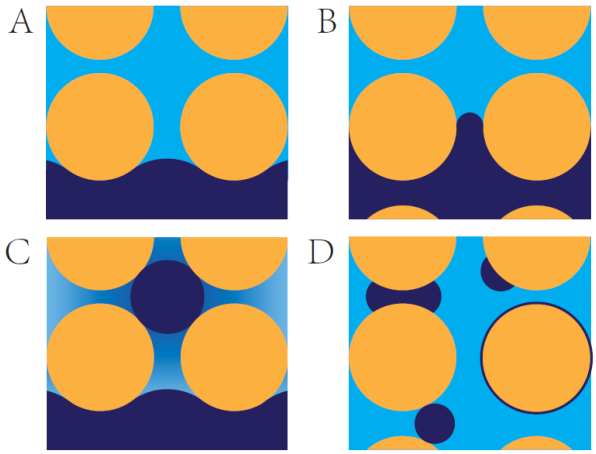

Figure 3.8 Particle level hydrate distribution that corresponds to the four points in Figure 3.7.

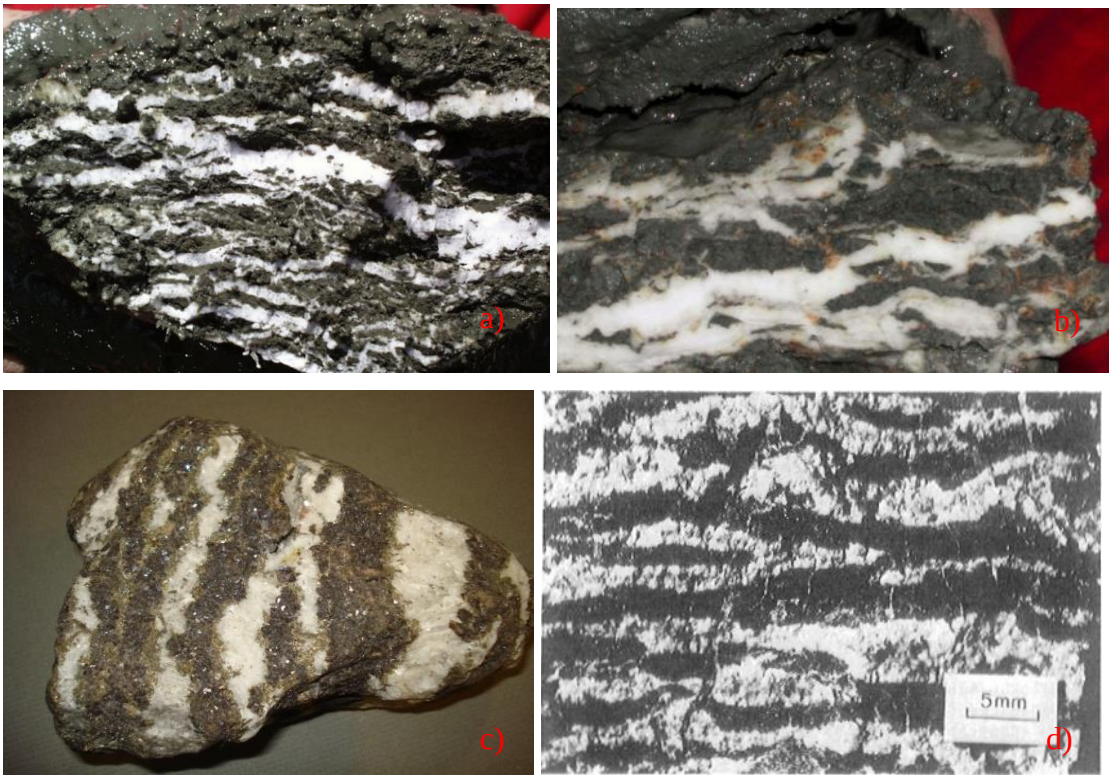

Figure 3.9 Analogue to natural Lisegang bands in ores. a) Hydrate at Hydrate Ridge, GEOMAR, 2012; b) Hydrate at the Gulf of Mexico, GEOMAR, 2012; c) Zinc ores, uwaterloo.ca/earth-sciences-museum; d) Dolomite bands in ores, (Merino 1984).

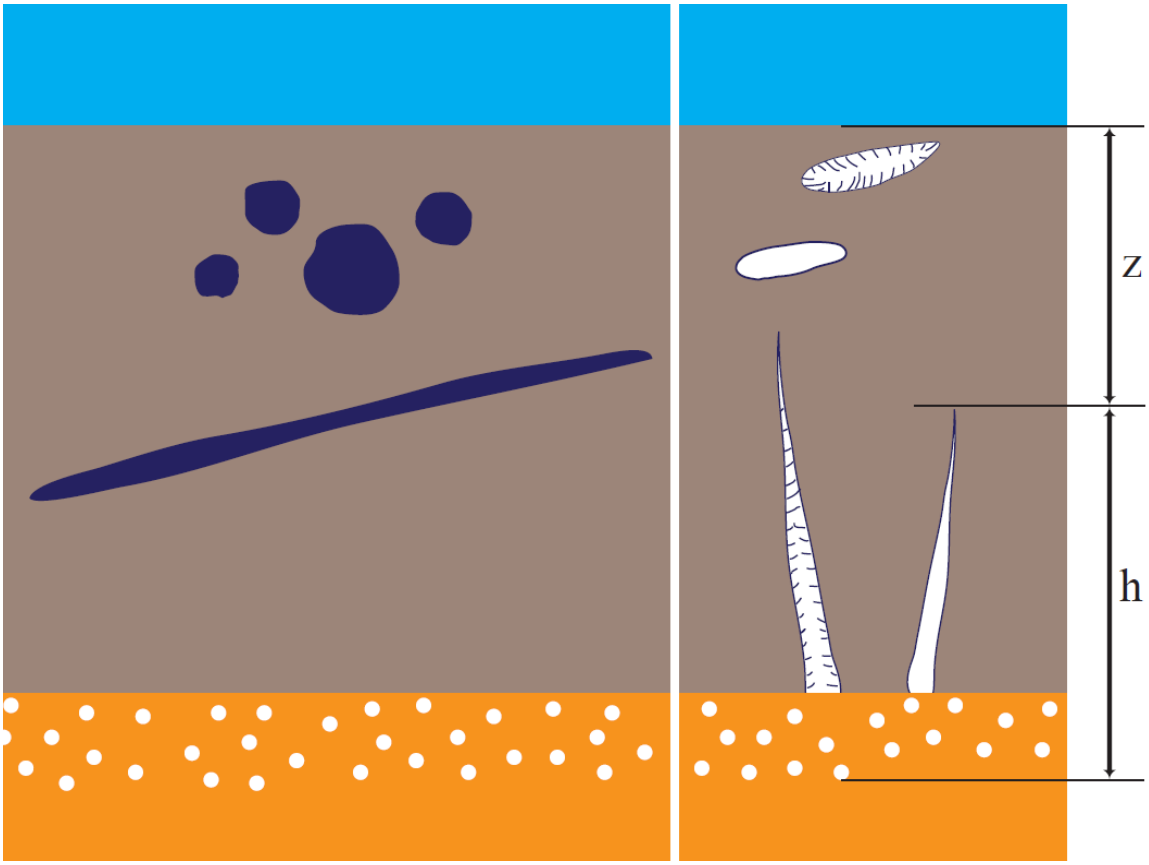

Figure 3.10 Gas supply to the hydrate formation front via diffusion and gas-driven fractures.

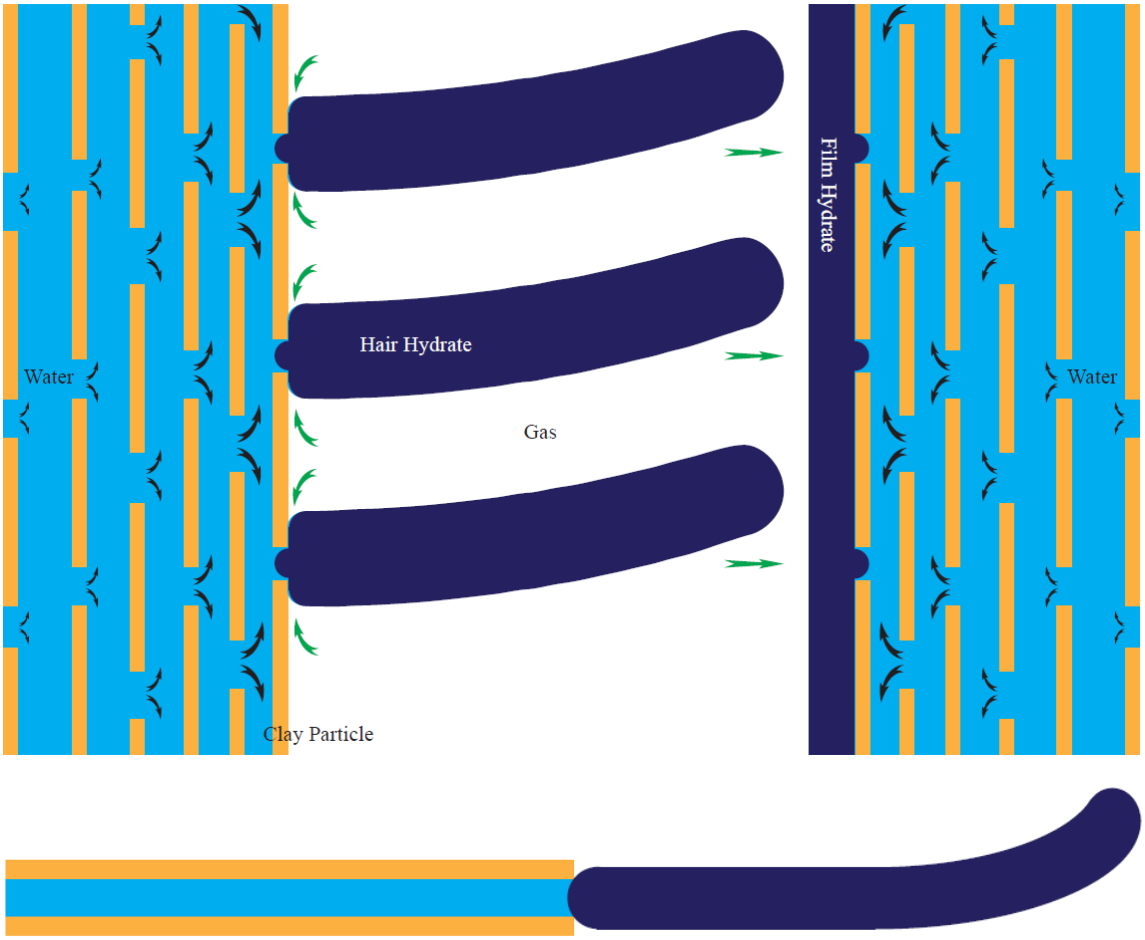

Figure 3.11 Hydrate crystal growth in gas-filled openings. Film and exo-pore patterns of crystal growth.

Figure 3.12 Natural examples and laboratory illustrations of exo-pore mechanisms. a) Hair ice (Hofmann et al., 2015); b) Frost flower on dittany (MacRae, 2010); c) Needle ice (Credit: Kelvin Freitas); d) Gypsum flower (Credit: Dave Bunnell); e) Gypsum needle (Alonso and Ramon 2013); f) Hydrate shell (Chapter 4).

CHAPTER 4

LABORATORY HYDRATE FORMATION IN FINE-GRAINED SEDIMENTS

4.1. Introduction

The global annual natural gas consumption was 3400 billion m^3 in 2015, with US consumption estimates of 760 billion m^3. The global accumulation of methane in gas hydrate deposits is 20,000 trillion m^3 (Boswell 2009), enough for 200 years of consumption assuming a growth rate of 2.2% per year. Hydrate-bearing coarse-grained sediments are preferred for potential gas production due to their relatively high saturation, high permeability and high mechanical stability (Moridis et al. 2009; Yamamoto and Dallimore 2008). However, fine-grained sediments host more than 90% of the total methane hydrate accumulation (Boswell and Collett 2006). The large amount of hydrates in fine-grained sediments requires careful consideration in the context of energy source, its potential role in the global carbon cycle and environmental implications. However, hydrate-bearing fine-grained sediments remain least understood and characterized compared to hydrates in coarse-grained sediments.

Methane hydrate formation in water-saturated sediments is inherently gas limited due to the low methane solubility in water (Waite et al. 2009). In addition, fine-grained sediments have small pores and low fluid conductivity and correspondingly long time-scales for gas transport. Consequently, gas hydrate formation develops over millions of years in fine-grained sediments (Xu and Ruppel 1999). In addition, the small pore size in fine-grained sediments decreases the possibility for nucleation and shifts the gas hydrate phase boundary to either higher pressure and lower temperature (Handa and Stupin 1992; Seshadri et al. 2001; Uchida et al. 2001). Segregated hydrate morphology in fine-grained sediments requires an additional driving force for hydrate growth whereby hydrate must overcome the effective stress and displace the sediment (Dai et al. 2012).

Several ocean drilling sites exhibit a narrower depth range for hydrate accumulation than initial estimates (Liu and Flemings 2011; Paull et al. 1996; Westbrook

et al. 1994). This deviation may result from the omission of capillary effects in earlier analyses.

Previous hydrate formation experiments in laboratory settings have focused on coarse-grained sediments (Ebinuma et al. 2005; Katsuki et al. 2006; Zhong and Rogers 2000). There are four common methods: dissolved gas, partial water saturation, ice-seeding and hydrate premixing (Waite et al. 2009). Hydrate formation with dissolved gas supply from water flux is inherently slow. The partial water saturation in specimens enables gas supply via connected pores. The utilization of ice as nucleation seeds significantly shortens the induction time. In addition, premade hydrate particles could be mixed with sand particles under low temperature conditions.

Many experiments use tetrahydrofuran THF as a methane substitute to avoid the guest molecule limitation in hydrate formation. The physical properties of THF hydrate are grossly similar to methane hydrate (Lee et al. 2007). In addition, experiments typically use carbon dioxide due to its higher solubility in water relative to methane (Katsuki et al. 2006; Tohidi et al. 2001; Zatsepina and Buffett 2001). There are advantages in other gas hydrate formers; for example, 3D CT images distinguish Xe-hydrate from water because it has high density of 1.8 g/cm^3 and Xe gas has a large atomic number(Jin et al. 2008).

Hydrate formation in sediments resembles water freezing in many ways, except that formation is not limited by gas transport. Both ice and hydrate extract water from the sediment by cryogenic suction. In the long term, molecular transport can gradually change the spatial hydrate distribution within sediments, concentrating the hydrate into fewer and larger masses (Ostwald ripening - (Myerson 2002)).

The morphology of hydrate in coarse-grained sediments can be pore-filling, cementing, coating or framing. By contrast, hydrate distribution in fine-grained sediments contains segregated nodules and veins. Electrical resistivity measurement of pressure cores illustrates inclined hydrate lenses in logging-while-drilling data (Cook et al. 2008). Photographs from a variety of drill sites and X-ray CT images from pressure cores corroborate the segregated lens or veins morphology of hydrate in fine-grained sediments (Ghosh et al. 2010; Lee et al. 2013; Rees et al. 2011).

The methane solubility in water decreases in the presence of hydrate; in fact, a 4mm thick methane hydrate lens can form every 1m of sediment given the change in methane saturation before and after formation (Jang and Santamarina 2016). Yet, the high hydrate saturations encountered in fine-grained deposits highlight gas supply by diffusion, advection, or along gas-driven fractures.

This chapter documents a comprehensive experimental study designed to emulate hydrate formation in fine-grained sediments. Experiments use a variety of different methods that could be observed in natural settings. Experimental observations enhance the understanding of natural hydrate formation in fine-grained sediments.

4.2 Laboratory Study: Hydrate Formation Methods

We explore different experimental methods to overcome some of the inherent limitations with gas hydrate formation in fine-grained sediments documented above and in Chapter 3. Table 4.1 lists all the experiments reported herein. Details follow.

4.2.1 Strategy based on THF hydrate

Strategy rationale. The miscible characteristic of THF with water enables the hydrate formation without limitation of water or guest molecule supply. Furthermore, THF hydrate formation could occur in atmosphere pressure under 4°C. THF hydrate formation develops in a variety of soil types, under similar thermal conditions (Table 4.1, Experiment 1-5). The liquid contents here in the experiments are all slightly above the liquid limit.

4.2.2 Strategy based on diatoms

Strategy rationale. This study recognizes the common coexistence of both hydrate and diatoms in fine-grained sediments (Clennell et al. 1999; Yun et al. 2011). Particles in diatomaceous earth have an inner pore arrangement that is dependent on the diatom

species. Figure 4.2a presents a scanning electron micrograph of the diatomaceous earth specimen used in the study.

This series of experiments use the inner space of the diatom particles as the storage space for high-pressure CO_2 gas (Experiments 6-8). The injection of water into the specimen then enables hydrate to form with a readily available source of gas already present in the sediment. Consequently, hydrate formation is not limited by the long time diffusion of guest molecules.

Experiment methods. The experiment starts from vacuum iteration to eliminate the influence of air. CO_2 gas is then injected into the chamber to fill the pore space of the specimen. Water addition on top of the specimen occurs before or after the temperature decrease to form hydrate.

4.2.3 Strategy based on ice-hydrate transformation

Strategy rationale. Ice can serve as gas hydrate nucleation seeds therefore the nucleation barrier is reduced. The enthalpy for CO_2 hydrate dissociation is between 57.7 to 63.6 kJ/mol (a mole of CO_2 hydrate is 44g + n 18 g, where n=5.75-6) (Anderson 2003). The latent heat in water/ice transformation is 6.05 kJ/mol, equivalent to 34.8-36.3 (6.05 n) kJ per mole of CO_2. Therefore, the ice-hydrate transformation is an exothermic process. In addition, pre-melting commences at the ice crystal surface when T=-33°C. The crystal structure does not fully solidify until temperatures reach 0K (Li and Somorjai 2007). Once the transformation from ice to hydrate occurs on the pre-melted ice surface, the generated heat melts more ice to release free water for hydrate formation and therefore creates a positive feedback loop to accelerate the process.

Experiment methods. We introduce ice into the sediments by the placement of premade ice lenses in dry specimens or freezing unsaturated specimen (Experiments 9-14). The system then moves into the hydrate stability field initiated by a pressure increase from 33 KPa. An ice-to-hydrate transformation occurs as temperatures gradually increase towards ice melting point.

4.2.4 Strategy based on gas injection directly into specimen

Strategy rationale. Natural gas plumes on the ocean floor indicate the presence of a free gas paths within the sediment (Gardner et al. 2009). Hydrate formation along the paths depends on the processes of the gas transfer from the fracture and the water supply from the sediments to the hydrate formation front.

Experiment methods. These experiments inject CO_2 into the water-saturated sediment to cause a gas-driven fracture where hydrate typically nucleates. Specimen preparation in Experiments 15 to 18 uses a consolidation pressure of 50 kPa, and the effective stress remains during the hydrate formation process through the compressed spring. Gas injection in Experiment 19 creates bubbles with the volume two to three times of the specimen. Experiment 20 uses a porous cap on the top of the specimen to reduce the volume expansion of the specimen.

Research highlight. The back flow of water into the injection needle in these series of experiments can potentially clog the tube if hydrate forms inside. Therefore, the introduction of liquid CO_2 in the experiment provides the experiment with a stable gas resource. The gasification of liquid CO_2 also compensates for the gas consumption and leakage during hydrate formation. Alternatively, liquid CO_2 stabilizes the systems pressure. Liquid CO_2 sits on the bottom of the opening due to its higher density in comparison to CO_2 gas. Therefore, the relative position between liquid CO_2 and the sediments in the experiments resembles the spatial relationship between the gas source and the hydrate bearing sediments in nature.

4.2.5 Strategy based on long term diffusion

Strategy rationale. Hydrate formation from CO_2 saturated water in fine-grained sediment is of interest in the study. Diffusion is a crucial component in the gas supply process to saturated fine-grained sediments. Saturation of a 10mm specimen with CO_2 take place over 7 days. The specimen in Experiment 21 and 22 are under pressure no less than 3 MPa for 20 days and 10 days respectively before temperature depression.

4.3 Results and Observations

Each experiment is a unique entity in this research. However, due to the large number of experiments, this section reports common features rather than individual experimental results. Table 4.2 details the basic information of the specimen in the experiments.

4.3.1 Experimental setup

Schematic and measurement. The schematic in Figure 4.1.a presents the flexibility of the system to inject gas and gas saturated water to both the top and bottom of the chambers. Figure 4.1.b illustrates the real chambers mounted on a stiff frame. Figure 4.1.c displays the section of the specimen chamber. A spring applies the effective stress on the specimen. The position of two thermocouples enables the measurement of both temperature and temperature gradient. Pressure transducer connected to the top of the chamber provides pressure data during the whole process.

CT scan related considerations. This study uses X-ray computed tomography to obtain a better insight into the hydrate formation process in sediments. We design and fabricate three identical thin-walled (3.5 mm) aluminum chambers (Ø 40mm, H 140mm) to sustain pressures up to 30 MPa (Figure 4.1c). Key considerations include the balance between strength, material X-ray transparency, ease of operation and sample size effect. Additionally, an adapter that attach the aluminum chambers to the rotary stage allows minimal specimen chamber movement and multiple scans at the same position, which enables image comparison studies.

Scan process. The CT scan time is managed to be less than 35 minutes to restrict the temperature increase during the process to be no more than 7°C to ensure that the hydrate remains within the stability field. The insulation uses foam, which is transparent in front of X-ray, to coat the chamber to reduce the heat absorption from the environment.

CT image interpretation. The brightness of the pixel corresponds to the attenuation coefficient of the material in X-ray images. There are 6 different experimental

phases: the aluminum chamber, the saturated specimen, water, hydrate, liquid CO_2 and the gas-filled void (the attenuation coefficient ranges from high to low). The histogram of hydrate, water and liquid CO2 overlaps due to the similarities between the attenuation coefficients of these phases. Therefore, it is not credible to differentiate them from each other based on the pixel intensity alone. Beam hardening and ring artifacts further decrease visibility. However, results indicate the solid phase hydrate can maintain an irregular shape, compared to the pool-like structure or the smooth and curved surface of the liquid phase water/CO_2.

4.3.2 Pressure and temperature signatures

Experimental phase boundaries. There are three phase boundaries in the CO_2 hydrate formation experiments: water/ice, liquid/gas CO_2, and the hydrate phase boundary. Figure 4.3 presents the experiments typical pressure-temperature curves. Hydrate formation is always accompanied by a thermal spike due to the exothermic reaction.

Thermal spike in THF hydrate formation. THF hydrate formation produces a thermal spike that remains for between 30 minutes when formed in silica flour to several hours when formed in bentonite. Two factors control this timescale, the amount of THF hydrate and the rate of heat transfer to the environment. The heat transfer could be considered at a constant rate. Therefore, the length of the thermal spike is approximately proportional to the amount of formed hydrate produced by the experiment.

Thermal response in CO_2 hydrate formation. The ice-to-hydrate transformation occurs at a temperature lower than the ice melting point (-1.5 °C in Experiments 10, 13 and 14; -1.7 °C in Experiments 11 and 12). The shortened thermal spike in CO2 hydrate formation experiments is due to the slow guest molecule supply in comparison to THF hydrate formation. The end of a thermal spike does not indicate the end of hydrate formation. The long-term formation and evolution of hydrate shapes in sediments continue throughout the course of these experiments. Additional sudden pressure increases as shown in the trajectory types C, D, E, and F in Figure 4.3 may also trigger the formation process.

Hydrate dissociation. Experiments use two different technics to trigger hydrate dissociation: depressurization and thermal stimulation. Hydrate dissociation by depressurization exhibits a temperature decrease due to the endothermic characteristics. The temperature can decrease to a point lower than the water freezing point (see Experiments 8, 10 & 23). Therefore, water released from hydrate dissociation in these cases freezes. The overall hydrate-ice transformation process is endothermic that it requires a heat supply from the outside environment to sustain. Ice that covers the hydrate surface can also hinder hydrate dissociation.

The second technic increases the temperature to trigger hydrate dissociation. Any temperature increase in a closed constant-volume system could trigger hydrate dissolution. When hydrate is present, the pressure increase induced by thermal stimulation differs significantly from the gas law governed pressure response. Therefore, hydrate needs to dissociate and release a particular amount of gas to maintain the stability of the residue hydrate. By contrast, a temperature decrease promotes hydrate formation.

Liquid CO_2. Pressure-temperature trajectories typically follow the liquid CO_2 phase boundary when liquid CO_2 is present, noted in Experiments 15-17. This phase boundary plays an important role in geological CO_2 sequestrations.

Observations show that the PT trajectory frequently diverges from the phase boundary. Potential explanations for this divergence include:

- Spatial mismatch between the sensor and physical processes in the specimen. The pressure reaches equilibrium quickly. Therefore, the pressure, but not the temperature in the chamber could be considered homogeneous. The position of the temperature sensor does not match the points of phase transition.
- Imperfect sensor calibration.
- The response time lag of the sensor.
- Chemical impurities that affect the phase boundary.
- Heat exchange in the chamber and with the environment.
- Coexistence of hydrate formation/dissociation and CO_2 liquefaction/gasification.

4.3.3 Pore size effect

Temperature depression. The degree of temperature depression and induction time increase with the decrease in particle size due to the pore size effect (Experiments 1-4). Segregated hydrates can form outside the pores, either on top of the specimen, in the opening created by gas injection, or alternatively in the cavities that existed at the beginning of the experiment. Observations note thermal spikes in hydrate experiments using both silica flour and some diatomaceous specimens. However, there is no visible segregated hydrate structure observed in 3D X-ray images potentially due to the relatively large pore size (Figure 4.11).

Nucleation. Gas hydrate nucleation in small pores subjects to limitation due to insufficient guest molecules available in the limited space (Chapter 3: Equation 3.2 and Figure 3.1). Observations note that CO_2 hydrate experience longer induction time than THF hydrate for two reasons. On one hand, the THF solution is in stoichiometric ratio, therefore, the critical pore size collapses to the critical nuclei size. On the other hand, the presence of bubbles in the THF specimen, which cannot be completely removed, provides enough pore space for nucleation. However, these bubbles at the specimen preparation stage contracts and dissolves into the water due to the pressure increase in CO_2 hydrate experiments.

Illustration of pore size effect. Figure 4.4 displays the typical response of a P-T trajectory affected by the pore size effect. The P-T trajectory follows the shifted phase boundary in an equilibrium state subsequent to hydrate formation associated with temperature decrease. However, the curve deviates from the shifted phase boundary to the bulk hydrate phase boundary with temperature increases.

4.3.4 Morphology

Porous structure. The porous structure is the key feature of massive hydrate formation. The maximum experimental duration is one month in this study (due to experimental instabilities/control); therefore, the time does not allow the formation of a

non-porous hydrate mass with the same size in this study (Figure 4.6, 4.7, 4.10, 4.15 & 4.16). The porous structure develops in Experiments 6, 9, 11, 12, and 16-22. The X-ray images and photos demonstrate the porous characteristics of hydrate in Figures 4.6-4.10. In Experiment 11, the none-clogging gas path from the upper space to the ice-hydrate transformation front contributes sufficient guest molecules. This growth pattern resembles hair ice (Chen and Grey 2008). Parallel experiments do not demonstrate this phenomenon.

Striped patterns. Two hydrate shells exhibit striped patterns grow on the superior surface of the specimen in Figure 4.5. The striped surface feature exists in other hydrate formation experiments and pipe clogging cases (Makogon 1997).

Water migration. The location of hydrate formation can be different to the initial lenses in Experiments 11 and 12 (Figure 4.6 and 4.7). The difference in shape results from two factors. Once the first nuclei stabilize and start to grow, they extract all the nearby free water. Furthermore, the heat generated from the hydrate formation front diffuses to the nearby field and releases the temperature depression around the lens. Therefore, the hydrate formation centers the first nuclei. The shape of the final hydrate mass should be similar to the initial ice lens if hydrate forms a thin shell on the ice surface, a situation not observed in the experiments.

Capillary suction. Capillary suction in the presence of dry sediments competes for water with cryogenic suction. The lens size decreases during hydrate formation in Experiment 12 because of the suction of water into the dry specimen. The arching-shaped cracks result from both the volume contraction of the sediment upon water absorption and the gravity of the upper layer. Observations of a parallel experiment note the complete absorption of a thinner ice lens into the sediment.

Surface property influence. We use fumed hydrophobic silica in Experiment 13 to study the influence of mineral surface properties on hydrate formation and dissociation. The sequence of CT scans presents the evolution of the lens morphology (Figure 4.13). The lens shape sphericity increases during the transformation from ice to hydrate or from hydrate to water due to membrane effect induced by surface tension. The sphericity then decreases during water-to-hydrate transformation. Section 4.3 details the thermal and

mass analyses of this experiment. Note that the diameters of the ice lenses are smaller than half the size of the aluminum chamber (33 mm). This guarantees a completely hydrophobic environment.

4.3.5 Topology

THF hydrate. When THF hydrate forms, guest molecules are readily available in the stoichiometric solution. Consequently, thermal boundary conditions and sediments properties, such as pore size and solution content control the hydrate topology in the sediments. Figure 4.11 displays the THF hydrate structure in sediments with different particle sizes. The increase of particle size induces the decrease in the number of hydrate lenses and an increase of lenses distribution heterogeneity. The thermal dissipation rate to the environment affects the hydrate distribution. The hydrate lens topology consists of the densely packed lenses on the periphery and the loosely distributed lenses towards the center of the specimen in the middle. In addition, the heat dissipation through the air in Fig 4.12 is slower than water as seen in Fig 4.11-3. The air bath condition provides an increased duration for the hydrate to extract the THF solution from the nearby sediments. Therefore, hydrate formation in an air bath facilitates larger and more concentrated hydrate lenses, in comparison to the water bath.

CO_2 hydrate. Ice lenses in figure 4.6 mainly form on the periphery of the frozen specimen at the beginning of the experiment (upper images). Massive porous hydrate with stripe patterns forms by a process of water extraction from melted ice and the compression of the sediment (lower images). The initial ice lens topology in this case does not determine that of the transformed hydrate mass. The topology is an important indicator of the formation history. By contrast to THF hydrate, guest molecule availability in CO_2 hydrate formation and gas supply methods become more important in the determination of hydrate topology. Results of gas injection experiments indicate that hydrate forms whenever gas interacts with the sediments. CO_2 saturated specimens develop a polygonal pattern hydrate formation in Figure 4.9.

4.3.6 Sediment consolidation and relaxation

Hydrate mass pulls water from the sediment and consolidates the soil skeleton via cryogenic suction. Figure 4.14 displays the consolidation effect observed in Experiment 4. The effective stress is a function of the temperature depression (Chapter 3). These results indicate a higher volume of produced hydrate in Image 4 in comparison to Image 2. This experiment indicates hydrates increased ability to extract fluid at lower temperatures. Images 5 and 6 demonstrate the specimens structure at one hour and one-day time points post dissociation respectively. The sediment in image 6 exhibits less mass concentration spots, which indicates the sediment swelling. The sediment does not absorb all the released fluid when hydrate dissociates. Therefore, there is usually free water/THF solution on the surface of the specimen by the end of the experiment. Consequently, hydrate dissociation does completely negate the consolidation effect generated by hydrate formation.

4.3.7 Exclusion in crystallization

Hydrate formation, like ice formation, excludes most of the impurities. Hydrate formation in salt water increases the salinity of the solution due to ion exclusion. Similarly, dissolved air in water functions as a type of impurity and is excluded from hydrate growth. The bubbles in the ice lens in Fig 4.7 form due to the exclusion of gas in the freezing process. The concentrated bubble distribution in the center of the ice lens indicates the hydrate formation history due to heat transfer. The phenomenon also exists in the THF hydrate formation process, as noted in Figure 4.14. However, the phenomenon does not occur in the CO_2 hydrate formation process. There are two possible explanations for the lack of bubbles within CO_2 hydrate lenses. The CO_2 hydrate formation in this study is mostly porous. In addition, the rate of air migration from the hydrate formation front to the outer field is comparable with the CO_2 supply rate to the formation front. Alternatively, there is sufficient time for the excluded air to diffuse out from the solution prior to the nucleation of gas bubbles.

4.3.8 Mass transportation upon dissociation

CO_2 hydrate dissociation generates massive gas driven fractures (Figure 4.8, 4.14, 4.15 and 4.17). Results of Experiments 11 and 15-22 note the presence of both free water on the surface and gas within the fractures and cavities of the specimen. The surface water does not flow back into the specimen, despite the positive effects of gravity. Therefore, the fractures in the specimen cannot reach the surface after gas release. Following depressurization, fractures that previously housed hydrate now contain water released from hydrate dissociation. This change occurs when the pressure and temperature moves away from the CO2 hydrate stability field.

4.3.9 Solid, liquid, and gas

The fundamental difference between the solid phase and liquid phase assists with hydrate formation confirmation. Solid phase ice and hydrate have both shear and tensile strength. Therefore, they can bear some loads from the external environment and maintain a sharp surface and connected porous structure that includes massive irregular cavities. The slurry in Figure 4.10, is unable to keep the thin shell-like structure stable without the support of a skeleton. There must be a layer of hydrate on the interface to support the specimen. By contrast, liquid water or CO2 typically display rounded surfaces which can sometimes include small (≈1 mm), spherical gas bubbles. The reflection of light from the liquid water surface is stronger than from the solid surfaces of ice and hydrate therefore provides additional evidence of phase transitions in visualization chamber. CT images display a significant difference in pixel brightness between the gas and liquid phases, primarily due to gases lower density in comparison to liquid. However, geometrical shape alone is insufficient to differentiate between liquid and gas bubbles on CT images.

4.3.10 Dynamic hydrate growth and dissociation

Hydrate formation evolution. The injection of liquid CO_2 stimulates crack propagation over the course of three days illustrated in Figure 4.15. A hollow structure

hydrate gradually fills the crack, and the hollowness of the hydrate decreases with time. The liquid CO_2 exists until the depressurization. Water extraction from the sediment is less than that in the THF hydrate formation experiment with similar conditions. Therefore, neither water nor guest molecules are limited within the system. The reason that hydrate ceases to form is that the water and guest molecules cannot meet each other efficiently. The hollow hydrate structure adjusts its shape to take the load transferred from the sediment.

Other dynamic processes. Figure 4.16 (Experiment 22) demonstrates the evolution of X-ray projections during the hydrate formation process. The time lapse images demonstrate the hydrate formation on the specimen surface, the lenses inside the specimen and the hollow gas hydrate structure that invades into the specimen. Figure 4.17 illustrates the evolution of projections during the dissociation, crack formation process and the gas extraction path.

4.4 Analysis and Discussion

4.4.1 "Reservoir" simulation

Simulation - Fundamental physics. The quantified mass and thermal analyses of the experimental process is critical to the understanding of the formation and dissociation of hydrate. The physical analyses model recognizes the coexistence and coupling effects of the physical processes including water and gas migration, heat transfer within different components and the sensor response delay.

Mass analysis

Procedure. Figure 4.17 details the procedure used in the analysis. The analysis starts from a steady state or at least a quasi-steady state. The calculation of test chamber gas density uses the Gas Law (http://www.peacesoftware.de/). Calculation of the total mass of gas-phase CO2 as a function of time assumes that the liquid and solid phases in the chamber are incompressible and that the volume of the gas phase is constant. If we

assume that there is no gas leakage, a mass change of gas phase CO_2 indicates a hydrate related process.

The influence of hydrate formation and dissociation on the gas-phase mass has a cyclic trend when the temperature oscillates with time. By contrast, leakage demonstrates a global trend of gas loss (Figure 4.19). We consider the leakage of gas from the analysis by the subtraction of the general CO_2 content loss trend versus time. The difference between the measured data and red solid line reflects the hydrate formation and dissociation in the experiment. Mass conservation then calculates the rate of hydrate formation/dissociation.

Thermal analysis

Physics. Figure 4.19 illustrates the thermal analysis procedure. Thermal effect accompanies all of the processes in the experiments which include: gas injection, gas release, environmental temperature oscillation, hydrate formation and dissociation. Pressure quickly reaches equilibrium; however, the temperature does not reach this point within 5 hours. Observations also note the thermocouple response time lag, which can impact on results. Thermal couples can result in a damped thermal peak/valley during transient thermal processes. This phenomenon occurs when the specific heat of the medium is much lower than that of the thermal couple. Therefore, a more accurate gas temperature calculation uses the gas law from the pressure response of the system, in comparison to the direct temperature measurement.

Physics model. If we assume that the thermocouple tip has a cylindrical geometry, and the heat exchange between the thermocouple and the environment could then be expressed as:

$$\frac{dQ}{dt} = \pi r_t^2 l \rho_t c_t \frac{d\left(T_t(t)\right)}{dt} \tag{4.1}$$

$$q[t] = \frac{dQ}{dt} = h 2\pi r_t l \left[T_e(t) - T_t(t)\right] \tag{4.2}$$

Where Q is the heat transferred from the environment to the thermocouple; r_t is the radius of thermocouple; ρ_t is the density of thermocouple; c_t is the constant volume heat capacity of thermocouple; T_t is thermocouple temperature; t is time; h is the heat transfer coefficient between thermocouple and environment; and T_e is environmental temperature.

Simulation result of the thermal couple response in gas during the gas injection process. When the gas temperature increases or decreases, the heat generated or lost should be redistributed to the whole sediment:

$$\Delta T_{sedi} = \Delta T_g \frac{\Phi \cdot \rho_g \cdot c_g}{\Phi \cdot \rho_g \cdot c_g + (1-\Phi) \cdot \rho_{\text{mineral}} \cdot c_{\text{mineral}}} \tag{4.3}$$

Where ΔT_{sedi} is the overall sediment temperature change; ΔT_g is the gas temperature change due to gas injection or release; Φ is porosity; ρ_g is the density of gas; c_g is the constant volume heat capacity of gas; $\rho_{mineral}$ is the density of sediment mineral; $c_{mineral}$ is the constant volume heat capacity of the sediment mineral.

Thereafter, the heat diffuses to the adjacent ice/hydrate lens and the environment.

$$\frac{\partial T}{\partial t} - D\left(\frac{\partial^2 T}{\partial x^2} + \frac{\partial^2 T}{\partial y^2} + \frac{\partial^2 T}{\partial z^2}\right) = 0, \; D = \frac{k}{\rho C_p} \tag{4.4}$$

Where x, y, z are the coordinates; D is diffusion coefficient; k is the thermal conductivity.

Simulation of the thermal processes and its consequent effect on the experimental components uses the COMSOL Multiphysics software. Fig. 4.20 displays these results.

4.4.2 Discussion

Diatomaceous earth. Temperature and pressure trajectories and related analyses indicate that hydrate formed in all diatomaceous earth specimens tested as part of this study. Yet, there are not clear signs of segregated hydrate with the exception of the two hydrates lenses on the top of the specimens (Experiment 7). Small hydrate crystals distributed in pores do not merge into a large segregated hydrate mass that could be distinguished in CT images. In part, this is due to short laboratory time scales that do not

allow for Ostwald-ripening, in addition to the generation of high effective stresses in small rigid chambers.

Ice-to-hydrate transformation. The success of hydrate formation experiments with ice-to-hydrate transformation strategy highly depends on the clear path of gas-supply. The pre-melting of the ice surface and exothermic feature releases free water from the ice crystal lattice and enables water migration to the hydrate formation front or pores in dry sediment. Hydrate formation, which heavily relies on the relatively slow heat dissipation is slower than the instant water migration process due to capillary suction. Therefore, the final hydrate mass shape reflects the water migration history rather than simply resembling the initial ice lenses.

Gas injection. Laboratory produced hydrate that uses gas injection methods aims to emulate natural conditions (Figure 4.23). The liquid CO_2 represents the gas zone/resource layer under the hydrate-bearing layer, which supplies gas to the hydrate growth within the fine-grained sediments. The gas flow through the openings in fine-grained sediments is a transient process. However, the diffusion of released gas back into the sediment is negligible by laboratory time scales. By contrast, hydrate in fine-grained sediments loses gas to the hydrate formed outside the sediment due to the shifted phase boundary in the pores when effective stress is present. Therefore, a stable gas source under the bottom of the sediments is critical to a successful experiment. The gas resource can also be continuous gas injection from the bottom of the sediments. Yet, backflow and injection needle clogging are common problems with this technique.

Reproduction of natural conditions. Laboratory hydrate formation in fine-grained sediments that emulates naturally formed hydrate should create a gas resource inside or underneath the fine-grained sediments. Either a chemical or pressure gradient then drives the gas into the sediment. It is also important to guarantee that there is no quick path for gas to escape the fine-grained sediments, although this is difficult to achieve in laboratory conditions. A hole with a 1mm diameter can very effectively transport gas through the sediments. Note the hydrate in clayey sediments acts as a buffer during the upward gas migration. The existence of hydrate in sediments is because of gas supply or, a historically supply below the hydrate stability zone. Otherwise, the nonstop loss of gas

into the ocean floor from the top of hydrate-bearing sediments would eventually deplete the reservoir. This explains the rareness of natural CO_2 hydrate-bearing sediments.

Experimental findings. The gas that reaches the top of the sediments forms hydrate with a small amount of free water (very common in effective stress conditions). This is an easier process than hydrate formation by water extraction from the sediments. Once hydrate forms on top of the sediments, the further growth competes with the hydrate inside the sediments for water resources within the system.

Fracture accelerated hydrate formation. Gas driven fractures form when the gas pressure under hydrate bearing layer increases to a certain degree. Hydrate forms when gas reacts with water in the sediment and can potentially clog the gas path. The further formation of hydrate consolidates the nearby sediment. This increases the likelihood of gas driven fractures in the far field. The loop continues to form high saturation rate hydrate-bearing fine-grained sediments. This mechanism is significantly more efficient than diffusion controlled hydrate formation.

Porous and thin-layer structure. Massive hydrate formation in the experiments always starts with a porous strip structure, which has a clear path to supply gas to the formation front. If a solid layer of hydrate forms between the vapor phase CO_2 and the sediment/water, further hydrate growth has to be through gas diffusion to the water/hydrate interface or water diffusion to the hydrate/gas interface. The thin layer of hydrate is no more than 120 microns in experiments without the presence of sediments (Subramanian 2000).

4.5 Conclusions

Most hydrate accumulations in nature are found in fine-grained sediments. Hydrate formation in fine-grained sediments is limited by pore size effect and gas transport. We used different strategies to accelerate the supply of guest molecules to the hydrate formation front, to overcome the nucleation barrier, and to explore long-term diffusion controlled CO_2 hydrate formation. This extensive study confirms the great

challenges in hydrate formation in fine grained sediments in relatively short laboratory time scales. Other conclusions from this study follow:

- Hydrate formation in fine-grained sediments is inherently dispersive (Chapter 3).
- Gas supply to the hydrate formation front controls the rate of hydrate formation.
- Hydrate formation extracts water from the sediments, and the surrounding medium becomes overconsolidated. The compaction effect remains upon hydrate dissociation.
- Freshly formed hydrate is highly porous. The pervious hydrate structure provides an effective path for gas migration to the hydrate-sediment interface and sustains rapid hydrate growth.
- A gas driven opening imposes extension to the sediment at the tip, the local pores enlarge, the void ratio increases, more water is available and hydrate forms more readily at the tip.
- The inner pores in diatomaceous earth may serve as widely distributed gas storage. Therefore, hydrate formation in diatomaceous earth does not rely on long-distance gas supply from the far field.
- Dry fine-grained sediments extract water from melting ice faster than the rate of hydrate formation; therefore, ice-to-hydrate transformation has limitations and the hydrate mass that forms exhibits different morphology from the original ice mass.
- A hydrate shell forms around gas-filled openings in soft clays. Further hydrate growth invades into the sediment to form lenses or exo-pore growth takes place into the opening.
- The temperature depression evolves over time in both hydrate formation and dissociation process to reflect pore size effects.
- The exclusion of foreign species during hydrate growth captures the history of hydrate formation.

Table 4.1 Experiment List

No.	Sediment type	P-T Trajectory Type [a]	Thermal Boundary	Related Images	Chamber type	Liquid Content [b]	Hydrate Morphology	Notes
THF Hydrate Experiments								
1	Silica Flour	A	Water Bath	4.11-4	X-ray [c]	40%	Pore-filling	Mole ratio of THF/Water: 1/17 Temperature depression to 2 °C to form hydrate
2	Diatom	A	Water Bath	4.11-3	X-ray	150%	Lenses	
3	Kaolinite	A	Water Bath	4.11-2	X-ray	60%	Lenses	
4	Bentonite	A	Water Bath	4.11-1, 4.14	X-ray	300%	Blocks	
5	Diatom	A	Air Bath	4.12	X-ray	120%	Lenses	
Particle Inner Pore Space Utilization (CO_2 hydrate)								
6	Diatom	B	Copper coil	--	Visualization [d]	0%⇨40%	Small Crystals	Water injection into dry diatom specimen inside/outside hydrate stability field
7	Diatom	B	Copper coil	4.5	Visualization	0%⇨30%	Hydrate Flower	
8	Diatom	B	Air Bath	--	X-ray	0%⇨40%	Small Crystals	
Ice-to-Hydrate Transformation (CO_2 hydrate)								
9	Kaolinite	C	Copper coil	--	Visualization	--	Porous Lens	Ice lens in groove of unsaturated kaolinite
10	Kaolinite	C	Copper coil	--	Visualization	60%	Shell	Mini-sample with D=6mm, L=20mm
11	Kaolinite	C	Air Bath	4.6	X-ray	55%	Porous Block	Unsaturated
12	Kaolinite	C	Air Bath	4.7	X-ray	--	Porous Lens	Dry kaolinite with ice lens embedded
13	Hydrophobic silica	C	Air Bath	--	X-ray	--	Porous Lens	Hydrophobic silica with large/small ice lens embedded
14	Hydrophobic silica	C	Air Bath	4.13	X-ray	--	Lenses	
Gas Injection into the Bottom of Specimens (CO_2 hydrate)								
15	Diatom	D	Air Bath	4.8	X-ray	40%	Porous lens	1. Consolidation pressure: 50KPa 2. Gas injection into the bottom of consolidated specimens
16	Layered specimen [e]	D	Air Bath	--	X-ray	48%	Porous lens	
17	Layered specimen [f]	D	Air Bath	4.15	X-ray	48%	Porous lens	
18	Diatom	E	Air Bath	4.22	X-ray	40%	Porous lens	

19	Kaolinite	E	Air Bath	4.10	X-ray	150%	Lens, shell	Gas injection into the bottom of the slurry specimens
20	Kaolinite	F	Tygon Coil	4.9	X-ray	150%	Lens	
Long Term Diffusion (CO_2 hydrate)								
21	Bentonite	B	Tygon Coil	4.4	X-ray	2000%	Hair	Temperature depression after specimen saturation
22	Bentonite	B	Tygon Coil	4.16, 4.17	X-ray	300%	Hair, Lens	

[a]P-T Trajectory Type see Figure 4.3;
[b]Mass ratio between liquid (THF-solution/water) and sediment particles;
[c]The X-ray transparent aluminum chamber that allows 3D CT scan of the specimen;
[d]The visualization chamber with a sapphire window that allows a camera to record the process;
[e]From the bottom to top: kaolinite, sand and kaolinite;
[f]From the bottom to top: kaolinite, sand

Table 4.2 Sediment properties

Soil Description	Minerology	Mean particle size D_{50} [μm]	Specific Surface S_s [m^2/g]	Liquid Limit LL[%]
Silica Flour	SiO_2	20	0.5	31
Kaolinite	$Al_2Si_2O_5(OH)_4$[a]	0.36[b]	34	67
Diatom	92% SiO_2[c]	10[c]	89	121
Bentonite	$Al_2O_34SiO_2H_2O$[a]	0.07[d]	565	276
Hydrophobic Silica	SiO_2 coated with chlorosilanes	≈0.035[e]	32[e]	n/a

[a)]Reade Advanced Materials; [b)](Palomino and Santamarina 2005); [c)]PERMA-GUARD; [d)](Plaschke et al. 2001); [e)]Estimated from SEM Images

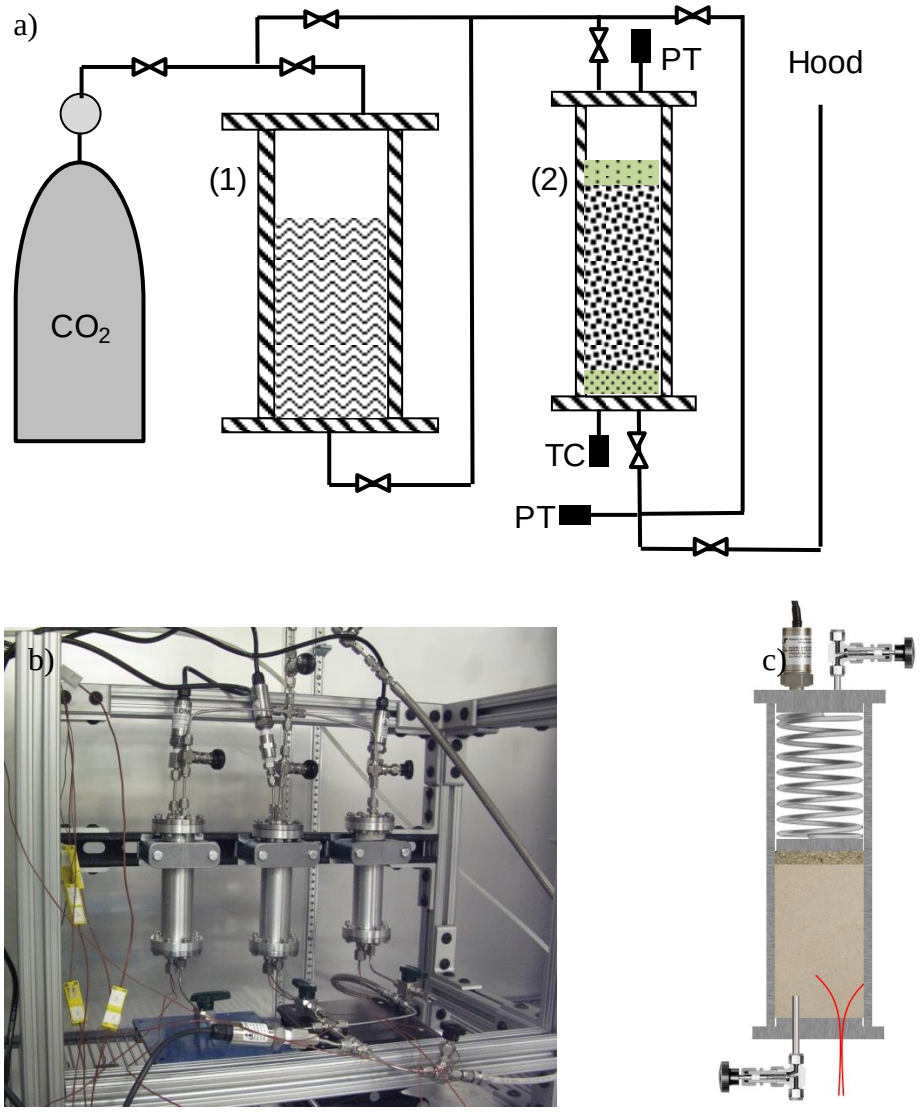

Fig. 4.1. Reactors and PT control. (a) Flow control including (1) Auxiliary chamber and (2) X-ray transparent reactor. (b) X-ray transparent reactors in temperature-controlled environmental chamber. (c) Effective stress controlled reactor.

a) b)

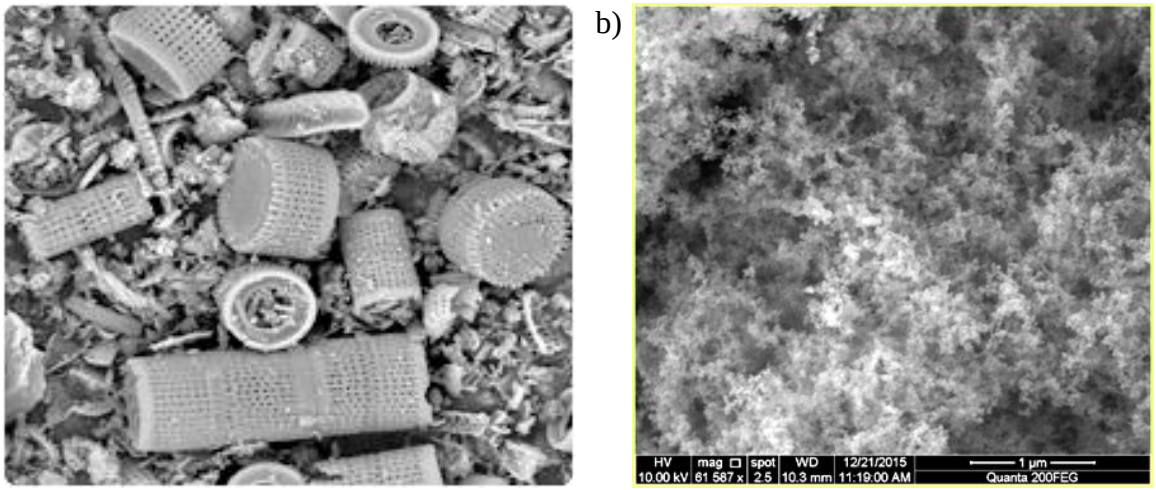

Fig. 4.2. Scanning electron microscopy image of a). Diatomaceous earth (PERMA-GUARD) and b). Fumed hydrophobic silica powder.

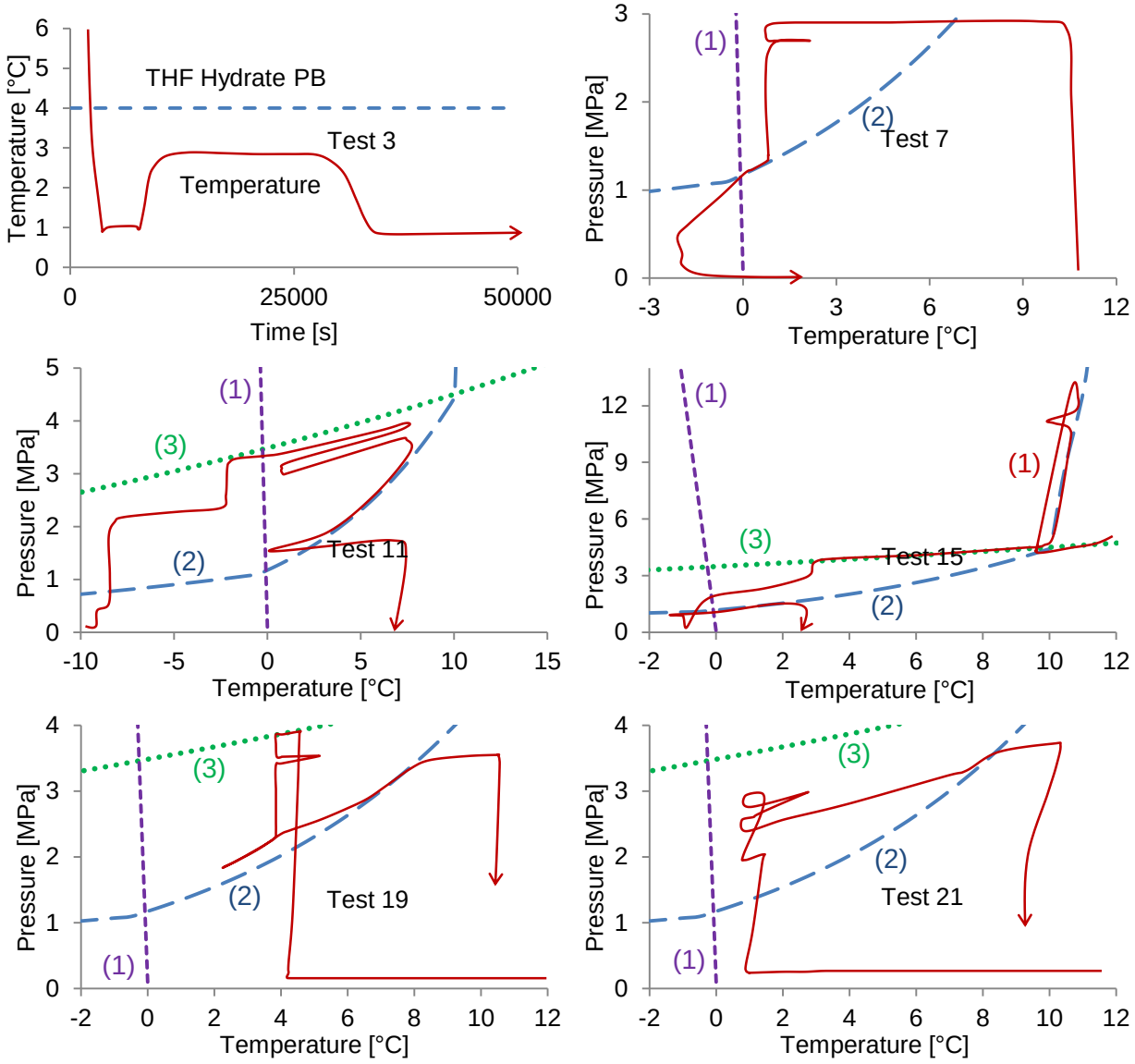

Figure 4.3 Typical P-T Trajectories (red lines) for various tests — Test numbers to Table 4.1. The reference lines correspond to (1) ice-water phase boundary, (2) CO_2 hydrate phase boundary and (3) gas-liquid CO_2 boundary.

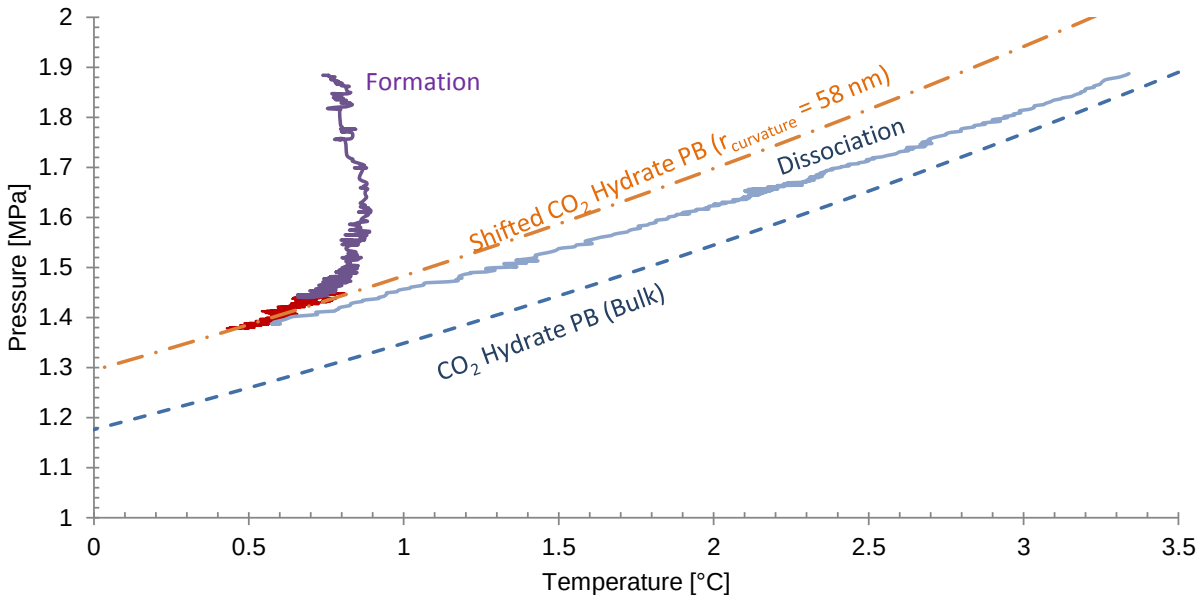

Fig. 4.4. Pore size effect on phase transformation during formation and dissociation (Test 19, Table 4.1). Two phase boundaries are shown for reference: lower boundary corresponds to bulk and the upper boundary corresponds to a spherical curvature with radius $r_{cuvature}$ = 58 nm.

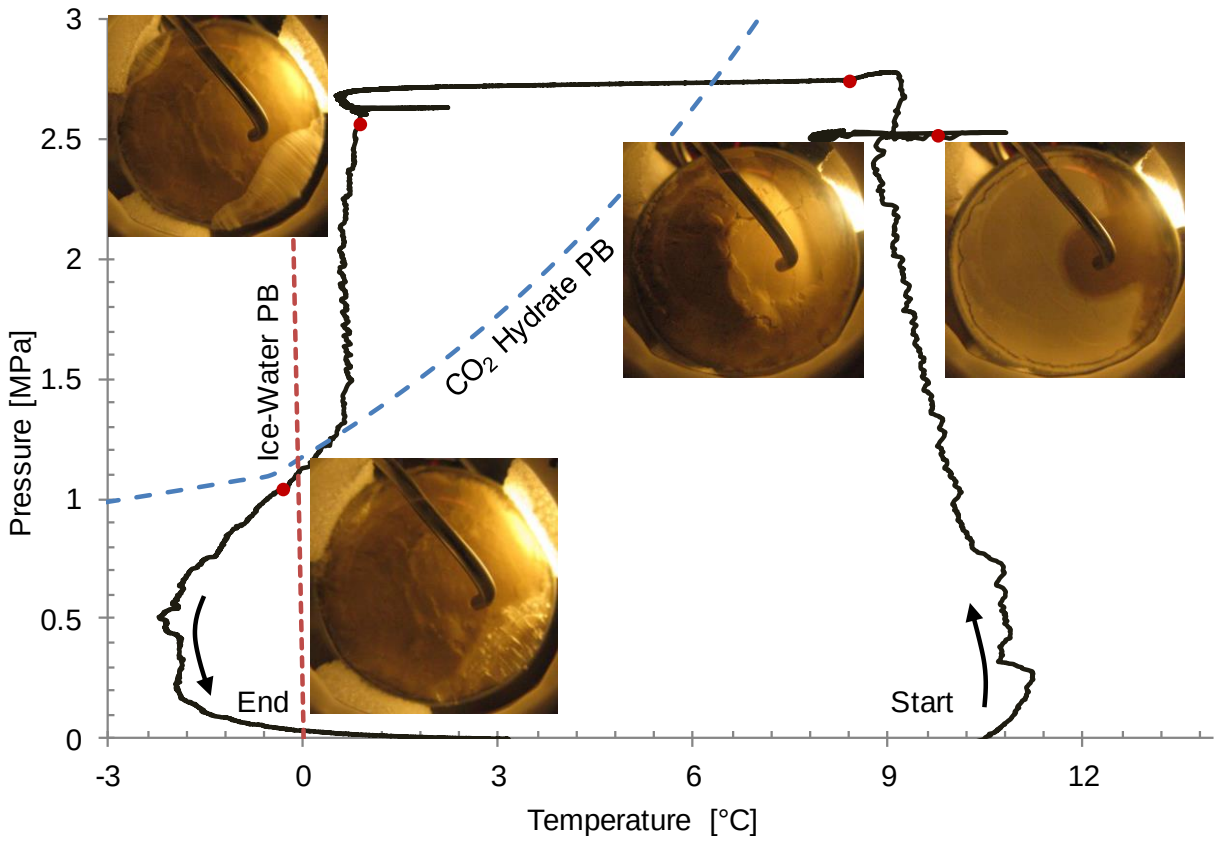

Fig. 4.5. Hydrate formation induced during water injection onto an oven dried diatomaceous earth specimen. Water injection starts outside the stability field at a gas pressure P_{gas} = 2.5 MPa, and T = 10.5 °C. Selected photographs are shown at PT conditions represented by the filled circle (Test 7, Table 4.1).

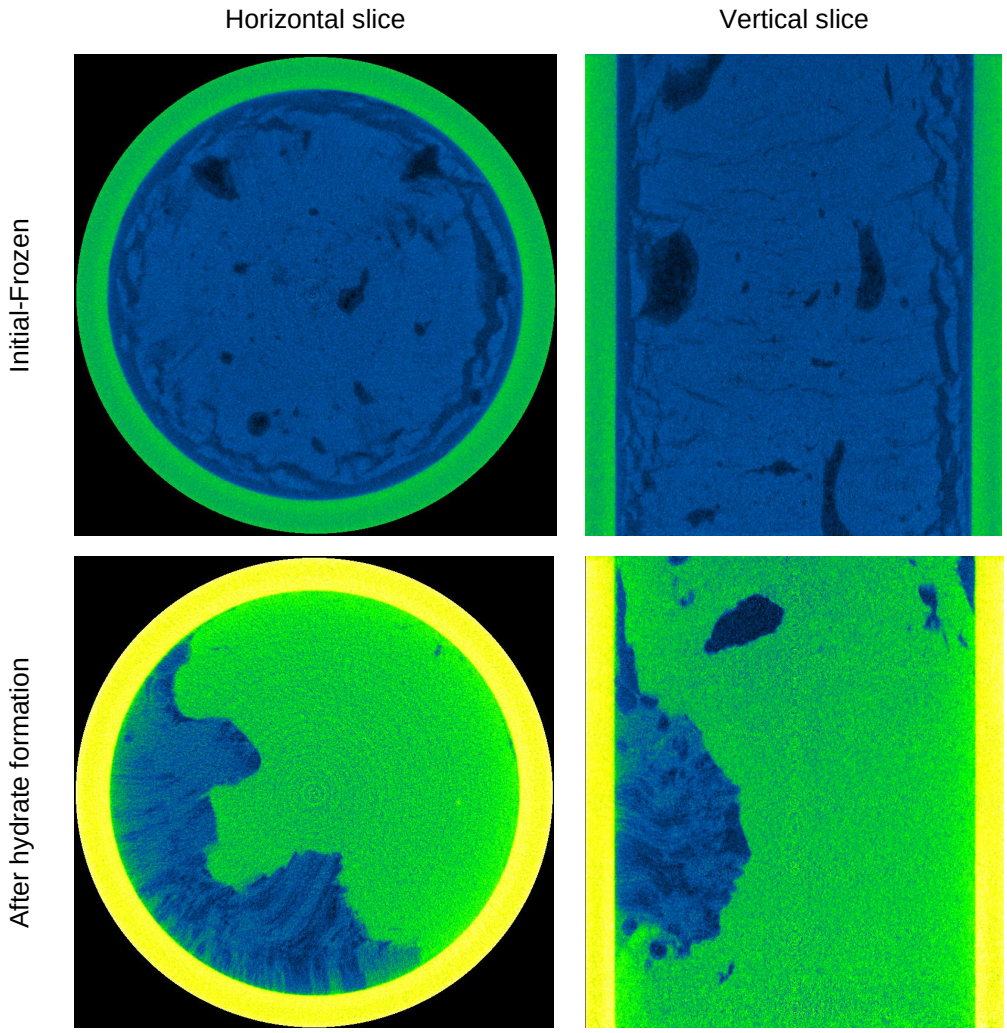

Fig. 4.6. Hydrate morphology: ice-to-hydrate transformation in an unsaturated frozen kaolinite specimen (Test 11, Table 4.11). Darker blue colors in lower images correspond to hydrate. (In collaboration with Seth Mallett).

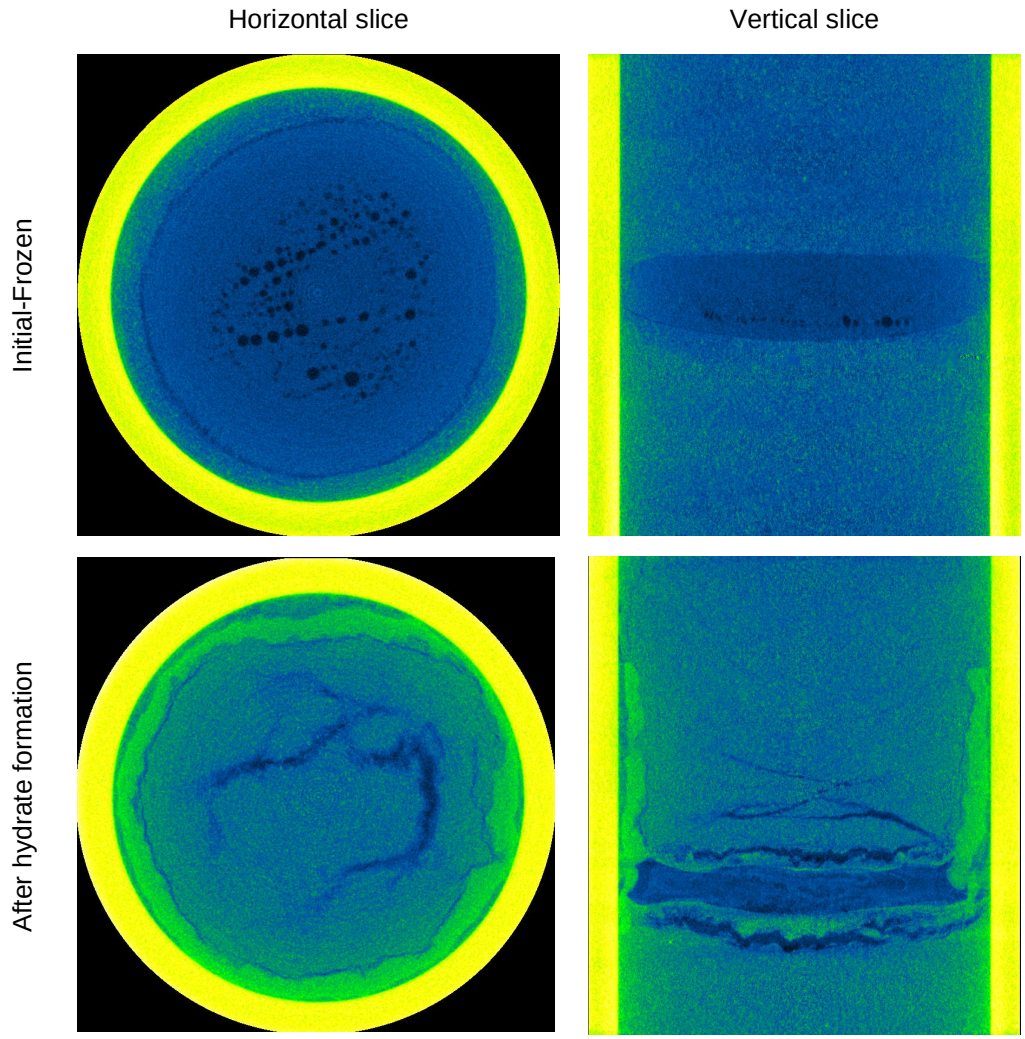

Fig. 4.7. Hydrate morphology: ice-to-hydrate transformation of an ice lens buried in a dry kaolinite specimen (Test 12, Table 4.1). Darker blue colors in lower images correspond to hydrate. (In collaboration with Seth Mallett).

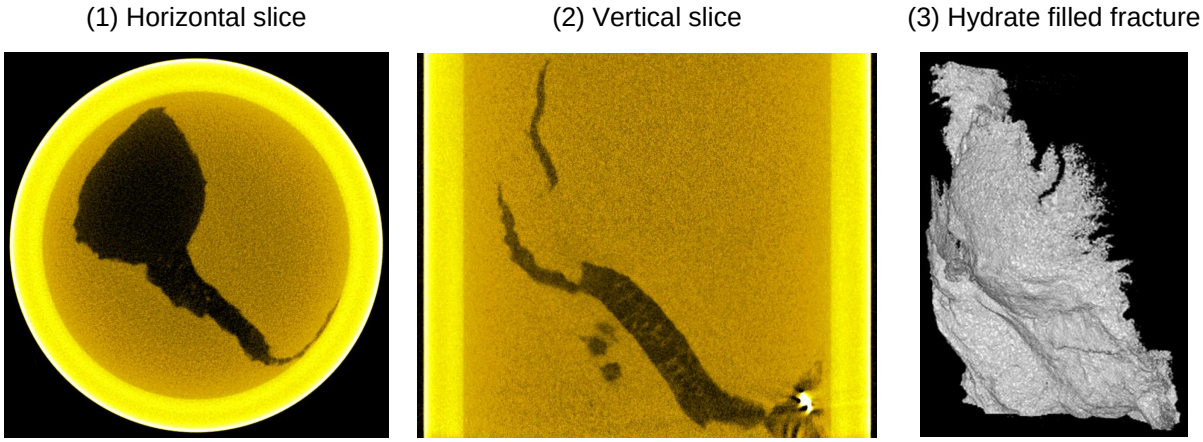

Fig. 4.8. Hydrate morphology: gas driven fracture formed in a water saturated kaolinite specimen (Test 15, Table 4.1). (1) Horizontal slice; (2) Vertical section; (3) 3D hydrate filled fracture extracted from the 3D tomography image.

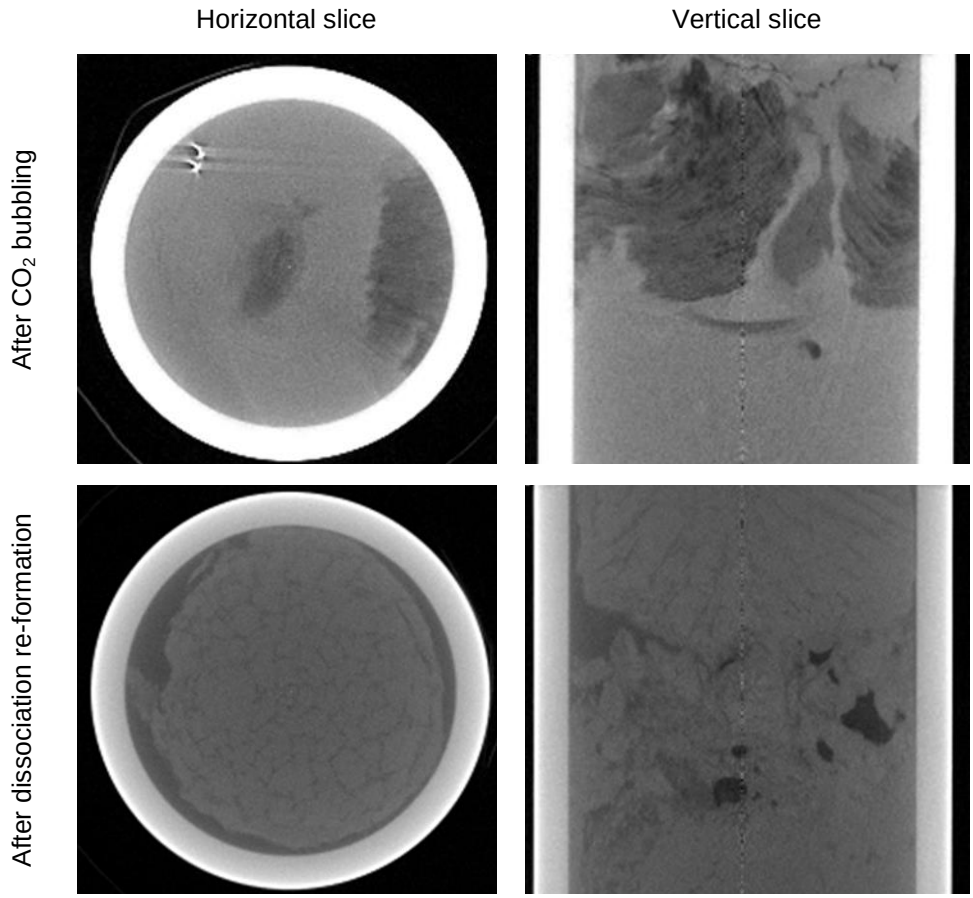

Fig. 4.9. Hydrate morphology: gas bubbles migration in kaolinite slurry (Test 20, Table 4.1).

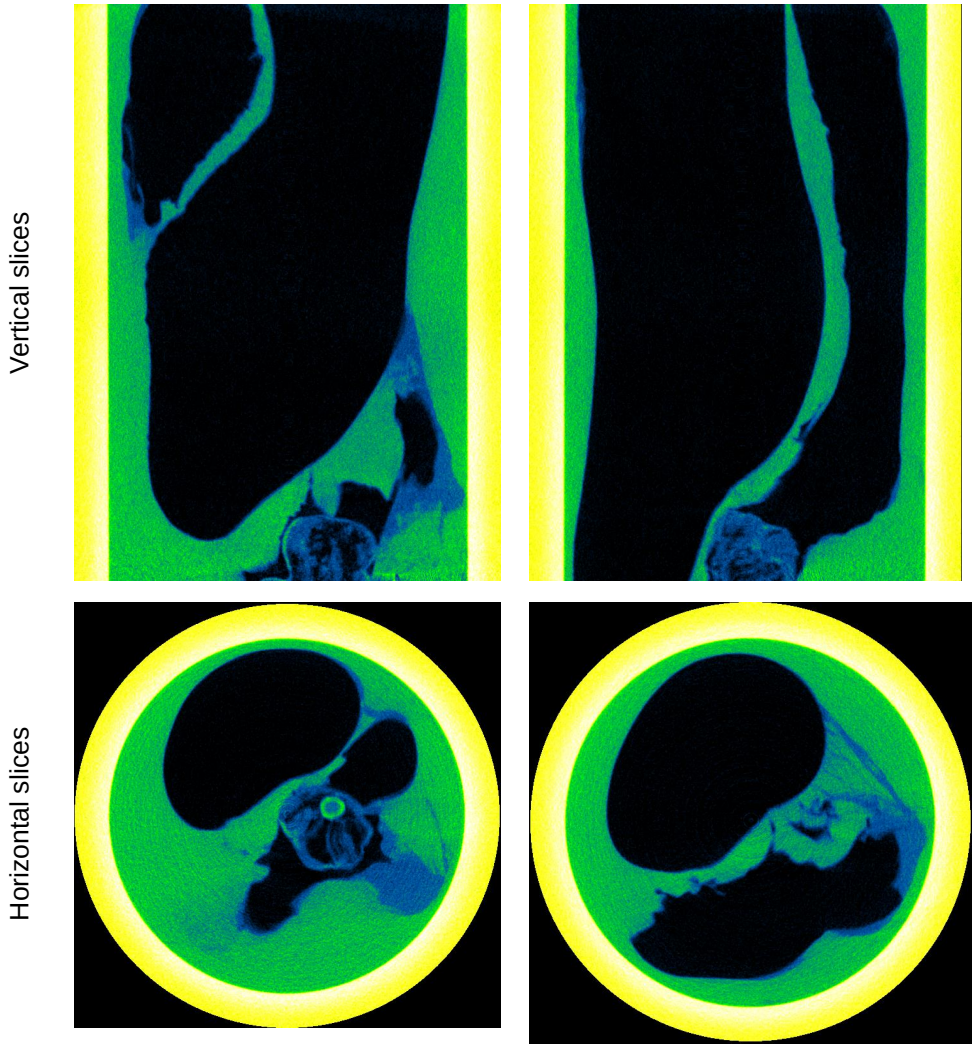

Fig. 4.10. Hydrate morphology: gas injection bubbling through kaolinite slurry specimen (Test 19, Table 4.1). Darker blue colors in lower images correspond to hydrate. (In collaboration with Seth Mallett).

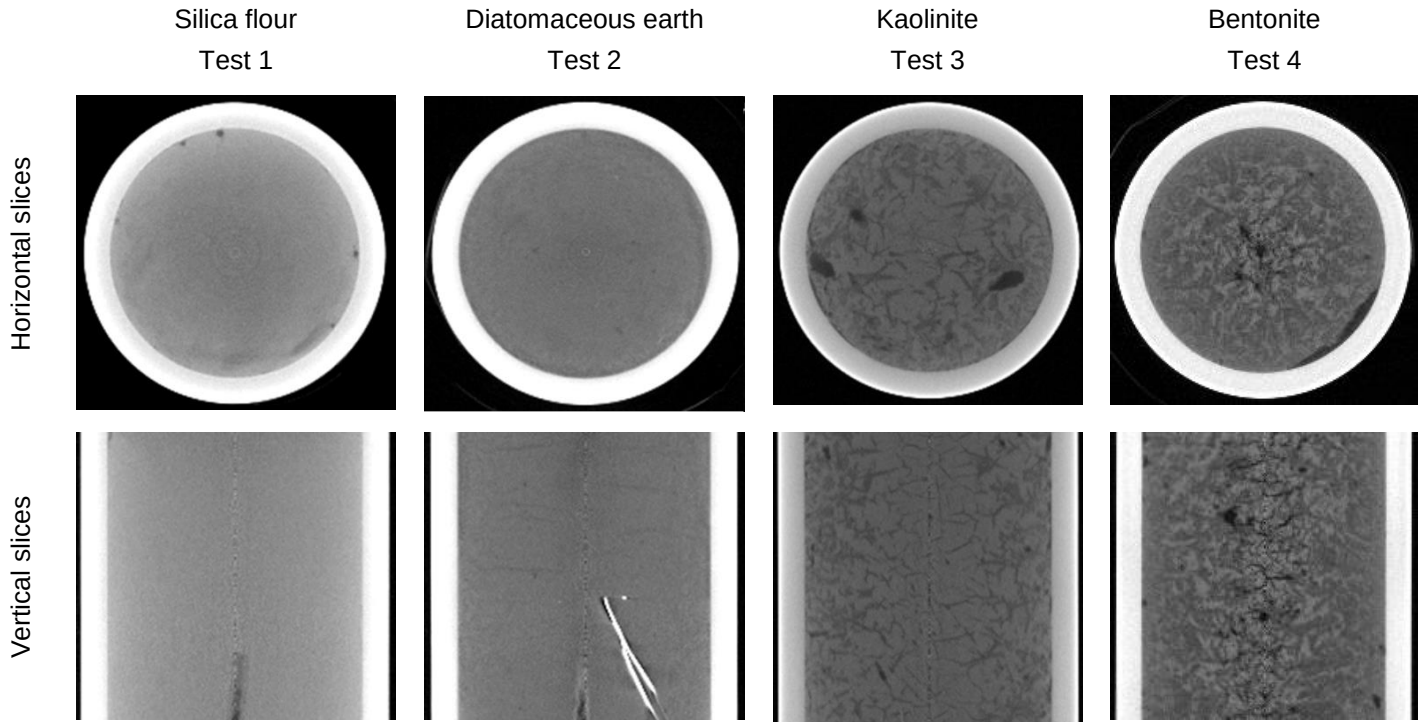

Fig. 4.11. Tetrahydrofuran THF hydrate morphology in different sediments. Note: formed from stoichiometric solution.

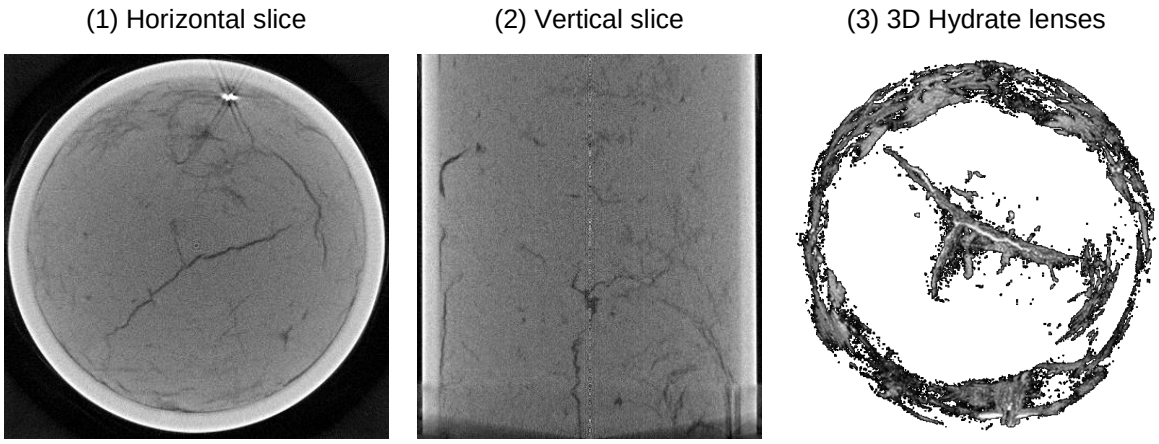

Fig. 4.12. Hydrate morphology: THF hydrate in a diatomaceous earth specimen (Test 5, Table 4.1). (1) Horizontal slice; (2) Vertical slice; (3) Segregated 3D hydrate lense structure. (In collaboration with Seth Mallett).

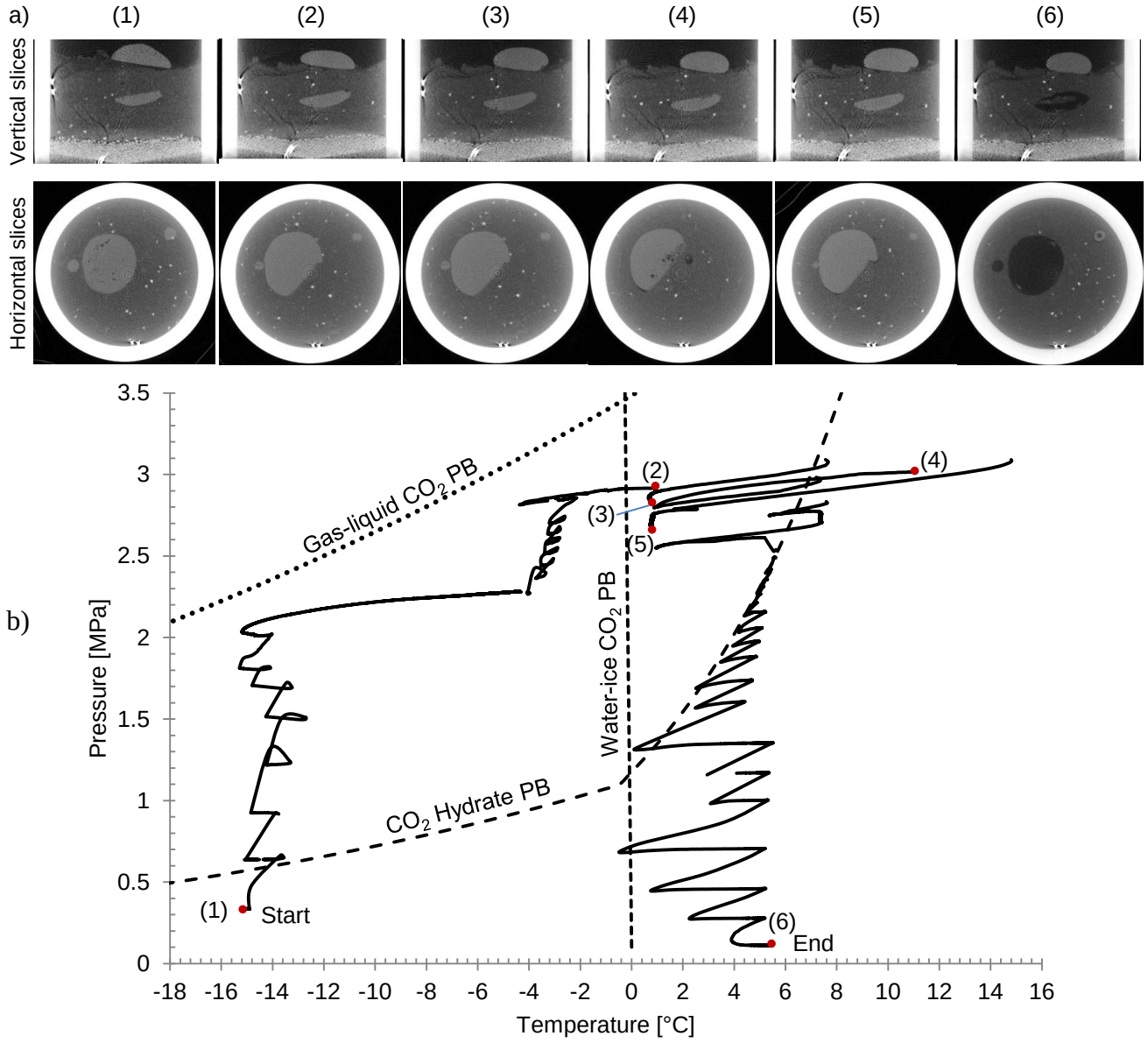

Fig. 4.13. Ice-to-hydrate transformation of two ice lenses buried in hydrophobic fumed silica (Test 14, Table 4.1). The numbers and large red dots in the pressure-temperature space display experimental conditions during the corresponding scans. a). Sequence of CT slices; b). T-P path in the experiment.

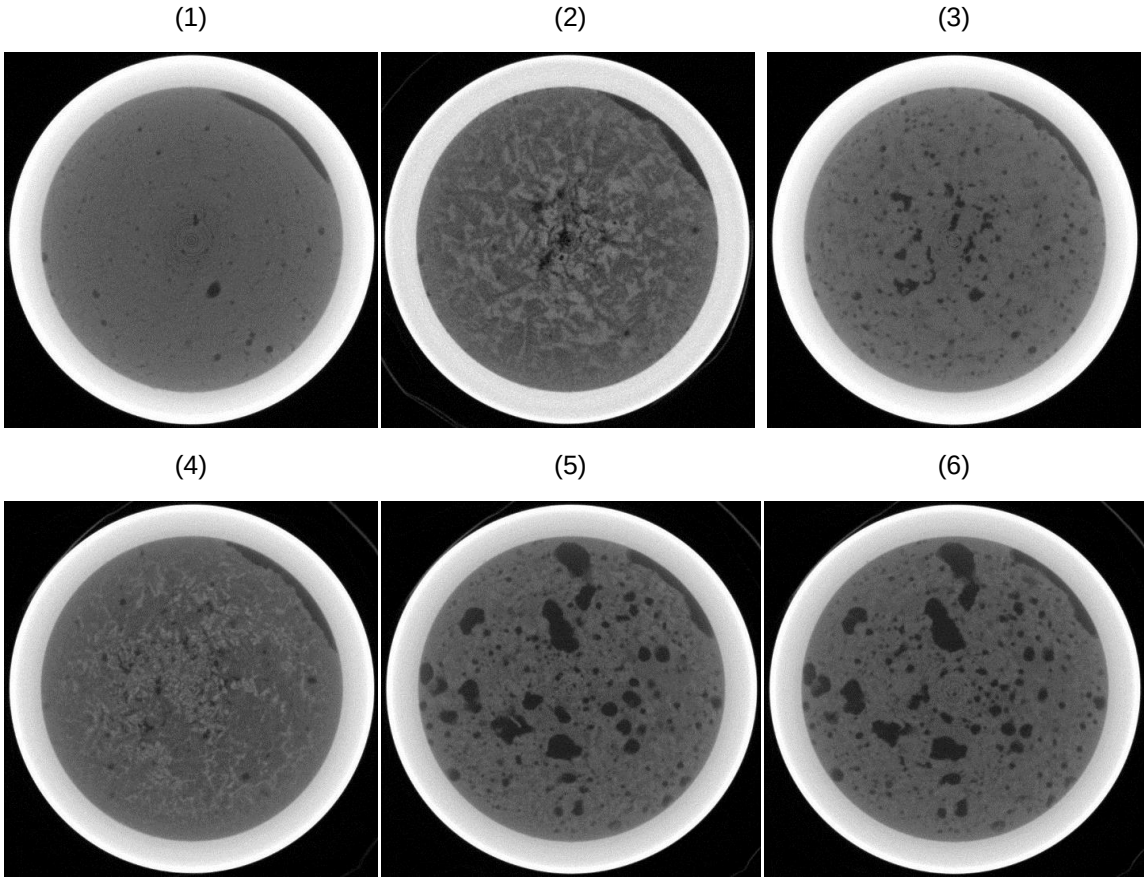

Fig. 4.14. THF hydrate formation and dissociation in a bentonite specimen (Test 4, Table 4.1). (1) Initial condition; (2) Hydrate formation at 1°C; (3) One day after dissociation; (4) Hydrate formation at -18°C; (5) One hour after dissociation; (6) One day after dissociation.

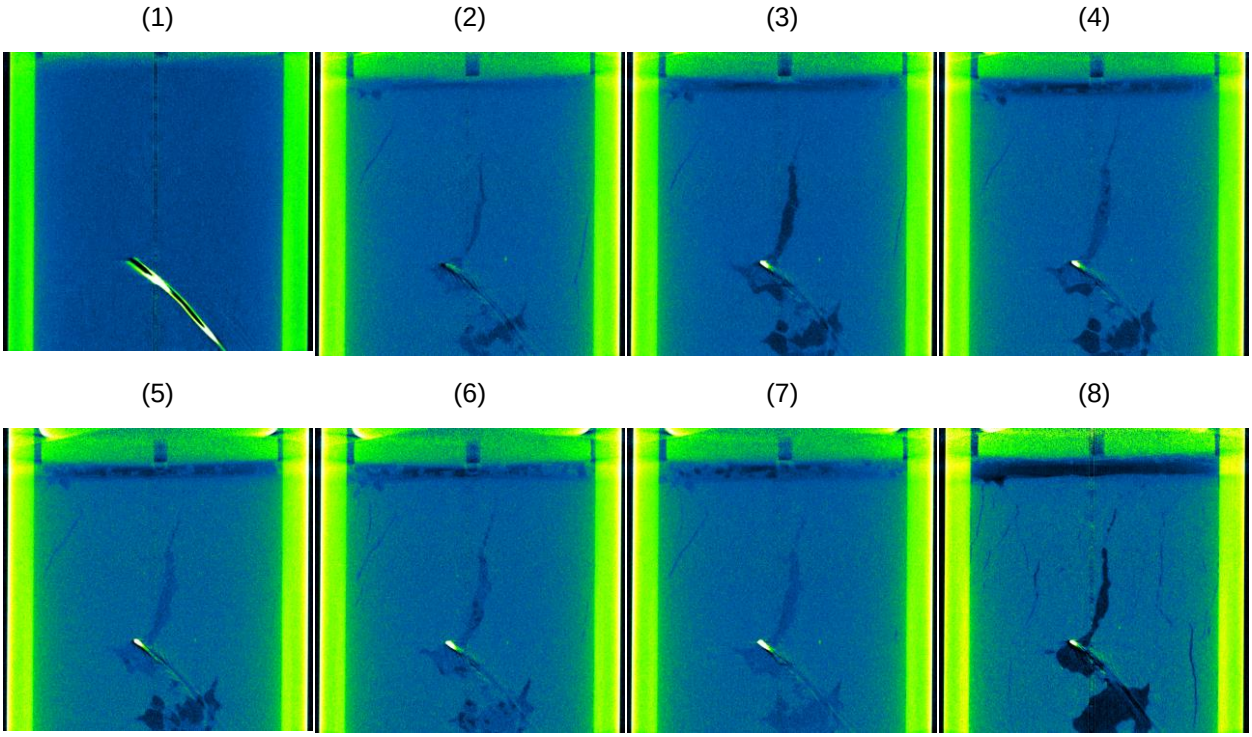

Fig. 4.15. Hydrate lens evolution after the generation of a gas-driven fracture in a water saturated kaolinite specimen (Test 17, Table 4.1). (1) Initial condition; (2) 24 hours after gas injection; (3) 48 hours; (4) 72 hours; (5) 96 hours; (6) Liquid CO_2 release; (7) Gas hydrate dissociation completion; (8) Final state at atmosphere pressure.

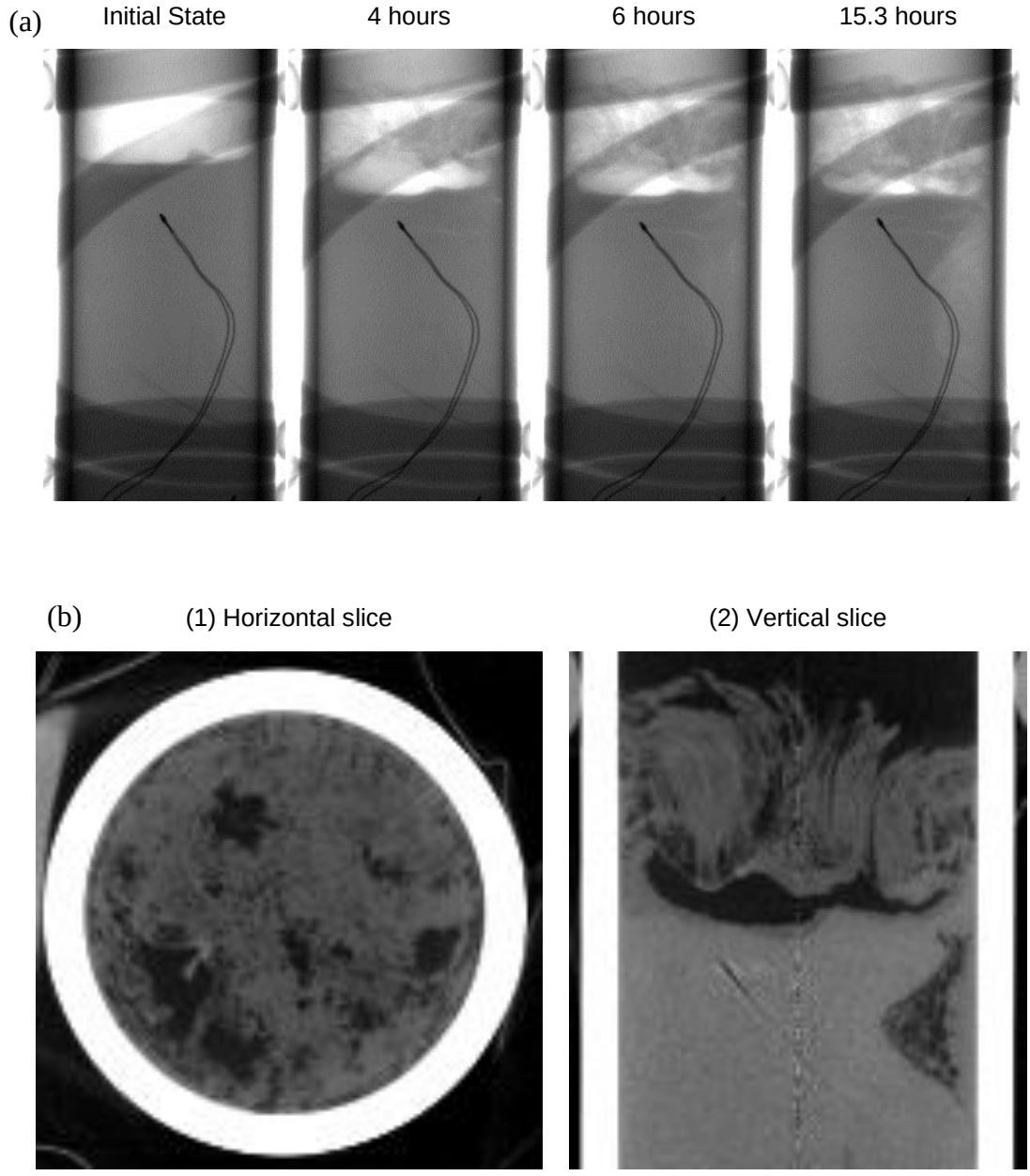

Fig. 4.16. CO_2 hydrate formation at the top of and inside a kaolinite paste (Test 22, Table 4.1). The paste is exposed to CO_2 gas at 3.4 MPa for 20 days with subsequent temperature decrease to stability field. (a) Evolution in time; (b) Horizontal and vertical slices of the CT after 8 hours.

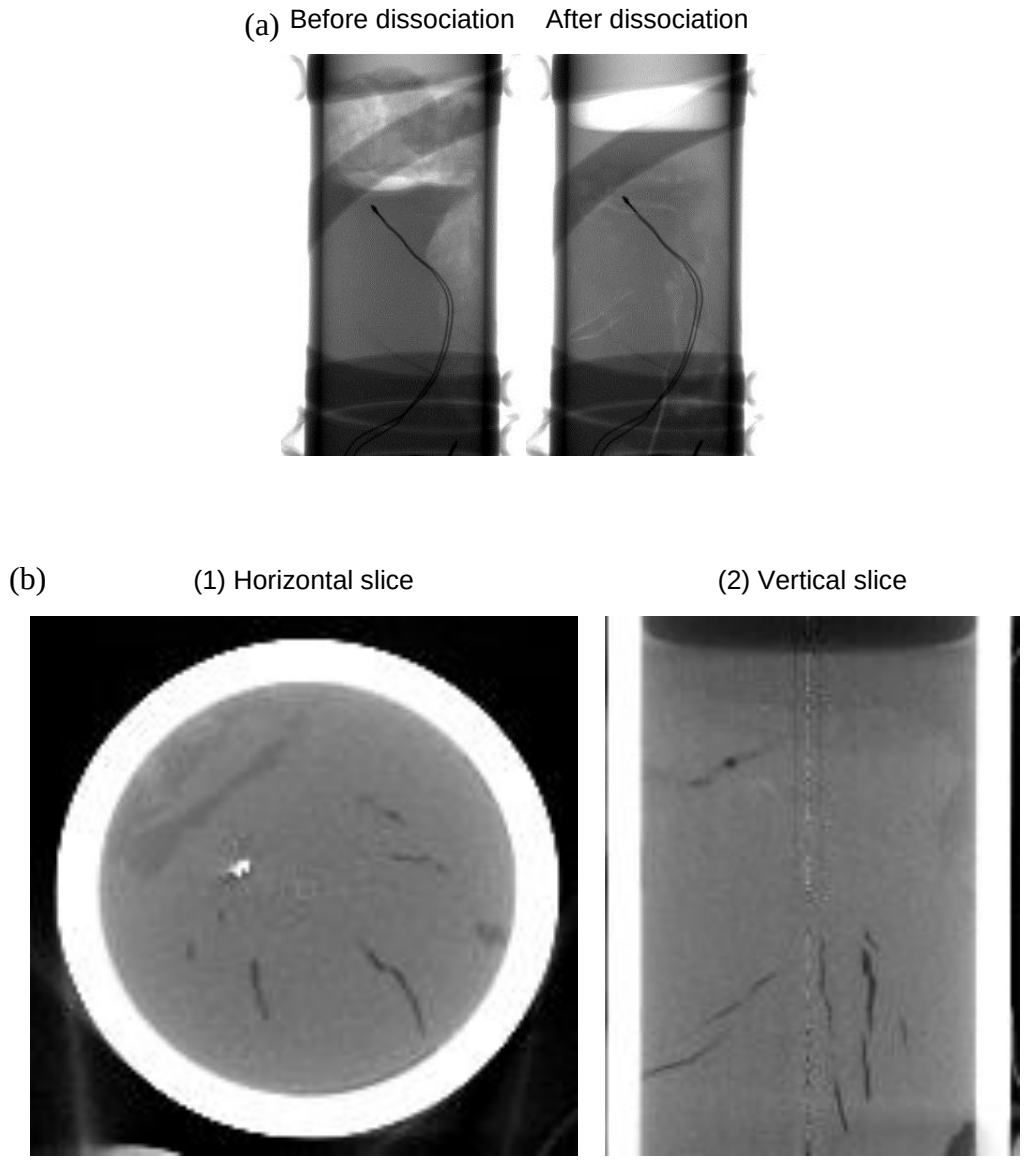

Fig. 4.17. Hydrate dissociation developed by depressurization. (a) Projections; (b) Horizontal and vertical slices of CT gathered after dissociation.

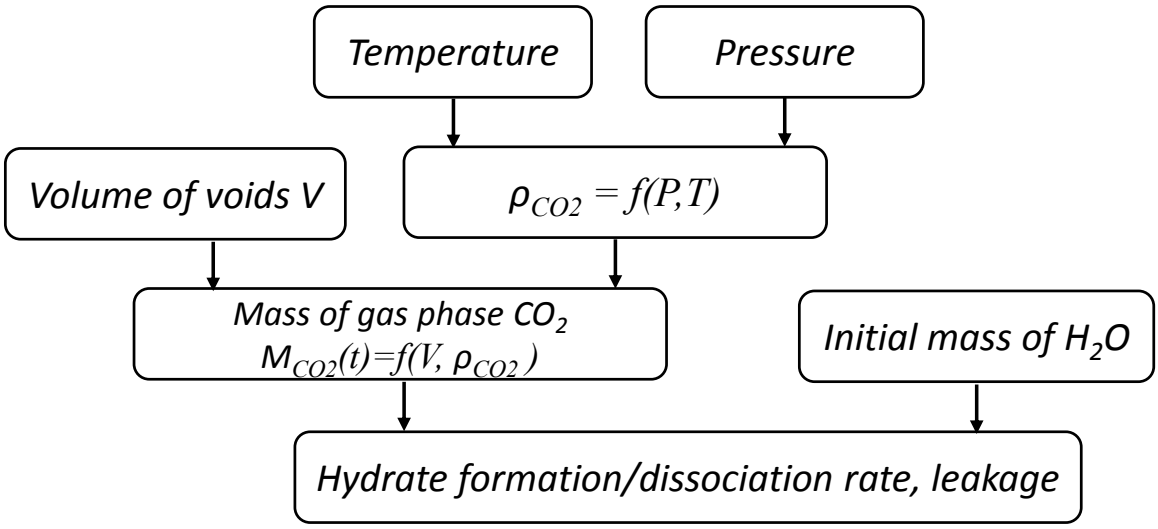

Fig. 4.18. Mass balance analysis.

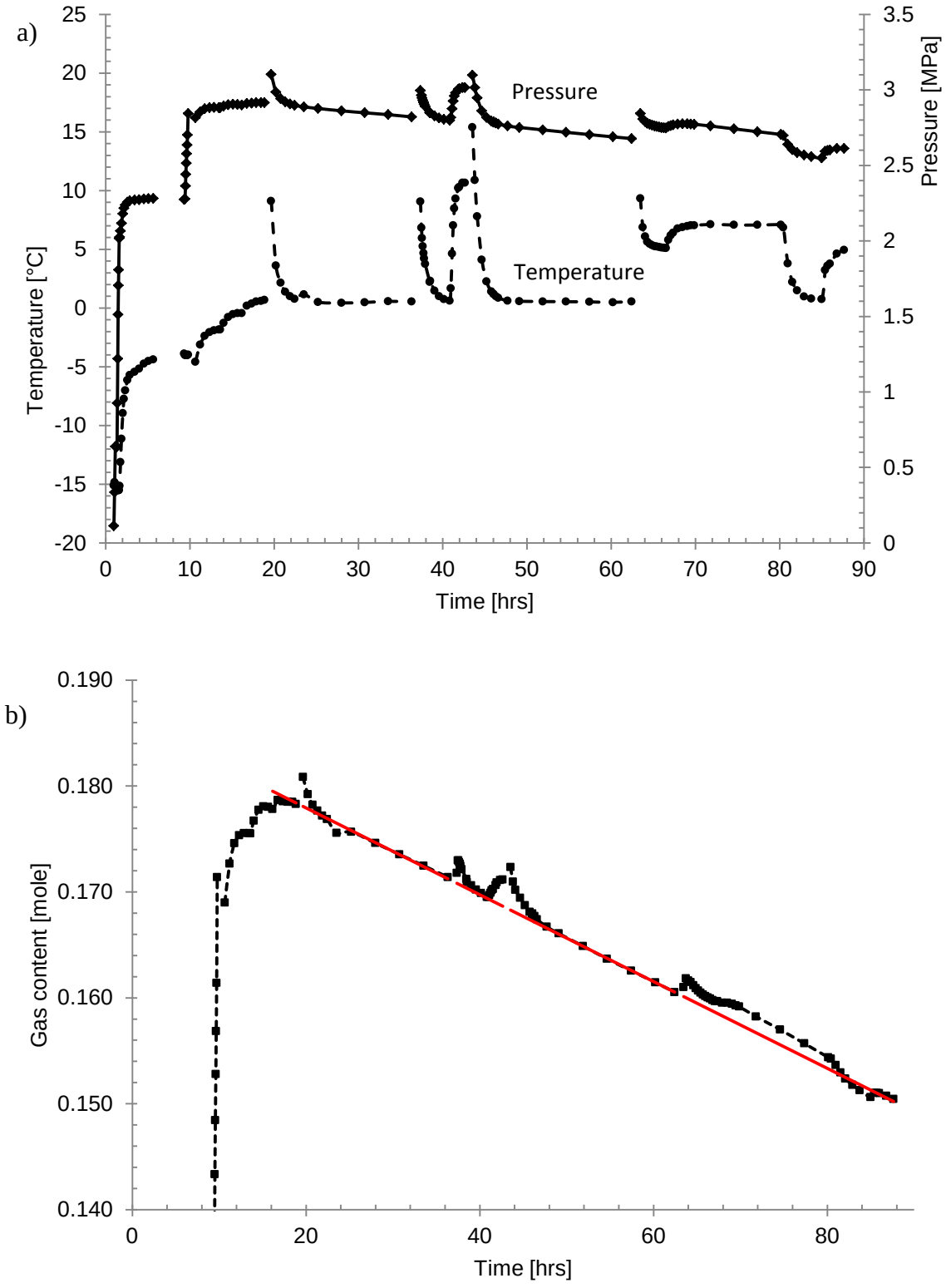

Fig. 4.19. Analysis of gas consumption during hydrate formation. a). Temperature and pressure versus time; b). Calculated gas content versus time.

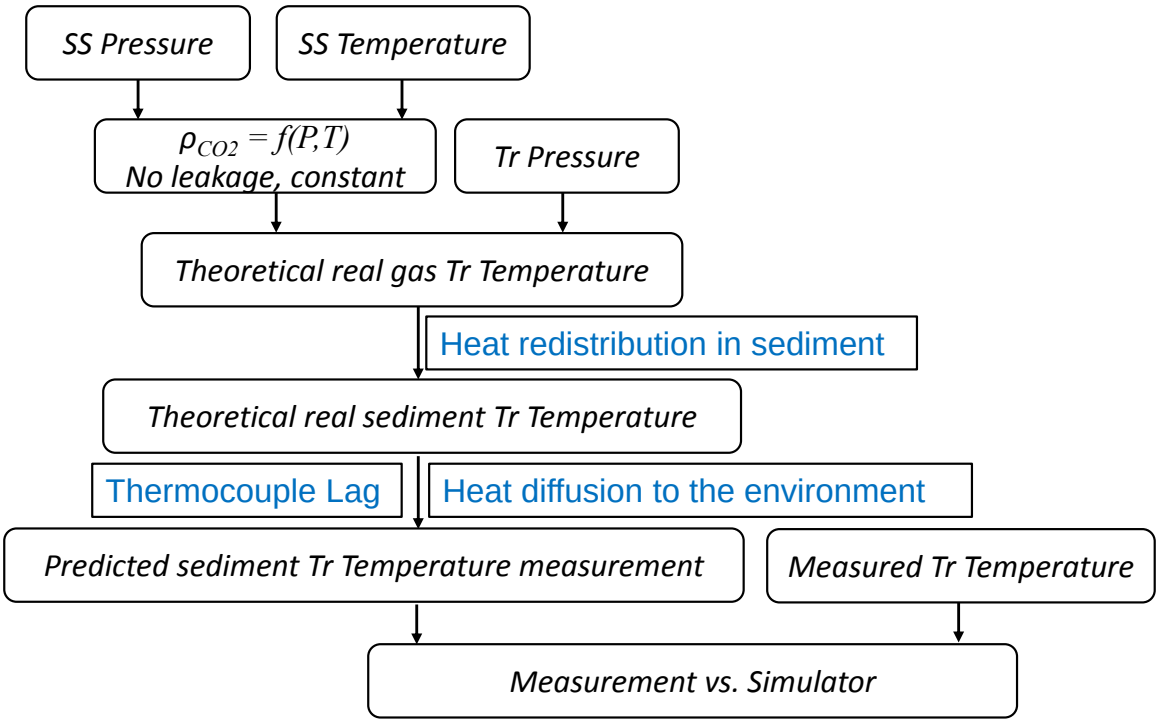

Fig. 4.20. Thermal analysis.

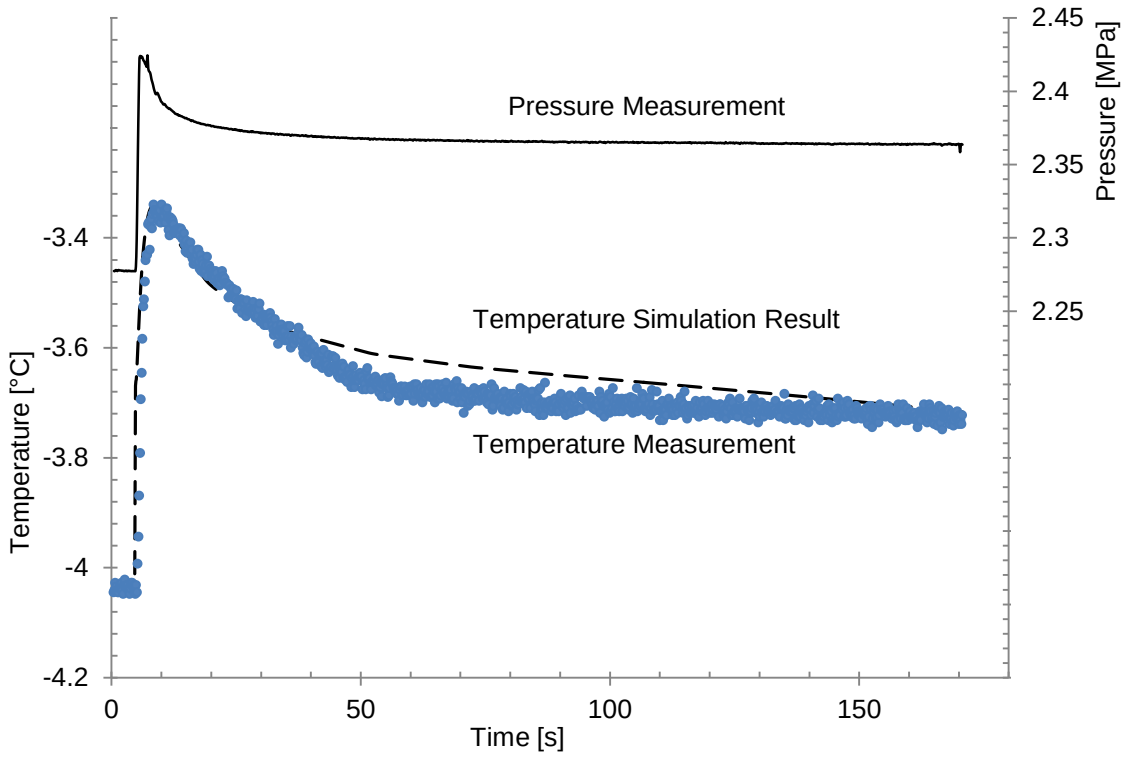

Fig. 4.21. Thermal response: simulation result versus measurement.

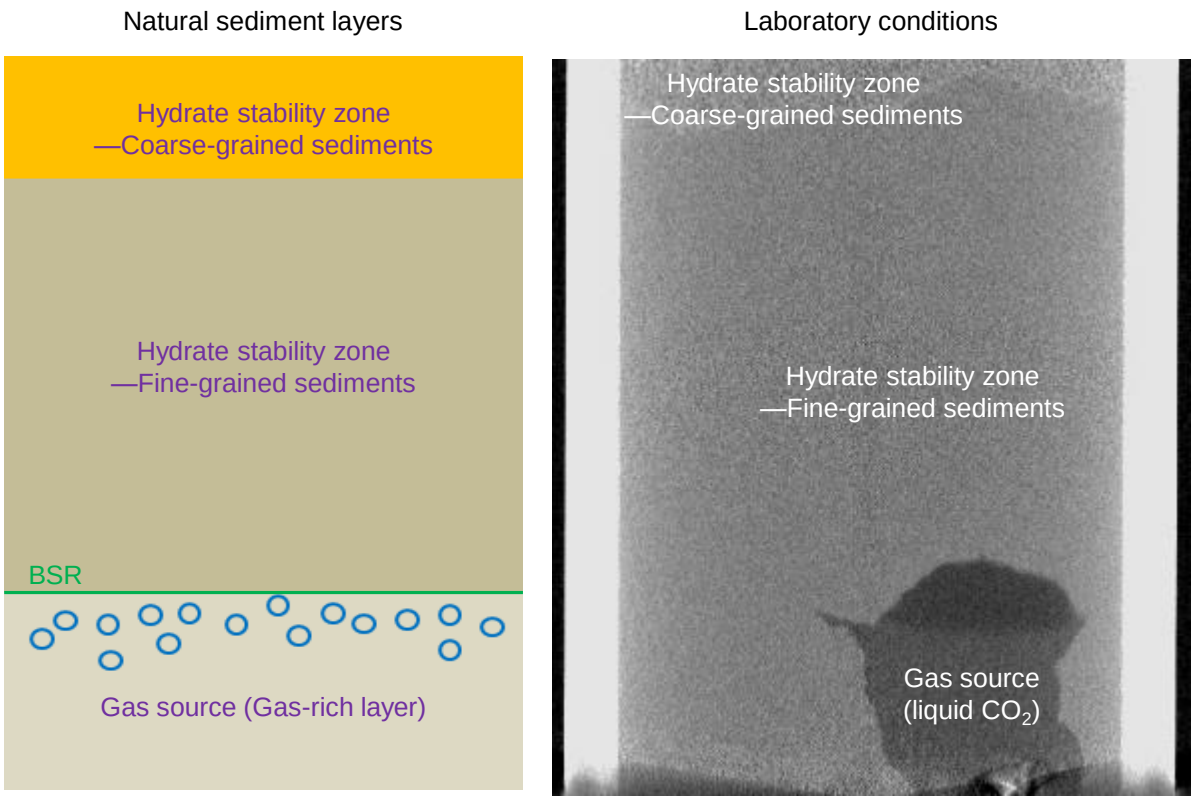

Fig. 4.22. Emulation of natural hydrate formation conditions in the laboratory.

CHAPTER 5

PHYSICAL PROPERTIES OF HYDRATE BEARING FINE-GRAINED SEDIMENTS

5.1 Introduction

Gas hydrates in marine and permafrost sediments are potential energy resources (Boswell 2009; Collett 2002). The dissociation of gas hydrates can contribute towards climate change (Archer 2007; Ruppel and Pohlman 2008), cause ground subsidence and trigger seafloor landslides (Grozic 2010; Hornbach et al. 2007; Kvalstad et al. 2005).

Hydrate in coarse-grained sediments exhibits cementing, pore-filling, and grain-coating morphology (Dai et al. 2012). However, hydrate forms into segregated lenses, veins and nodules in fine-grained sediments (Chapters 3 and 4).

The physical properties of hydrate-bearing fine-grained sediments depend on the properties of each component in the system and the morphology of the segregated hydrate mass. In particular, the water migration and sediment compaction induced by cryogenic suction and particle-displacive hydrate formation changes the physical properties of the sediments around hydrate lenses.

The characterization of the physical properties of hydrate-bearing sediments is critical to both engineering and research. The thermal and hydraulic conductivities of hydrate-bearing sediments control hydrate dissociation and gas production. On the other hand, the mechanical properties before and after dissociation define the mechanical stability and deformation field during hydrate dissociation and gas production.

Characterization difficulties limit our ability to determine a reliable set of physical properties for hydrate-bearing fine-grained sediments. Pressure cores are expensive, and mechanical sampling disturbance are inherent to all coring including pressure cores. In-situ measurements assess a small area around the measuring device, which is extensively disturbed by the insertion of the device itself. And, laboratory hydrate formation in fine-

grained sediments is most challenging and may not produce specimens that resemble natural hydrate-bearing sediments (Chapters 3 and 4).

This chapter uses effective media models and numerical simulations to estimate the physical properties of hydrate-bearing fine-grained sediments. Clearly, particle-displacive hydrate morphology in fine-grained sediments requires distinct physical models compared to the pore-filling hydrate in coarse-grained sediments. We start with a discussion on the hydrate distribution in fine-grained sediments and the changes in the surrounding sediment properties during hydrate formation. Then we explore thermal and hydraulic conductivities, stiffness and strength properties of hydrate-bearing sediments. The final section addresses effective media models and bounds.

5.2 Hydrate Distribution and Cryogenic Suction

5.2.1 Hydrate distribution

Figure 5.1 presents a collection of X-ray projections and CT slices of sediments recovered using pressure core technology. The bright areas correspond to the low-density hydrate mass. Photographic images of the sediments after rapid depressurization compiled in Figure 5.2 provide complementary information on the hydrate morphology and on the hydrate-sediment interface. Clearly, the hydrate-sediment interface is not smooth; in fact, the shape of the hydrate mass is quite irregular and jagged.

Hydrate formation from dissolved methane in fine-grained sediments is a diffusion-limited reaction process. Images in Figure 5.2 exhibit Liesegang band topology (Chapter 3). Alternatively, hydrate forms in gas-driven fractures and inherits the fracture topology, including its rough edges and uneven propagation fronts (Figure 5.3); these features can explain morphological characteristics observed in Figure 5.1 and 5.2. Conceptual hydrate distributions in Figure 5.4 attempt to capture salient geometric characteristics observed in Figures 5.1, 5.2 and 5.3.

Hydrate saturation in fine-grained sediments. The hydrate saturation is defined as the ratio between the hydrate volume and the overall pore space. However, this definition is

inadequate for particle-displacive hydrate distributions. Instead, we define the hydrate volume fraction VF_h, as the ratio between the volume of hydrate and the total sediment volume.

5.2.2 Cryogenic suction: Overconsolidation

Hydrate formation extracts water from the sediments and causes it to compact or consolidate. Figure 5.5a and 5.5b demonstrates the consolidation effect of cryogenic suction on a kaolinite specimen subject to a freezing front imposed on the upper boundary; the X-ray attenuation coefficient in the sediments is higher near the ice front (top) than in the far field of the cold front (bottom). Figure 5.5c illustrates mechanism of cryogenic suction at the particle-scale. The pressure of the hydrate mass equilibrates the sum of the pore water pressure and the effective stress. Therefore, the effective stress equals the capillary pressure between the hydrate mass and the pore water.

Cryogenic suction, water migration and ion exclusion during hydrate formation alter the physical properties of the sediment that surround the segregated hydrate. Therefore, it is not appropriate to use the properties of the normally consolidated sediments NCS in a two-component effective medium model: in fact, the stiffness, strength, and thermal conductivity of the sediments after hydrate formation is higher than for the normally consolidated sediments at the same burial depth or effective stress; on the other hand, the sediment hydraulic conductivity decreases with the reduction in void ratio. The electrical conductivity response of the sediment that surrounds the hydrate mass is complex and varies in time: it decreases with the reduction in porosity, but it increases due to ion-exclusion; however, excess ions eventually diffuse away.

Over-consolidation ratio OCR. The OCR is defined as the ratio between the effective stress and the effective stress at the corresponding burial depth. The effective stress σ'_{cs} around particle-displacive hydrate can be estimated from Equation 3.30,

$$\sigma' = \frac{\Delta T'}{T_B} H_f \rho_h \tag{5.1}$$

where $\Delta T'$ represents the temperature depression; T_B is the temperature at the bulk hydrate phase boundary; H_f is the bulk enthalpy of fusion; and ρ_h is the hydrate density. Note that the analysis assumes sufficient gas supply in the sediment. One degree of super-cooling approximately corresponds to 1.57 MPa (T_B = 273K, H_f = 0.46kJ/g, ρ_h = 0.937 g/cm^3). Therefore, even a slight degree of super-cooling could result in a dramatic effective stress change.

Let's assume that the behavior of the fine-grained sediments follows a Terzaghi consolidation model. The relationship between the void ratio e and the isotropic stress σ'_{cs} is

$$e = e_0 - C_c \ln\left(\frac{\sigma'_{cs}}{\sigma'_0}\right) \tag{5.2}$$

where e_0 and σ'_0 are the initial void ratio and effective stress and C_c is the compression index. Sediments around the hydrate mass obey mass conservation when hydrate formation does not involve water transport from the far field. Assuming negligible changes in mass densities, the volume of hydrate is equal to the sediment compaction

$$VF_h = \frac{\Delta e}{1+e_0} = \frac{1}{1+e_0} C_c \ln(OCR) \tag{5.3}$$

Given an observed hydrate volume fraction VF_h, initial effective stress at the burial depth σ'_0, and sediment parameters e_{1kPa} and C_c so that $e_0 = e_{1kPa} - C_c \log(\sigma'_0/kPa)$, then effective stress acting on the sediment around the hydrate mass is

$$\sigma'_{cs} = \sigma'_0 \exp\left[\frac{(1+e)VF_h}{C_c}\right] \tag{5.4}$$

This effective stress is used to compute all physical properties for sediments around lenses.

5.3 Numerical Simulations

Numerical simulations are conducted next to estimate the physical properties of fine-grained hydrate-bearing sediments.

5.3.1 Conduction properties: Laplacian fields

This section addresses all the physical properties governed by a single potential field (Berryman 1995). Let Ψ denote the generalized potential. The generalized flow q, along the i direction is,

$$q_i = K_i(x) A \frac{\partial \Psi}{\partial x_i} \tag{5.5}$$

where K is the conductivity, A is the section area, and x is the coordinate along the i^{th} direction. For example, the hydraulic head directs the hydraulic flow and the temperature gradient drives the heat flux. Then the mass/energy/electron conservation rules mandate that the flow in equals the flow out. Consequently, the Laplace equation describes the generalized conduction in a 3D space,

$$\sum_{i=1}^{3} K_i(x) \frac{\partial^2 \Psi}{\partial^2 x_i} = 0 \tag{5.6}$$

This single Laplace equation enables multi-physics analyses with one formula.

The majority of the physical properties of methane hydrate are similar to ice. However, the thermal conductivity is an exception to this rule: while ice has higher thermal conductivity than water, the thermal conductivity of hydrate is ~30% lower than that of water (Rosenbaum et al. 2007; Warzinski et al. 2008).

Figure 5.6 demonstrates the influence of two types of segregated hydrate distribution on the thermal conduction of hydrate-bearing sediments. Gas hydrate has significantly lower thermal conductivity in comparison to the sediments (Table 5.1a). Therefore, the heat flow line in Figure 5.6 shifts to reduce the length of the conduction path through the hydrate.

Figure 5.7 compiles the simulation results of the thermal conductivities K_T as a function of hydrate mass orientation θ. The effective thermal conductivity of the sediments with a single ellipse lens follows the equation below (In collaboration with Seth Mallett),

$$K_T = K_0 \cdot \cos^2\theta + K_{90} \cdot \sin^2\theta \tag{5.7}$$

where K_T is the effective thermal conductivity, K_0 and K_{90} are the effective thermal conductivities when the lens is perpendicular and parallel to the thermal gradient respectively, and θ is the orientation of the hydrate mass. By contrast, the effective thermal conductivity of the sediments that contain crossed hydrate lenses is not sensitive to the lens orientation.

Results for thermal conductivity apply to electrical conductivity, magnetic permeability, and dielectric permittivity as well. The effect of hydrate lenses on effective media properties reflects the corresponding physical properties. For example, the hydraulic and electrical conductivities of hydrate approach zero. Therefore, the cutoff effect of hydrate on the water flow and electric current is more significant than the effect on heat flow.

5.3.2 Mechanical properties: equilibrium and compatibility

Mechanical properties reflect internal equilibrium and compatibility of deformations. The selected stiffness and strength parameters for the various components are summarized in Table 5.1.

Small strain

This section analyzes the bulk modulus B due to its importance in wave propagation. It is common to use wave velocity profiles to estimate hydrate saturation rate (Chand et al. 2004; Ghosh et al. 2010; Lee and Collett 2005; Waite et al. 2009). We use COMSOL to study the elastic properties of hydrate-bearing fine-grained sediments. The effective bulk modulus is the volume average of all the components in the effective medium,

$$B^* = \frac{\Delta P}{\Delta \varepsilon_{vol}} \tag{5.8}$$

where P is the isotropic pressure, and ε_{vol} is the volumetric strain. The bulk modulus increases with the hydrate saturation.

Figure 5.8 presents the negligible influence of hydrate mass orientation θ on the the bulk modulus of hydrate-bearing fine-grained sediments. This is primarily due to the inherent isotropic stress boundary condition associated with bulk modulus. The influences of the hydrate fraction and the type of geometrical distribution are much more significant.

Large strain

The strength analyses include two conditions, non-slip contact and frictional contact between hydrate lens and the sediments. The hydrate lens elements share the same nodes with the soil elements in non-slip contact simulations. This corresponds to when the hydrate is in growing or is stable. Interfaces between the hydrates and the sediments are rough and jagged (See section 5.2). Therefore, there is unlikely to be slippage between the hydrates and sediment in the loading process. However, when the hydrate dissociates during gas production, the dissociation firstly occurs on the interface. Consequently, the contact between hydrates and sediments becomes slippery due to the presence of produced gasses. The characterization of the strength of the sediments then uses frictional contacts. The simulation uses a thin layer of material with a low friction angle (φ = 5°) to represent the frictional contact.

Figure 5.9 presents the displacement and in-plane shear stress field of the hydrate-bearing fine-grained sediments. The localized in-plane shear stress induces the later development of shear bands. When the interface is non-slip, the hydrate mass enhances the sediment strength by the inhibition of shear band formation. Therefore, two shear bands form around but do not cross the hydrate lens. However, when there is a frictional interface, one shear band develops along the interface. The shear band forms at a much lower vertical strain level in frictional conditions compared to the non-slip case.

Figure 5.10 shows the simulation results of sediments that contain cross hydrate lenses. The hydrate lenses behave as reinforcements to the sediment. When the load

transfers directly through the hydrate lenses (0°), the overall sediment strength reaches its peak. The influence of the interface strength is negligible in this condition. However, a slight tilt of the hydrate lenses can result in a significant strength decrease. The shear resistance of the overall sediment controls the load capacity, and the interface strength becomes critical as the angle of orientation θ increases. Shear stress localizes at the intersection of hydrate lenses in the slip interface condition. The hydrate yields and breaks when the shear force exceeds its strength. This could be an important failure mechanism when gas hydrate dissociates.

Figure 5.11 summarizes the shear strength simulation results. The total strength of the sediments reaches the peak when the lenses direction is parallel or perpendicular to the load direction. This strength decreases as hydrate lenses tilt towards 45°. In addition, Figure 5.11 presents the strength of sediment prior to hydrate formation (Equation 5.4). The contribution of the consolidation effect to the strength of the sediments is dramatically higher than the contribution of the hydrate lens.

5.4 Discussion

5.4.1 Effective media models and bounds

Effective media models provide over-all estimates of properties. Conversely, these models can be used to estimate hydrate saturation from measured physical properties (Berryman and Berge 1996). Effective properties depend on the volume fraction, material properties of the components, and their geometric distribution and shape. Tables 5.1 and 5.2 list common effective media models and their assumptions. In addition, the properties of mixtures are bound between upper and lower limits.

Upper and lower bounds

Series and parallel bounds provide the broadest range for a composite material and depend solely on the volume fraction and properties of the individual constituents. The Hashin-Shtrikman bounds constrain the physical properties to a tighter range (Hashin

and Shtrikman 1962; Hashin and Shtrikman 1963). However, these bounds assume that the overall medium exhibits homogeneous physical properties. The application of Hashin-Shtrikman bounds requires that the physical properties of the medium do not change with the variation of the measurement orientation. Hydrate-bearing fine-grained sediments consist of hydrate lenses that are usually parallel to each other therefore exhibit extreme heterogeneity. Consequently, parallel and series bounds remain the only bounds to constrain the effective properties in these conditions (Figures 5.12 and 5.13).

Estimation models

Wood's formula informs the shear modulus when all the components in the composite share the same shear modulus. The Voigt-Reuss-Hill theory presents an approximate estimation without the specification of geometrical distributions (Hill 1952). (Kuster and Toksöz 1974) developed an explicit shape model that considers spheres, needles, disks and penny cracks (Berryman 1980; Berryman 1980; Te Wu 1966; Walpole 1969; Walsh 1965). Self-consistent models improve the Kuster and Toksoz model but do not yield explicit solutions (Berryman 1995). Note that the original Kuster and Toksoz model and self-consistent model still assumes a global homogeneous medium. Therefore, they do not apply to hydrate-bearing fine-grained sediments. Modification of these models by the control of inclusion orientations enables an accurate prediction of physical properties of an anisotropic medium (Ghosh et al. 2010).

Comparison between numerical simulations and effective media theories

Figure 5.12 illustrates the numerical simulation results of bulk modulus and the comparison with a number of effective medium models. Hashin-Shtrikman bounds do not constrain the bulk modulus effectively in this highly inhomogeneous geometrical condition. None of Kuster-Toksoz or self-consistent models that use disk and penny-crack shaped inclusions predict the bulk modulus of the sediments well.

Figure 5.13 compiles the numerical results of thermal conductivity of hydrate-bearing fine-grained sediments and compares this data to theoretical bounds. Parallel and

series bounds constrain all the simulation results. However, it is clear that the Hashin-Shtrikman bounds do not apply to lens-shaped hydrate distribution in fine-grained sediments. Similarly, Archie's law assumes pore-filling morphology. Therefore, the equation requires careful reassessment when applied to fine-grained sediments.

5.4.2 Potential testing biases of mechanical properties

Boundary effects become significant when the assessment of strength and stiffness uses square specimens. Figures 5.14 presents the shear strength of the sediments with frictional interface as a function of hydrate mass orientation. When the weak layer interconnects with the shear band in the soil, the soil strength dramatically decreases. The interconnection in a square specimen most effectively occurs when the title angle equals 30° and 60°. Consequently, the shear strength q exhibits two valleys correspondingly. However, the shear band that cuts the constant stress boundary at 30° yields less resistance in comparison to the shear band along the 60° weak line that crosses the predetermined displacement boundary. Therefore, the strength of the specimen at 30° is lower than at 60°.

The two valleys in the strength of the specimen are due to the boundary effect and do not represent the true large strain mechanical behavior of hydrate-bearing sediments. Therefore, laboratory tests should use long specimens to ensure that the shear band does not cross the displacement-controlled boundaries. Figure 5.15 demonstrates the location of shear bands and hydrate lens in a long specimen. It requires that the geometry satisfy the relation below,

$$h > a + 2z = a + b\tan\theta \tag{5.8}$$

where a is the hydrate lens length, b is the specimen width/diameter, $\theta = 45° + \varphi/2$ and φ is the friction angle of the sediments. When the friction angle φ is 30° and a = 0.6b, the length of the specimen should be larger than 2.33 times of the specimen width/diameter. The simulation in this study use a length to width ratio of 2.5.

5.6 Conclusions

The characterization of the physical properties of hydrate-bearing fine-grained sediments is critical to stability analyses, volume change and settlement, and for the design of gas production strategies. Inherent difficulties limit the validity of in situ characterization, coring, and laboratory studies.

Therefore, theoretical models and numerical experiments become essential to estimate the physical properties of hydrate-bearing fine-grained sediments. Such an effort in this chapter allow us to conclude:

- Hydrate distribution in fine-grained sediments is primarily particle-displacive (Chapters 3 and 4). The interfaces between hydrates and sediments are rough and jagged.
- The cryogenic suction during hydrate formation alters the physical properties of the sediment that surrounds hydrate lenses and nodules.
- Assumptions in effective media models have to reflect the essential characteristics of hydrate distribution in fine-grained sediments. Assumptions in Hashin-Shtrikman bounds are incompatible, and series/parallel bounds should be considered.
- Laplacian properties of hydrate-bearing sediments with a single lens vary with the hydrate mass orientation, rendering elliptical anisotropy. Sediments with cross-lenses are not sensitive to hydrate orientation.
- The strength of stable hydrate-bearing fine-grained sediments is higher than that of normally consolidated sediments due to the sediment compaction during hydrate formation. The strength decreases dramatically during gas production as slippage occurs along the gas-filled hydrate-sediment interface.
- Experimental as well as numerical simulations are affected by boundary effects. The presence of hydrates invalidates common geometric guidelines used for sediment testing. In particular, longer specimens are required to evaluate the shear strength to avoid boundary related biases.

Table 5.1 Parameters used in analyses and simulations

(a) Thermal properties

	k_T [W m^{-1} K^{-1}]	c_p [J kg^{-1} K^{-1}]	ρ [kg m^{-3}]
Hydrate	0.57[a]	2031[b]	937
Wet clay	1.8	1126	1800

[a](Huang and Fan 2005), [b](Waite et al. 2009).

(b) Mechanical: Small strain

Property	Hydrate[a]	Clay + Water (e = 0.33)[b]
Density, ρ [kg m^{-3}]	937	1800
Elastic Modulus, E [GPa]	9.56	4.31
Bulk Modulus, B [GPa]	8.39	3.59
Shear Modulus, G [GPa]	3.65	1.66
Poisson's Ratio, v [ ]	0.31	0.30

[a](Helgerud et al. 2009), [b]Estimated with the average of Hashin-Shtrikman bounds, clay mineral properties B = 12 GPa (Vanorio et al. 2003), G = 6 GPa, water B = 2.2 GPa , G = 0 GPa.

(c) Mechanical: Large strain

Clay (Cam-clay model)	
Initial effective stress	σ'_0 = 500 kPa
Poisson's ratio	v = 0.3
Compression index	C_c = 0.17
Swelling index	C_s = 0.017
Void ratio at 1 kPa	e_{1kPa} = 0.84
Failure stress ratio	M_f = 1.20
Initial void ratio	e_0= 0.33

Hydrate (Elasto-plastic model)	
Initial stress	σ'_0 = 500 kPa
Poisson's ratio	v = 0.31
Elastic modulus	E = 9.56 GPa[a]
Yield stress	σ'_y = 5000 kPa[b]

[a](Helgerud et al. 2009), [b]selected according to (Durham et al. 2003).

Table 5.2 Upper and lower bounds-models

Models	Geometrical assumptions	Formula
Parallel and Series[a]	No limitation	Upper: $K_T = \sum f_i K_i$ Lower: $K_T^{-1} = \sum f_i K_i^{-1}$
HS-Elastic[b]	Isotropic medium	$B_T^{\pm} = B_1 + f_2 \Big/ \left[(B_2 - B_1)^{-1} + 3f_1 (3B_1 + 4G_1)^{-1} \right]$ $G_T^{\pm} = G_1 + f_2 \Big/ \left[(G_2 - G_1)^{-1} + 6f_1 (B_1 + 2G_2) / \left[5G_1 (3B_1 + 4G_1) \right] \right]$
HS-Laplacian[c]	Isotropic medium	$K_T^{\pm} = K_1 + f_2 \Big/ \left[(K_2 - K_1)^{-1} + f_1 / (3K_2) \right]$

Note the upper and lower bounds in the Hashin-Shtrikman theory are obtained by switching the components. [a](Mavko et al. 2009); [b]Hashin and Shtrikman 1963; [c]Hashin and Shtrikman 1962.

Table 5.3 Physical models

Models	Geometrical assumptions	Formula
Wood's formula[a]	Isotropic medium	$V=\sqrt{G_T/\rho}$, $G_T^{-1}=\sum f_i G_i^{-1}$, $\rho_T=\sum f_i\rho_i$
Voigt-Reuss-Hill[b]	No limitation	$K_T=\left(K_T^U+K_T^L\right)/2$, $K_T^U=\sum f_i K_i$, $\left(K_T^L\right)^{-1}=\sum f_i K_i^{-1}$
Kuster and Toksoz[c]	Isotropic medium[d]	$\left(K_T-K_m\right)\left(K_m+4G_m/3\right)/\left(K_T+4G_m/3\right)=\sum f_i\left(K_i-K_m\right)P^{mi}$ $\left(G_T-G_m\right)\left(G_m+\zeta_m\right)/\left(G_T+\zeta_m\right)=\sum f_i\left(G_i-G_m\right)Q^{mi}$
Self-consistent[e]	Isotropic medium[d]	$\sum f_i\left(K_i-K_T\right)P^{Ti}=0$ $\sum f_i\left(G_i-G_T\right)Q^{Ti}=0$

[a](Wood 1964); [b](Hill 1952); [c](Kuster and Toksöz 1974); [d]Contains randomly orientated inclusion shapes: spheres, needles, disks and penny crack; [e](Berryman 1980).

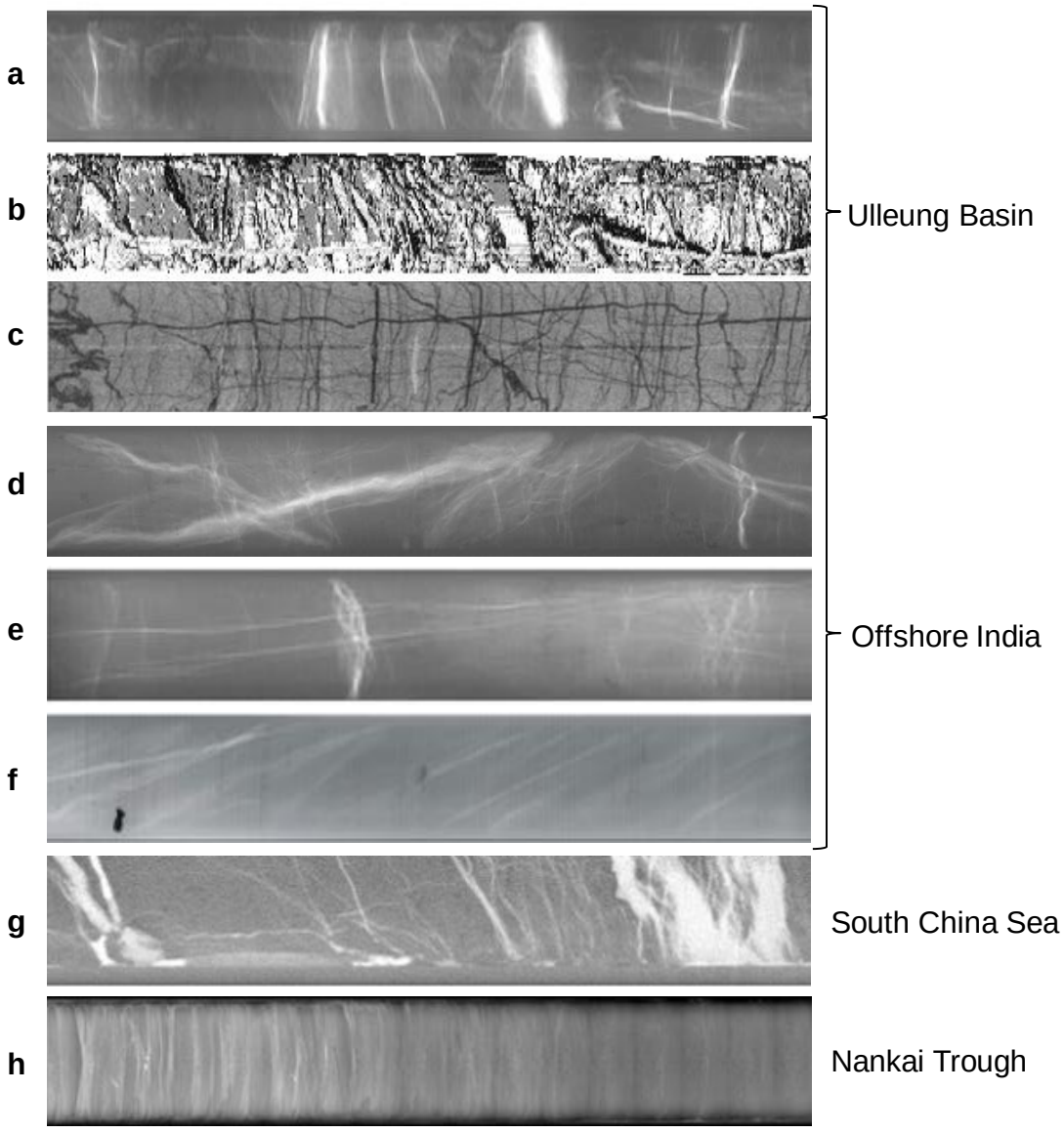

Figure 5.1 Segregated hydrate in fine-grained sediments: Natural specimens. X-ray projections (a, d, e, f, g, h) and slices of CT scans (b, c). Sources: [a,b,c](Lee et al. 2011); [d](Collett et al. 2008); [e](Rees et al. 2011); [f](Boswell et al. 2007); [g](Zhang et al. 2014); [h](Yamamoto et al. 2012).

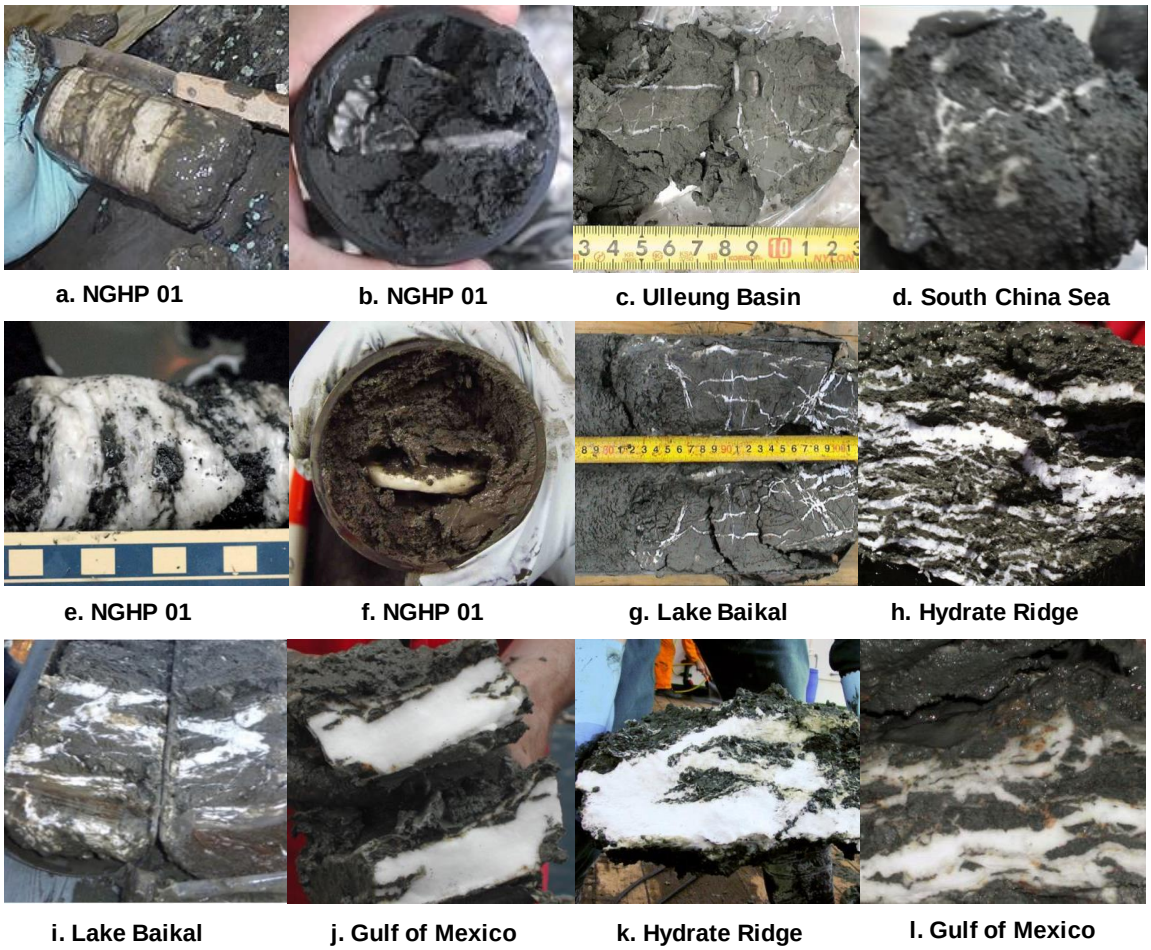

Figure 5.2 Segregated hydrate in fine-grained sediments: Natural specimens. Photographs obtained immediately after recovery and fast depressurization. Sources: (a, b, e, f) image courtesy of NGHP 01; (c) (Park et al. 2008); (d) (Zhang et al. 2014); (g, i) courtesy to Oleg Khlvstov; (h, j, k, l) courtesy of GEOMAR.

(1) Horizontal slice

(2) Vertical slice

(3) Hydrate filled fracture

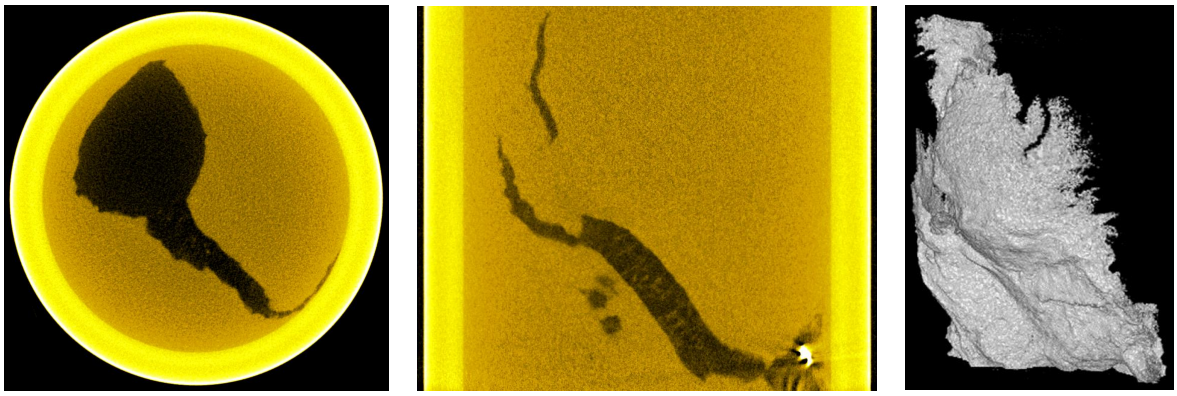

Figure 5.3 Segregated hydrate in fine-grained sediments: Laboratory study. Formation in gas-driven fractures (Chapter 4).

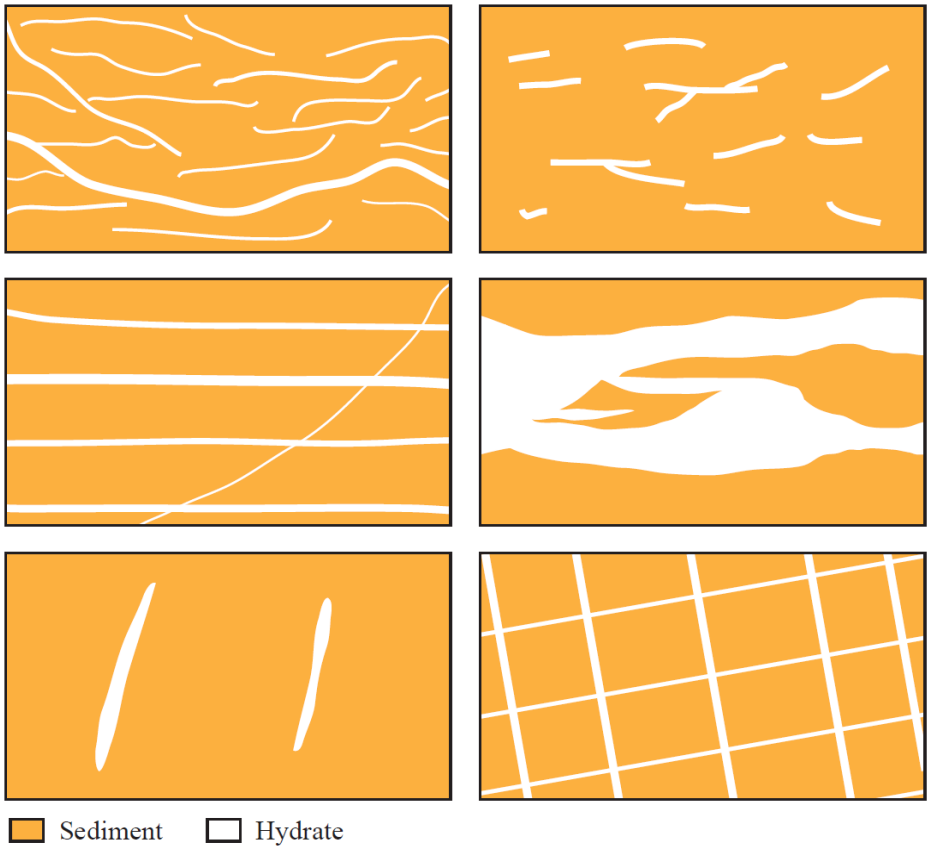

Figure 5.4 Segregated hydrate morphology in fine-grained sediments: Typical structures.

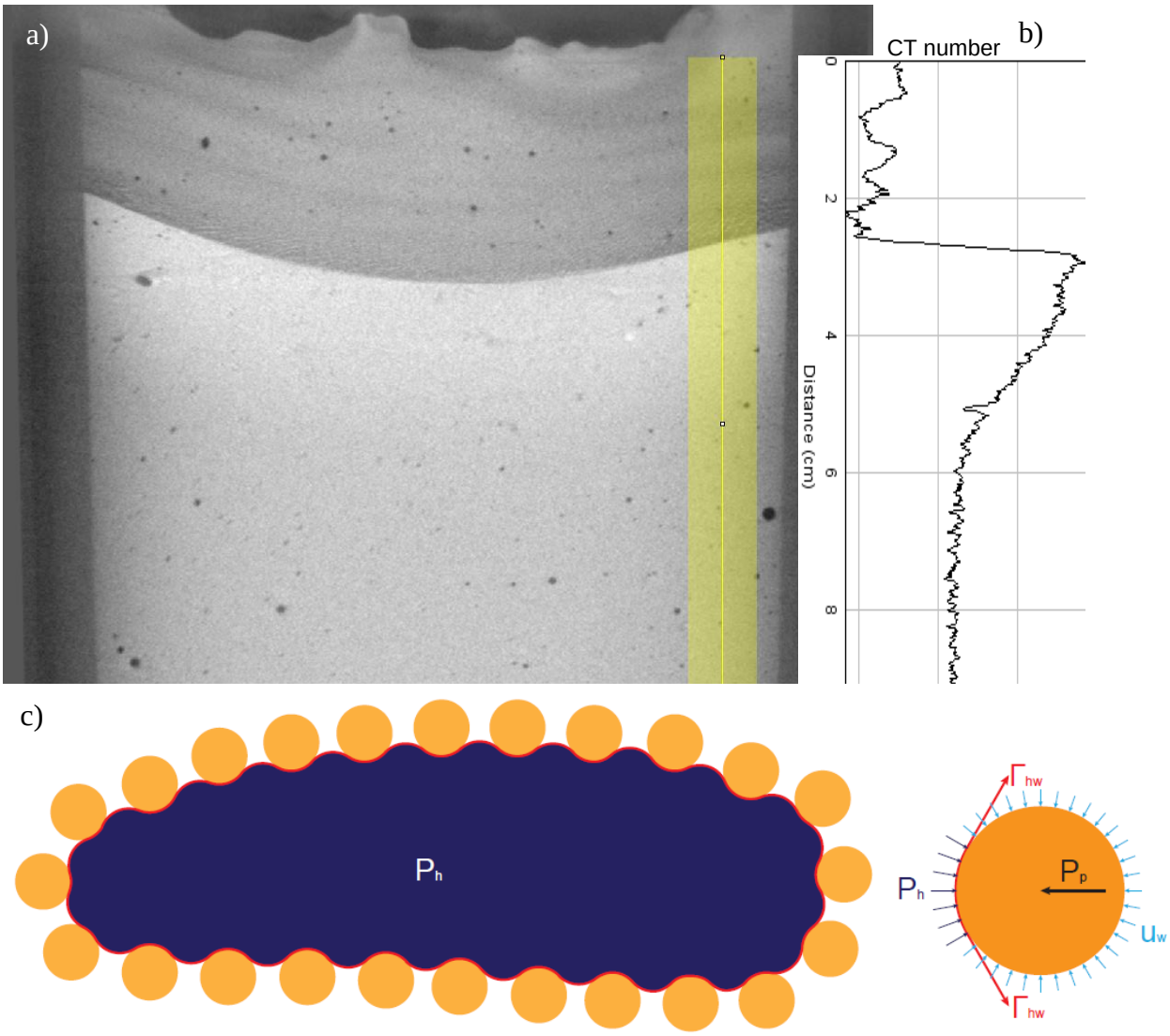

Figure 5.5 Cryogenic suction during ice/hydrate formation. a) Vertical slice of the 3-D image of a kaolinite specimen as the freezing front advances from the top, b) The CT number along the vertical direction that corresponds to the highlighted line, and c) Particle-scale equilibrium between the ice/hydrate mass, the pore fluid and sediment grains.

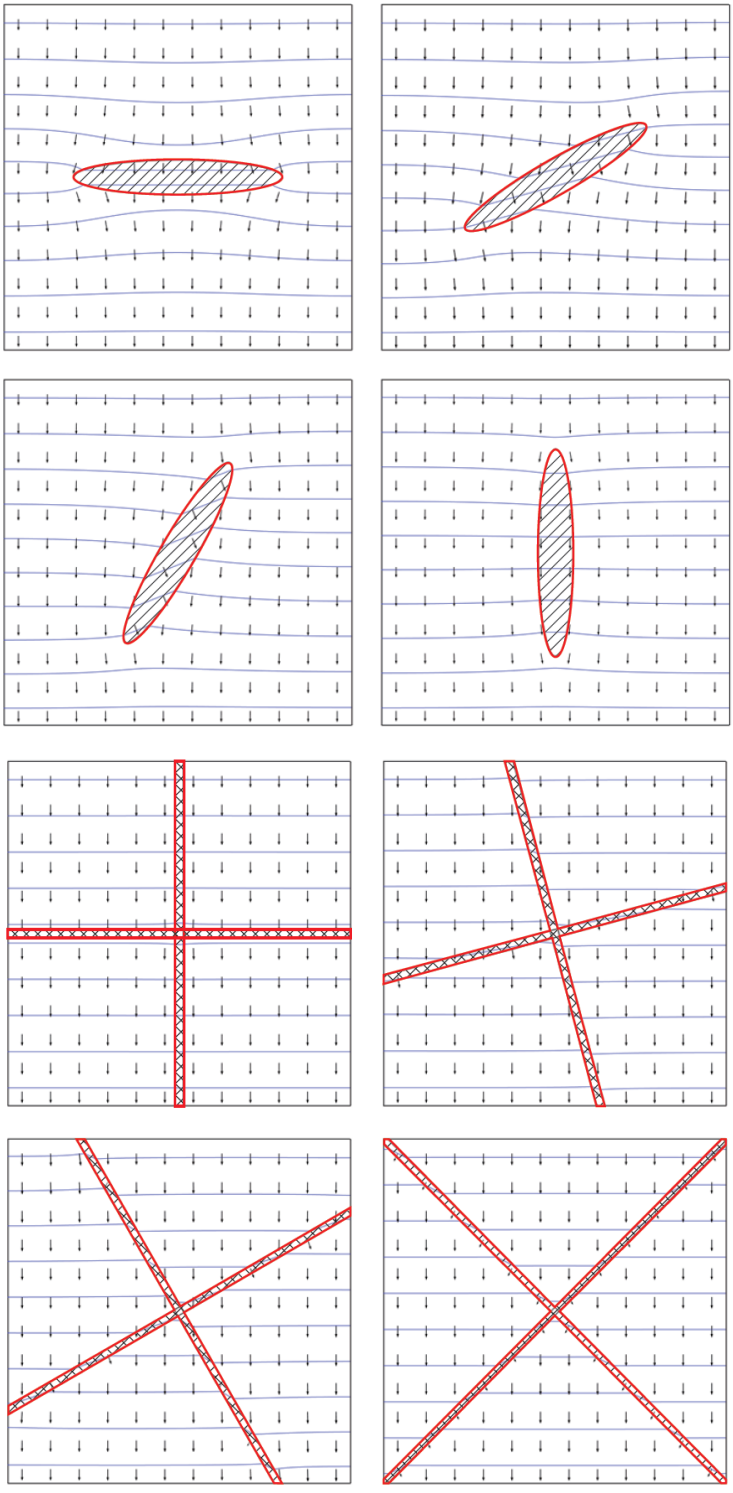

Figure 5.6 Lenses distribution and the influence on thermal conduction fields. Arrows denote the heat flow direction. Horizontal lines represent the temperature contour fields.

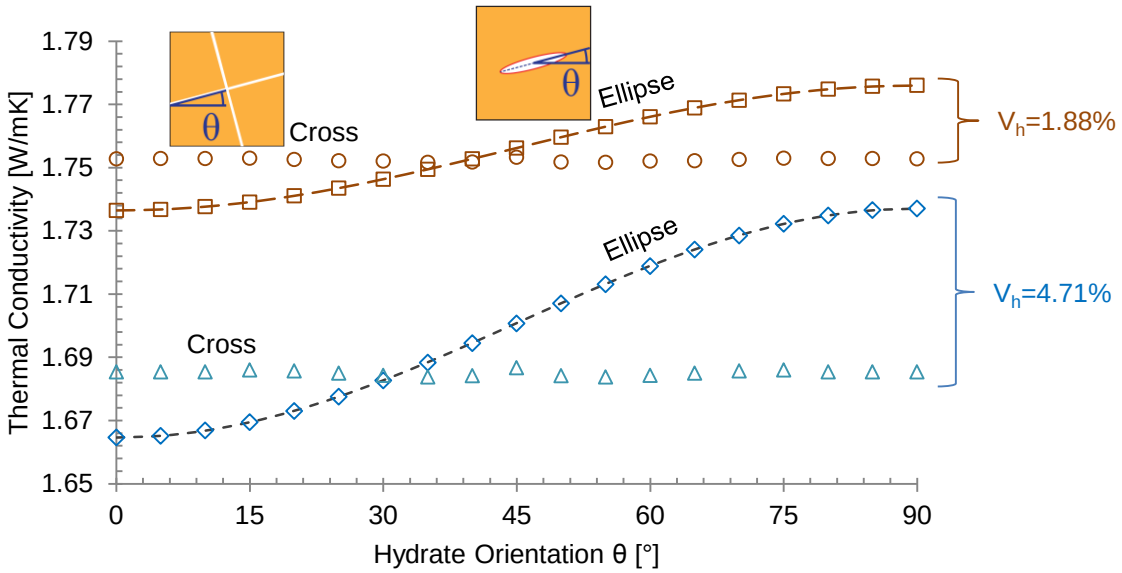

Figure 5.7 Effective thermal conductivity of hydrate-bearing fine-grained sediments as a function of hydrate mass orientation θ. Lines represent physical models; dots are numerical simulation results.

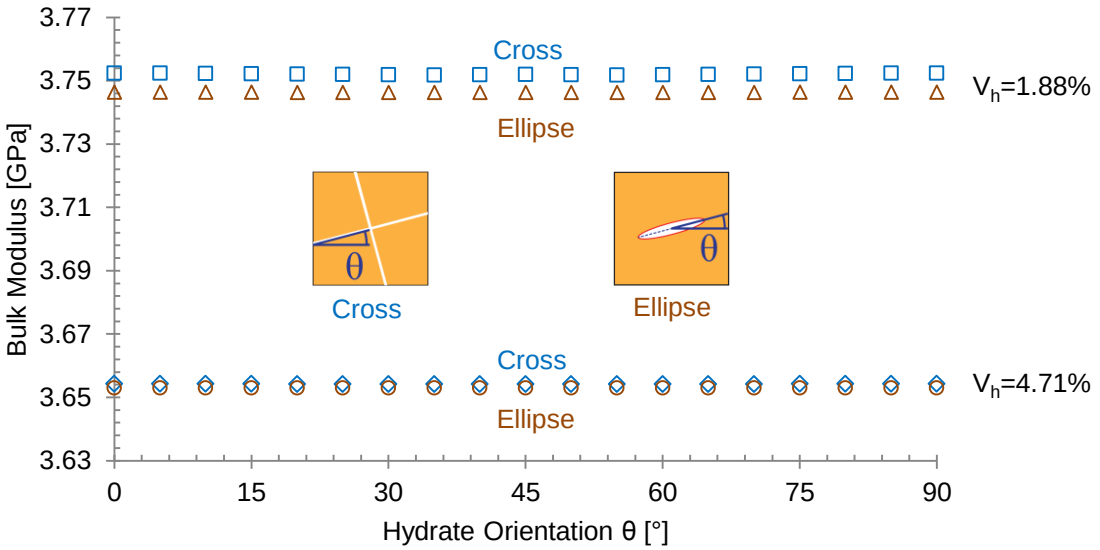

Figure 5.8 Effective bulk modulus of hydrate-bearing fine-grained sediments as a function of hydrate mass orientation θ. Lines represent physical models; dots are numerical simulation results.

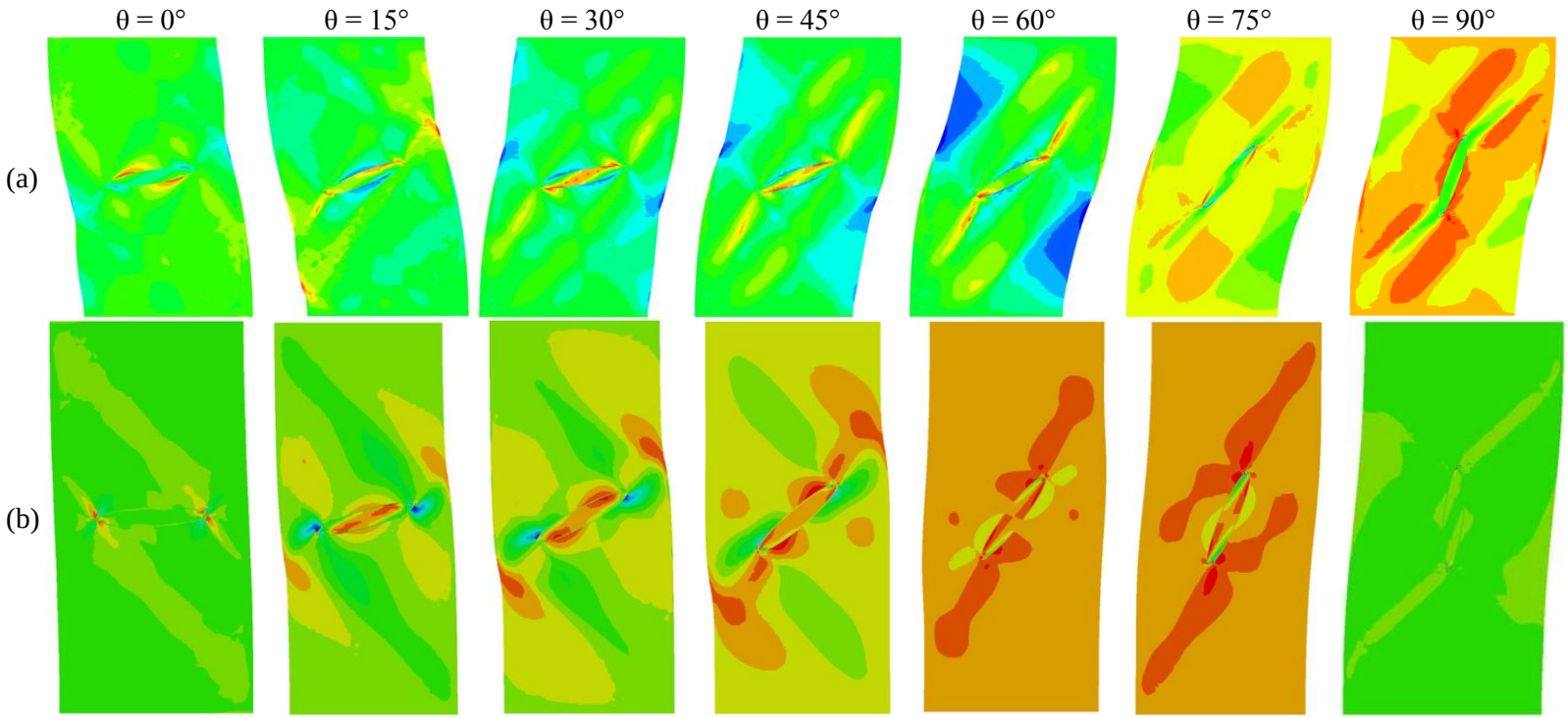

Figure 5.9 Fine-grained sediment with a single segregated hydrate lens subjected to shear. In-plane shear stress fields for various lens orientation θ. (a) Frictional hydrate-sediment interface, (b) Non-slip hydrate-sediment interface.

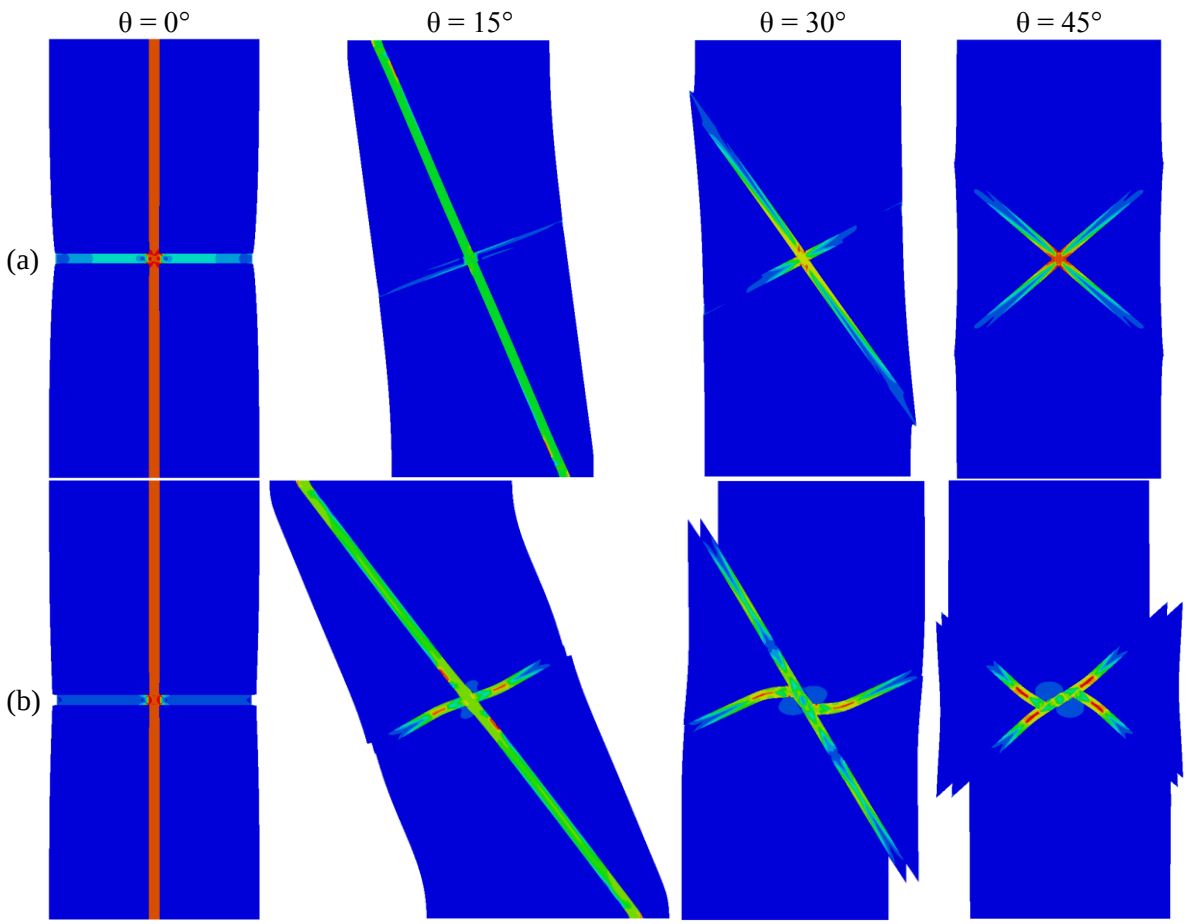

Figure 5.10 Fine-grained sediment with two normally-intersecting hydrate lenses at different orientation θ. Von-Mises-stress = $([(\sigma_1-\sigma_2)^2+(\sigma_1-\sigma_3)^2+(\sigma_3-\sigma_2)^2]/6)^{1/2}$ fields. (a) Frictional hydrate-sediment interface, (b) Non-slip hydrate-sediment interface.

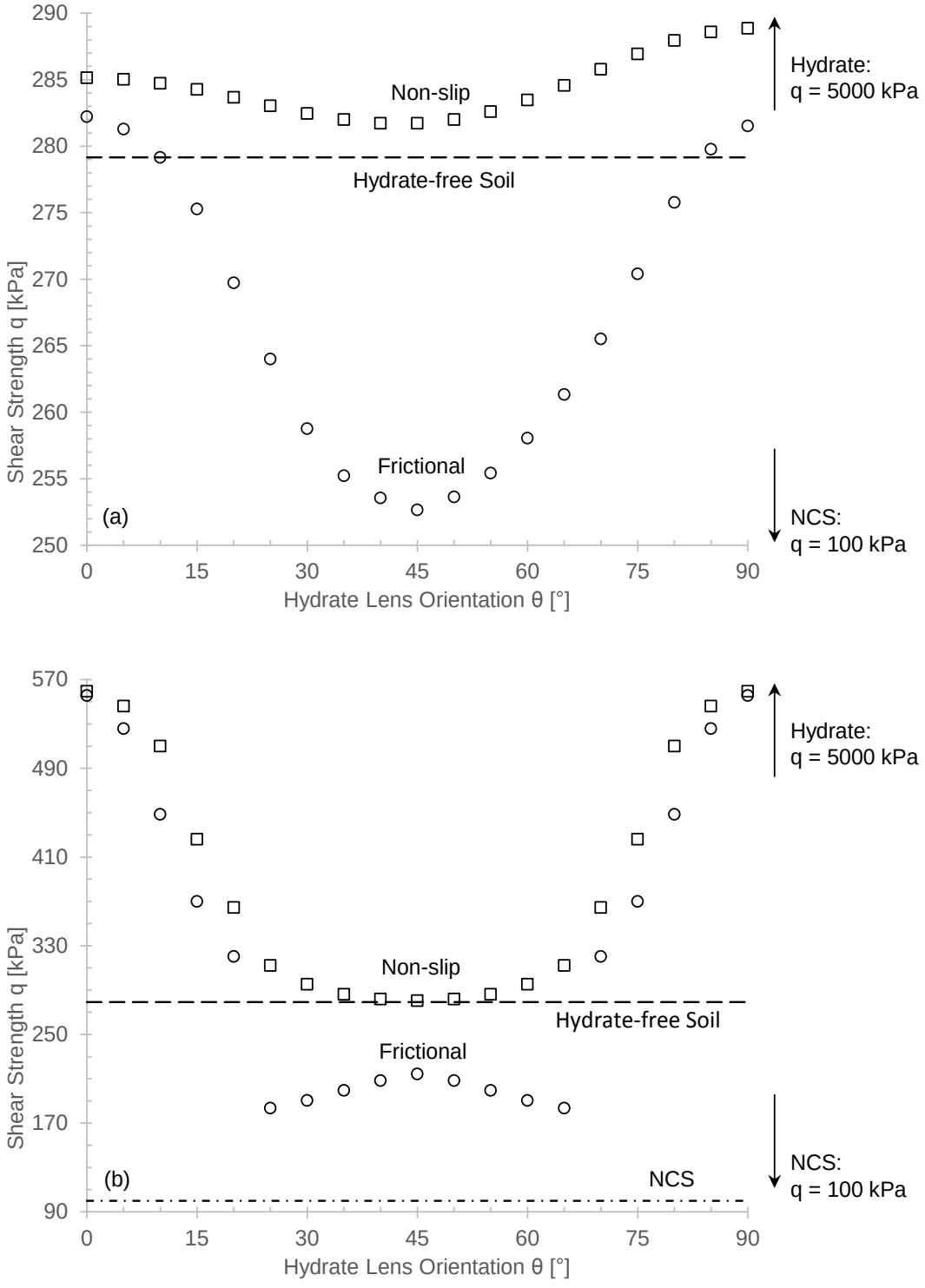

Figure 5.11 Shear strength of segregated-hydrate in fine-grained sediments with frictional and non-slip hydrate-sediment interface as a function of hydrate orientation θ. (a) Fine-grained sediment with a single segregated hydrate lens, (b) Fine-grained sediment with two normally-intersecting hydrate lenses.

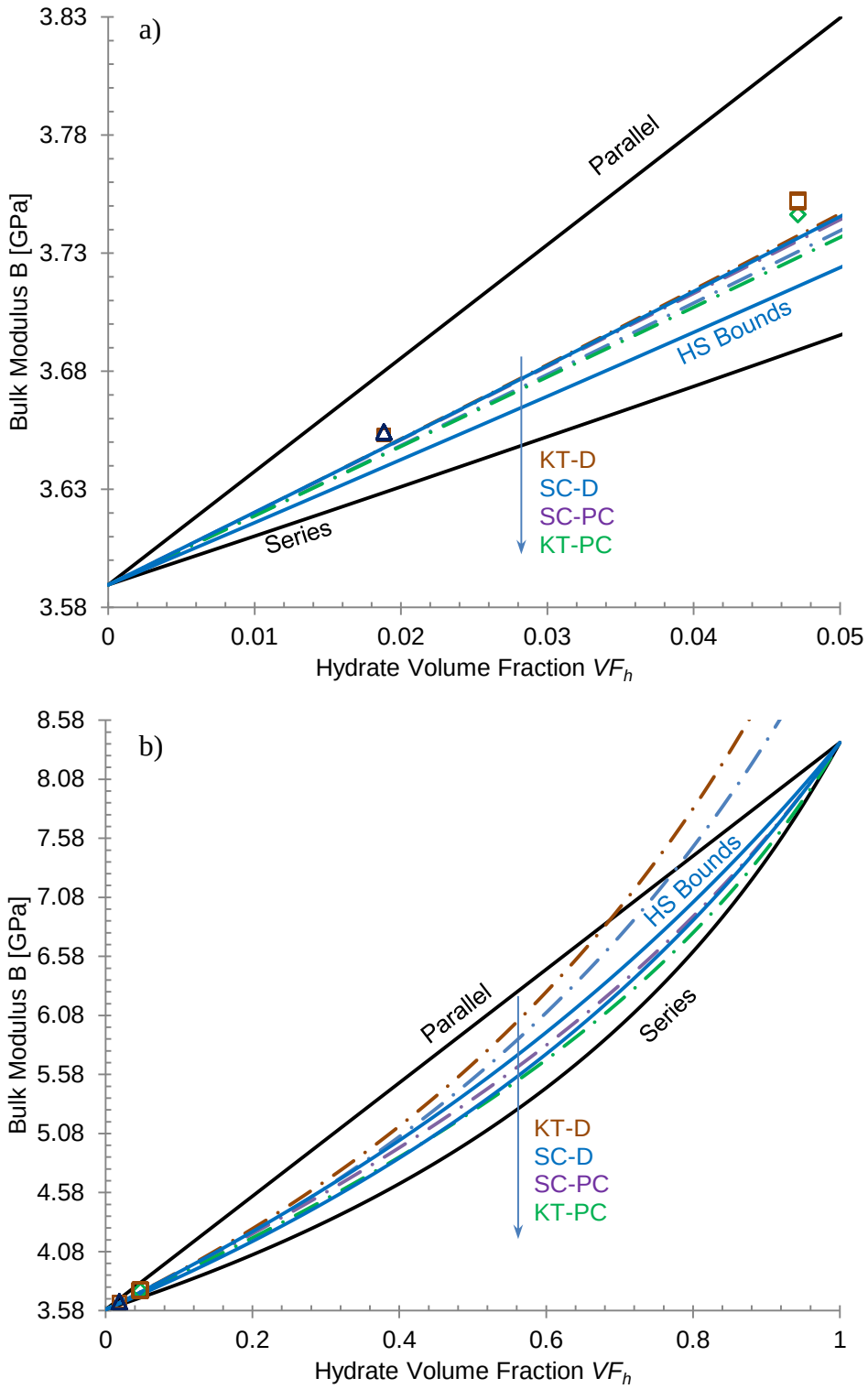

Figure 5.12 Bulk modulus of fine-grained sediments with segregated hydrate. Comparison between theoretical bound (continuous lines), physical models (dotted lines) and numerical simulations (symbols). Note: KT-D = Kuster-Toksoz Disk, KT-PC = Kuster-Toksoz Penny Crack, SC-D = Self-Consistent Disk, and SC-PC = Self-Consistent Penny Crack. (In collaboration with Seth Mallett).

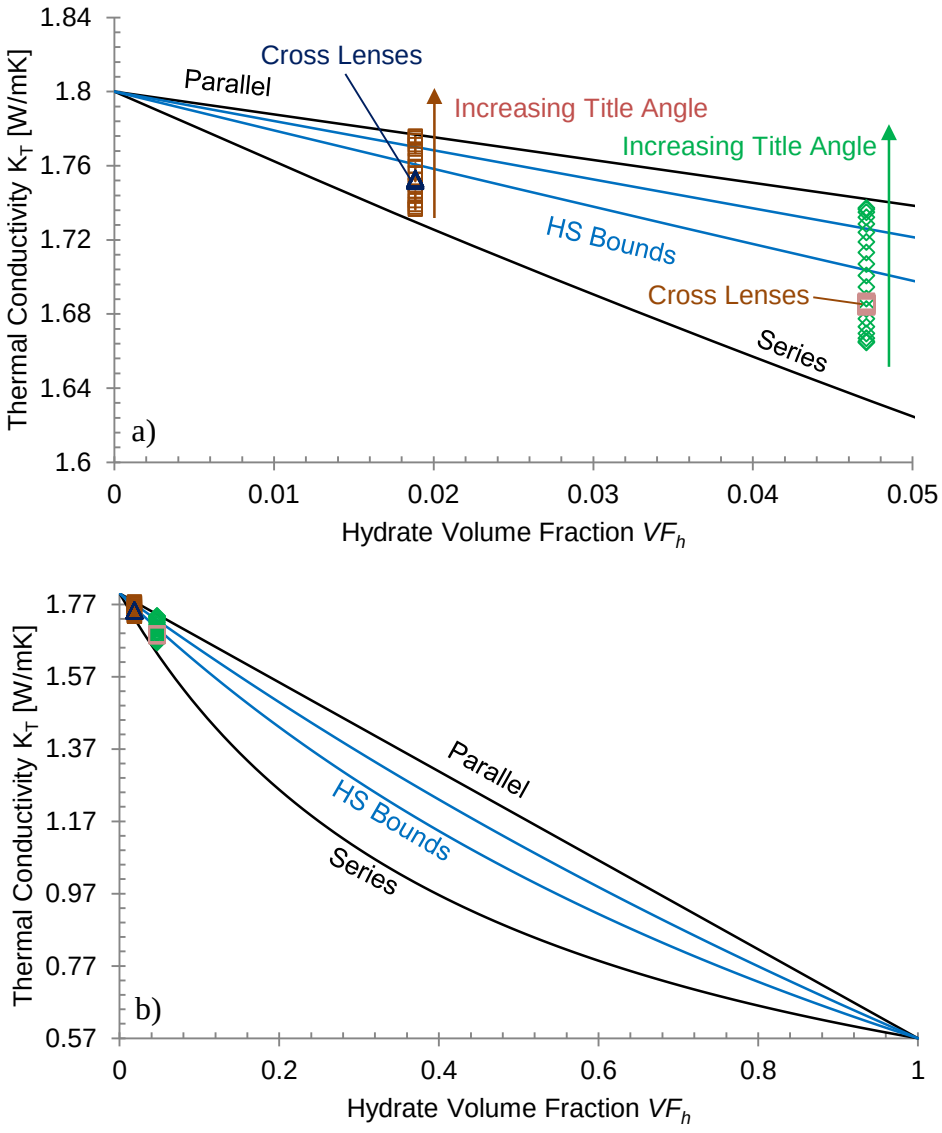

Figure 5.13 Thermal conductivity of fine-grained sediments with segregated hydrate. Comparison between theoretical bound (continuous lines) and numerical simulations (symbols).

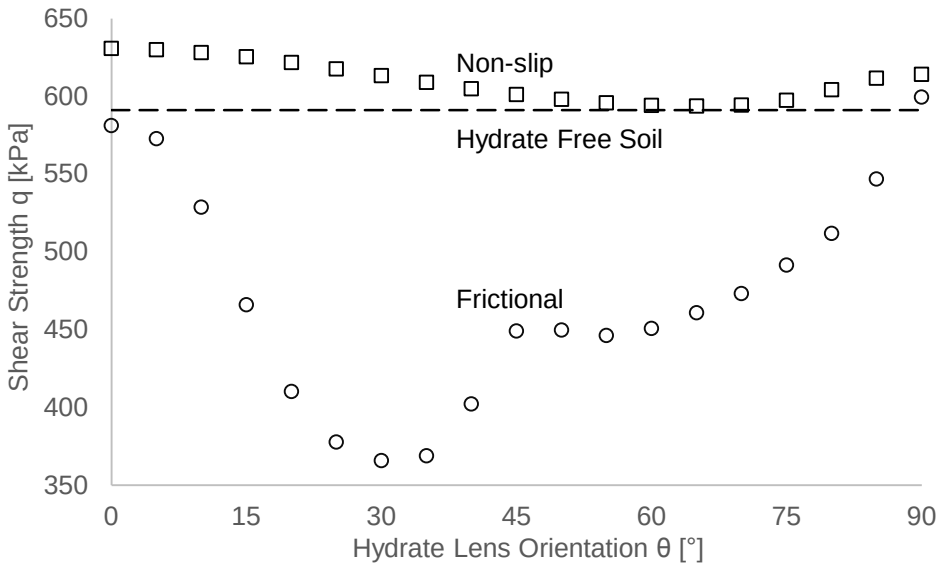

Figure 5.14 Boundary effect in square specimens.

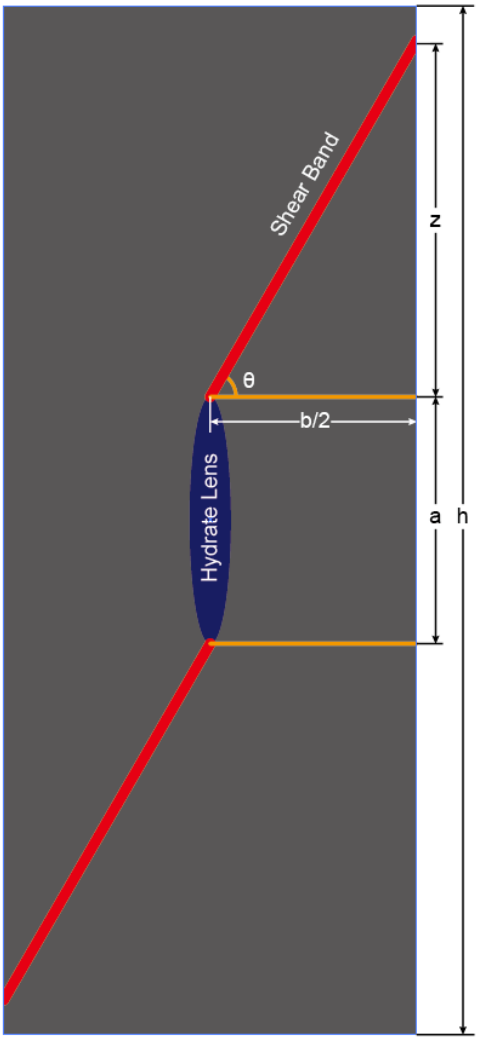

Figure 5.15 Requirement on specimen length to eliminate boundary effects.

CHAPTER 6

GAS PRODUCTION FROM FINE-GRAINED HYDRATE-BEARING SEDIMENTS

6.1 Introduction

Gas production from hydrate-bearing sediments has the potential to change the world's energy supply (Boswell and Collett 2011). Research on gas production from hydrate-bearing sediments has focused on coarse-grained sediments. Field tests include Mallik in 2007 and 2008 (Canada —(Dallimore et al. 2012)), Mount Elbert in 2007 and Ignik Sikumi, in 2012 (USA — (Hunter et al. 2011); (Schoderbek et al. 2013)), and the Nankai Trough in 2013 (Japan —(Yamamoto et al. 2014)). Further gas production tests from coarse-grained sediments will commence at the Nankai Trough site in 2017 (www.japantimes.co.jp), in the South China Sea in 2017 (news.xinhuanet.com), and in the Gulf of Mexico in 2018 (www.aapg.org). South Korea and India are contemplating similar field tests ((Kim et al. 2011; Kumar et al. 2014)).

Fine-grained sediments host over 90% percent of the global gas hydrate accumulations (Boswell and Collett 2006). However, gas production from fine-grained sediments has been discarded and no field tests have been proposed (Boswell et al. 2012). This situation reflects a number of unique challenges associated with fine-grained sediments that limit the economic viability of gas production. First, the small pore size in fine-grained sediments limits fluid permeability and trigger high capillary phenomena. Second, hydrate formation in fine-grained sediments is "particle-displacive" and forms nodules, chunks, lenses and veins. Third, hydrate dissociation is accompanied by large volumetric strains. These factors inhibit or even prevent gas production by conventional methods.

Standard sediment classification systems fail to recognize the preponderant role of fines (Park and Santamarina, 2016). Figure 6.1 illustrates a number of these issues. While coarse-grained particles may account for more than 80% of the total weight, fines control fluid flow, define pore size and capillary phenomena, constrain gas flow and gas

entrapment. This chapter explores the challenges of gas production in fine-grained sediments. It also presents a potential strategy for gas production from fine-grained hydrate-bearing sediments.

6.2 Gas Flow Patterns in Sediments

Gas flow in sediments can take place through either connected pores or gas driven fractures. Capillary pressure and effective stress define the boundaries for these regimes.

6.2.1 Capillary pressure

The interfacial tension between water and gas Γ_{gw} can sustain a pressure difference C_{gw} between water u_w and gas P_g,

$$C_{gw} = P_g - u_w \tag{6.1}$$

In addition to surface tension, the capillary pressure C_{gw}, depends on the pore size d and contact angle θ as well (Laplace equation),

$$C_{gw} = \Gamma_{gw} \frac{4\cos\theta}{d} \tag{6.2}$$

The interfacial tension depends on temperature, gas pressure and gas type (Espinoza and Santamarina 2010; Massoudi and King 1974). The interfacial tension between methane and water decreases by 11.6% as the gas pressure increases from 0.1 MPa to 7.5 MPa at 25°C (Massoudi and King 1974). The contact angle reflects the relative affinities between gas, mineral and water.

The critical pore throat size d^* that marks the break-through is (Espinoza and Santamarina 2010),

$$d^* = \frac{ke}{S_s \rho} \exp(\alpha \sigma_x) \tag{6.3}$$

where the geometric factor k is between 6 and 12, e is the void ratio, S_s is the specific surface of the sediment, ρ is mineral density, σ_x is the pore size standard deviation, and α is the factor that measures the deviation of the critical pore throat from the mean pore throat.

6.2.2 Balance between capillary pressure and effective Stress

There are three boundaries that determine the sediments flow behavior. These boundaries are identified next.

Boundary 1. When the effective stress σ' is larger than the characteristic capillary pressure C^*_{gw}, the fabric of the soil skeleton does not change due to the influence of the capillary pressure.

$$\sigma' = C^*_{gw} = \Gamma_{gw} \frac{4\cos\theta}{d^*} \tag{6.4}$$

Boundary 2. When the difference between the gas and water pressure is larger than the characteristic capillary pressure of the sediment, gas can potentially invade into the pore space (Figure 6.2a).

$$P_g - u_w = C^*_{gw} \tag{6.5}$$

Note that the unbalanced force between the water and gas transfers to the capillary tube. The assumption in Figure 6.2a is that the capillary tube is rigid and has sufficient strength. However, in reality, the capillary tube is compressible and has strength limitations. Therefore, the unbalanced forces can deform or even break the capillary tube.

Boundary 3. The soil skeleton functions as the capillary tube and the effective stress caps the strength. Figure 6.2b demonstrates that when the difference between the gas and water pressure is larger than the effective stress, it is potential for cracks to form in the sediment (Shin and Santamarina 2011).

$$P_g - u_w = \sigma' \tag{6.6}$$

The pressure difference between gas and water, effective stress and characteristic capillary pressure determine the macro-scale behaviors of the sediment. Figure 6.3 divides the entire σ'-(P_g-u_w) field into six different zones based on the three boundaries:

- *Zone N1.* P_g-u_w< σ'<C^*_{gw}. The effective stress limits gas flow.
- *Zone N2.* P_g-u_w<C^*_{gw} <σ'. The characteristic capillary pressure limits gas flow.
- *Zone Y1.* σ'<P_g-u_w<C^*_{gw}. Gas does not have the capability to invade into sediment pores due to the water surface tension. Gas flow only occurs through gas-driven fractures (Shin and Santamarina 2011).
- *Zone Y2.* C^*_{gw}<P_g-u_w<σ'. Gas flow only occurs through the connected pores. The soil fabric does not change due to gas flow.
- *Zone Y3.* σ'<C^*_{gw}<P_g-u_w. Gas flow is primarily through the gas-driven fractures. Dynamic gas flow can invade into sediment pores simultaneously.
- *Zone Y4.* C^*_{gw}<σ'<P_g-u_w. Gas flow is typically through the connected pores. Meanwhile, a dynamic gas flow can potentially create gas-driven fractures by the effect of dragging force (miscible fluid case in (Shin and Santamarina 2011)), which dramatically accelerates the gas flow rate.

Barrier pressure difference. We define the barrier pressure difference ΔP_b (red solid line in Figure 6.3) for gas flow in the sediments as,

$$\Delta P_b = P_g - u_w = \begin{cases} \sigma' & if \quad \sigma' < C^*_{gw} \\ C^*_{gw} & if \quad \sigma' \geq C^*_{gw} \end{cases} \tag{6.7}$$

6.2.3 Gas flow pattern: Field data analysis

Table 6.1 summarizes the reservoir locations, effective stress, pore pressure, temperature and sediments characteristics in natural hydrate-bearing sediments. Figure 6.3 illustrates the same data plotted in terms of the vertical effective stress versus the pressure difference between gas and water, both normalized by the characteristic capillary pressure. (Dai et al. 2012) provide detailed effective stress and particle size

estimations. We assume the characteristic pore throat is 1/10 of D_{10} and plot the pressure difference between the gas and water of 1 MPa or 3 MPa.

Analyses show that gas does not flow when the water pressure is 3 MPa lower than the gas pressure at a number of sites that include Blake Ridge (Table 6.1). Gas flow through pores usually occurs in coarse-grained sediments. Shallow marine sediments in conditions where effective stress is low favor gas flow through gas driven fractures. The pressure difference between the gas and water could be generated through gas pressure increases by thermal stimulation or through decreases in water pressure. Note that the gas pressure in the sediment cannot be larger than the pressure on the hydrate phase boundary during continuous gas production.

6.3 Gas Production in Fine-grained Sediments

There are four methods for gas production from gas hydrate-bearing sediments: depressurization, thermal stimulation, chemical stimulation and CO_2-CH_4 replacement. This section discusses the potential of each method in fine-grained sediments, and notes the importance of the capillary effect to gas production in fine-grained sediments.

This work does not consider the capillary effect on the gas hydrate phase boundary in gas production, as hydrates with the highest curvature dissociate first, and then further hydrate dissociation consumes the residual bulk hydrate at the bulk hydrate phase boundary. Our experimental results in Chapter 4, Figure 4.4 show that the hydrate phase boundary moves from the shifted phase boundary to the bulk hydrate phase boundary as the hydrate dissociation continues. Note that the phase boundary restores to the shifted phase boundary when the continuous dissociation ceases.

Capillary pressure inhibits hydrate dissociation. The depressurization method demands a lower water pressure than the phase boundary pressure to dissociate the residual hydrate. By contrast, the thermal stimulation technique requires a higher temperature at this point to destabilize the residual hydrate. Figure 6.5b illustrates that the gas pressure around the hydrate crystal is higher than the water pressure. The gas

pressure maintains the stability of the residual hydrate before the pressure difference between water and gas exceeds the characteristic capillary pressure.

6.3.1 Depressurization

The most successful gas production technique from gas hydrate sandy reservoirs is depressurization (Dallimore et al. 2012; Hunter et al. 2011; Yamamoto et al. 2014). However, depressurization-driven gas production in fine-grained sediments has a number of limitations.

Gas pressure limitations. Figure 6.5a displays the pressure-temperature (PT) trajectory (from point A to B to C) as depressurization occurs (Sloan and Koh 2007). Gas hydrate does not dissociate before the pressure decreases to point B. Furthermore, fluid pressures lower than point B do not guarantee gas flow in the sediments. Gas flow does not occur until the pressure difference between the gas and water, point B to C (the equivalent of a water pressure decrease from point A to C), exceeds the barrier pressure difference (Equation 6.7).

The site in the Sea of Okhotsk (Table 6.1) is an example of areas of low-temperature fine-grained sediments (Luan et al. 2008). Significant gas production challenges arise at sites when the PT is deep within the hydrate stability field. A large proportion of the pressure decrease is consumed to pull the PT to the hydrate phase boundary, and does not result in any gas production. This condition requires negative water pressure to overcome the barrier pressure difference. Pressures of up to 30Mpa challenge the equipment's capacity to depressurize the reservoir (Figure 6.5b).

Effective stress increases. Whenever the fluid pressure decreases, the force between the particles (effective stress) increases simultaneously. Therefore, the increase in effective stress induces sediment consolidation, accompanied by a reduction in the pore size and hydraulic conductivity. Effective stress in shallow marine sediments ranges from 0 KPa to 500 KPa (50 meters below the sea floor). However, the increase in effective stress in these conditions may reach up to 30,000 KPa. Section 6.4 details the potential impact of changes in effective stress on sediments.

Well production challenges. Sediment volumes contract as the effective stress increases. The decrease in well pressure creates consolidation around the well walls. The volume contraction could be more than 50% in soft sediments (Chong and Santamarina 2016). This contraction causes sediments subsidence and potential well stability issues. Furthermore, geometric restrictions prevent gas driven fractures in these conditions (Figure 6.6). Therefore, the slow gas flow rate through the pores in fine-grained sediments is an inherent limitation of the well production method.

Flow rate limitations. The characteristic capillary pressure reaches 1 MPa when the pore size decreases to 1.5μm, and 5 MPa for 0.3μm pores. Well production costs increase as the particle size decreases, due to the lower hydraulic conductivity in these conditions regardless of the capillary barrier.

6.3.2 Thermal stimulation

Water and sediments consume the majority of the injected thermal heat in production wells, with minimal heat consumed by gas hydrates. Therefore, pure thermal stimulation is uneconomical for this reason (Moridis 2008; Moridis et al. 2007). Figure 6.5a demonstrates the PT trajectory from point A to B' to C' to D' during thermal stimulation (Kwon et al. 2008; Sloan and Koh 2007).

The barrier pressure difference determines the minimum required pressure increase from points B' to C' to enable gas production. The slope of the hydrate phase boundary increases with the temperature increase. Therefore, the same amount of pressure increase corresponds to a smaller temperature increase at higher temperatures. This indicates that the thermal stimulation method is more efficient at high temperature sites.

When the PT trajectory deviates from the phase boundary, the gas hydrates completely dissociate. The slope of the pressure increase versus the temperature increase from points C' to D' is significantly flatter than that of the hydrate phase boundary. Therefore, further thermal stimulation that aims to increase the gas pressure becomes inefficient. When gas flow does not commence until point C, it indicates either a low

hydrate saturation rate or alternatively a very soft sediment that traps large volumes of the released gas in the cavities.

6.3.3 Chemical stimulation and replacement

Chemical stimulation and CO_2-CH_4 replacement both rely on the transport of molecules to the reaction front. However, the small pores and high specific surface in fine-grained sediments implicate inefficient substance migration. The Péclet number in fine-grained sediments *Pe* is (Fetter and Fetter 1999; Huysmans and Dassargues 2005),

$$Pe = \frac{V_e d_e}{D_e} \tag{6.9}$$

where V_e is the effective water velocity, d_e is the average grain diameter, and D_e is the effective diffusion coefficient in porous media. The effective water velocity is proportional to the hydraulic conductivity with a given pressure gradient,

$$V_e = \alpha K \tag{6.10}$$

where α is a coefficient that corresponds to the pressure gradient, K is the hydraulic conductivity in cm/s (Ren and Santamarina, 2016),

$$K = a \cdot S_s^{-1.9} \cdot e^b \tag{6.11}$$

where a=1.5×10^{-5}cm/s; *Ss* is the specific surface of the sediments in the unit of m^2/g; e is the void ratio; b=3 for coarse-grained soils and b=3.9 for fine-grained soils. Calculations assume a spherical grain shape, then

$$S_s = \frac{6}{\rho d_e} \tag{6.12}$$

where ρ is the grain density. Equations 6.9 to 6.12 inform the equation below,

$$Pe = \frac{d_e (\rho d_e)^{1.9}}{30 \alpha a e^b D_e} \tag{6.13}$$

The Péclet number is approximately proportional to the cubed grain diameter. The contribution of advection to the process of substance transfer in porous media decreases

dramatically as the grain size decreases. When Pe<1, diffusion dominates the transfer and decreases the transfer speed. Consequently, the chemical transfer in fine-grained sediments is time intensive and uneconomical.

The freshening effect. A number of hydrate dissociation experiments in water with chemicals dissolved exhibit the freshening effect (Østergaard et al. 2002). Gas hydrate dissociation releases fresh water into the environment. The fresh water dilutes all the dissolved components and reduces their concentration. This triggers the movement of the shifted gas hydrate phase boundary back to the bulk gas hydrate phase boundary as gas production continues. Similarly, the freshening effect can also reduce the concentration of any injected chemicals as the gas hydrate dissociates. The chemical stimulation methods detailed above do not permit continuous gas production.

6.3.4 Surface mining in shallow marine sediments

Shallow hydrate-bearing fine-grained sediments are found in Hydrate Ridge (Hovland et al. 1995), the Gulf of Mexico (Pflaum et al. 1986), the Sea of Okhotsk (Luan et al. 2008), and offshore India (Kumar et al. 2014). Shallow marine fine-grained sediments have the potential to accumulate large quantities of hydrates. Firstly, the effective stress in shallow sediments is low, yet the characteristic capillary pressure is high. These circumstances enable large quantities of gas to form cavities. Hydrate forms when these same gasses combine with water. Secondly, the low effective stress places less limitations on gas hydrate formation in comparison to deep fine-grained sediments (see Chapter 3 for detailed discussion). Thirdly, the water supply for gas hydrate formation could potentially come from the sea. By contrast, gas hydrate formation in deep sediments extracts water from the consolidated sediments, a process that requires a large degree of temperature depression. Therefore, shallow fine-grained marine sediments commonly contain large hydrate crystals (Suess et al. 2001).

Figure 6.7 proposes a new concept of surface mining in shallow marine sediments. The circulation of warm water from the sea surface increases the sediment temperature. Gas hydrate in the sediments dissociates upon heat absorption. The increased gas pressure then overcomes the barrier pressure difference to create gas-driven

fractures or drives gas flow through the pores. Membranes or umbrellas approximately the size of a football field then collect the gas or even gas hydrate.

Surface mining benefits. The above method applies to all sediment types. The characteristic capillary pressure is low in coarse-grained sediments due to the large pore size. Therefore, gas production occurs through the connected pores. The low effective stress in shallow fine-grained sediments allows low gas pressures to create gas-driven fractures, which can produce a number of gas flow paths.

A novel concept of gas hydrate harvest. Hydrate formation uses the gas released from the sediments. Methane bubbles from this release rise due to buoyancy. An upside-down container on the sea floor collects the bubbles. Stirring within the container then accelerates the hydrate formation process. The hydrate could then be harvested in the solid form.

6.4 Discussion: Implications

Consolidation. Fine-grained sediments usually possess a high compression index. The effective stress in shallow marine sediments less than 10 meters below the sea floor is usually not larger than 100 kPa. However, the increase in effective stress due to depressurization can be up to 30,000 kPa if the PT of the sites are deep within the hydrate phase boundary. The same amount of effective stress change in kaolinite results in a 50% volume contraction, a pore size reduction from 1000 nm to 100 nm, and a change in the void ratio from 1.38 to 0.2 (Chong and Santamarina 2016). Note that the characteristic capillary pressure is inversely proportional to the pore size. Therefore, the barrier pressure difference increases up to 10 times of the original. The effective stress increase develops in the sediments during well gas production, regardless of the method used. By contrast to depressurization, gas pressure increases due to thermal stimulation do not necessarily increase the effective stress. When we use surface mining techniques in shallow marine sediments, the increased gas pressure can generate gas-driven fractures without an increase in the effective stress. Therefore, the pore size and hydraulic conductivity do not decrease while gas production occurs.

Phase boundary shift. Continuous gas production maintains the bulk hydrate phase boundary. However, a pause in production can restore the shifted phase boundary that resulted from both the salinity and pore size effects. Hydrate then starts to dissociate at lower temperatures if triggered by thermal stimulation or higher pressures if induced by depressurization. Despite the benefits of this technique, a pause in gas production creates a number of economical and operational challenges.

Sediment capacity to trap gas. The fluid volume expands by up to 5 times in undrained and constant pressure conditions (Jang and Santamarina 2016). When the effective stress is higher than the characteristic capillary pressure, the volume expansion releases through pores. Large volume cavities could form in shallow fine-grained sediments, and trap the gas released from hydrate dissociation. Seismic data and in-situ testing of shallow marine sediments reveal this feature (Sultan et al. 2014). Video captured in northern Siberia illustrates sediments remarkable ability to trap methane gas inside these cavities (Siberian Times, 2016).

6.5 Conclusions

The production of gas from hydrate-bearing fine-grained sediments has the potential to impact the world's energy supply. This chapter discusses potential gas production techniques and highlights the critical role of capillarity in fine-grained sediments. During hydrate formation, capillarity leads particle-displacive segregated hydrate morphology. During dissociation and gas production, capillarity and effective stress determine the boundary between gas flow through pores and gas-driven fractures.

Physics-inspired analyses and mechanical models lead to the following observations related to gas production from hydrate-bearing fine-grained sediments:

- A small fines fraction is sufficient for fines-controlled mechanical and conduction properties. Therefore, hydrate reservoirs must be carefully characterized to assess the potential controlling effect of fines.

- Capillarity hinders gas production from fine-grained sediments when the pressure difference between the gas and water does exceed the barrier pressure difference defined by either pore invasion or gas-driven fracture formation.
- Hydrate lenses or nuclei with large curvatures dissociate first. The phase boundary gradually shifts towards the bulk hydrate phase boundary during hydrate dissociation.
- Gas production by depressurization is not technically viable in fine-grained sediments due to sediment compaction, decreasing pore size and fluid conductivity, and increased capillarity.
- Chemical stimulation and CO_2-CH_4 replacement are inefficient and uneconomical in fine-grained sediments due to the slow diffusion-controlled transport.
- Surface mining combined with thermal stimulation arise as a potential strategy to produce gas from near-surface hydrate-bearing fine-grained sediments. Gas escapes the sediment through gas-driven fractures caused by gas expansion and low effective stress conditions.

Table 6.1 Geological conditions present in natural hydrate-bearing sediments [a]

Location	σ' (MPa)	P_0 [b] (m)	D_{10} (μm) Mean	D_{10} (μm) s.dev.	T [c] (°C)	P_{pb} [d] (MPa)	T_{pb} [e] (MPa)	C^*_{gw} (MPa)	References [f]
Mallik	9.137	9.137	285	8.5	7.5	5.79	13.8	0.004	a,b,c
	9.03	9.03	108.4	76.02	7.2	5.60	13.7	0.010	a,b,c
	8.93-10.88	9.9	150	50	8.5	6.48	14.5	0.008	a,b,c
Blake Ridge	2.59	30.58	0.16	0.11	12.9	10.51	25.4	7.057	d,e,f
	3.30	31	0.001	0.0007	15.9	14.50	25.6	1129	d,e,f
	0.03	27.82	0.2	0.14	4.2	3.98	24.5	5.645	g,h,f
Nankai Trough	2.08-2.6	11.79	100	70.13	13.0	10.63	16.2	0.011	i,j
	0.9-1.4	47.99	10	7.01	8.5	6.48	30.1	0.113	k,j
NGHP	0.6	13	0.2	0.14	6.7	5.29	17.1	5.645	l,m,n,o
	0.58	11.07	1.6	1.12	6.7	5.29	15.6	0.706	p,n,o
Cascadia Margin	0.03	6.78	4	0.3	5.5	4.62	11.0	0.282	q,r
	0.13	6.87	2.5	0.2	6.3	5.06	11.1	0.452	q,r,s
Offshore Peru	1.41	39.61	0.01	0.01	8	6.13	28.1	113	t,u
	1.66	52.36	23	8	9.1	6.93	31.0	0.049	u,v
OKushiri Ridge	0.88-0.98	27.16	100	70.13	15.9	14.50	24.3	0.011	w
	0.88-0.91	27.16	0.01	0.01	15.3	13.60	24.3	113	w,x
	0.91	26.62	0.2	0.1	15.4	13.75	24.1	5.645	w
Ulleung Basin	1.36	21	1.5	1.05	7.3	5.66	21.7	0.753	y,z
	1.40	22.18	0.2	0.14	9.6	7.32	22.3	5.645	z,aa
Orca Basin, GOM	0.2-0.4	24.25	0.001	0.0007	4.4	4.07	23.1	1129	ab,ac,ad,ae
Alaminos Canyon, GOM	4	31.3	80	56.10	9.1	6.93	25.7	0.014	af,ae
Sea of Okhotsk	0.02-0.03	8.4	0.45	0.25	2.3	3.19	13.0	2.509	ag,ah
	0.02-0.03	6.7	0.4	0.2	2.3	3.19	10.9	2.823	ag,ah
Mt. Elbert	6.2	6.2	200	140.26	0	2.43	10.2	0.006	ai,aj,ak
	6.61	6.61	80	56.10	1	2.74	10.8	0.014	ai,aj,ak
	6.2	6.2	17	11.92	0	2.43	10.2	0.066	al
Atwater Valley, GOM	0-1.58	13.7	0.01	0.01	5.5	4.62	17.6	113	am,ae
Hydrate Ridge	0.05-1.06	9.46	0.2	0.14	11.2	8.74	14.1	5.645	an,ao,ap

[a]Effective stress, water pressure, and particle size are in agreement with Dai and Santamarina, 2012.
[b]Field water pressure calculations use water depth.
[c]Field site temperature calculations use sea floor temperatures and geothermal gradients if direct data is unavailable.
[d]Pressure calculations at the phase boundary use the bulk hydrate phase boundary and assume that the field temperatures do not change during gas production.
[e]Temperature calculations at the phase boundary use the bulk hydrate phase boundary and assume that the field pressure does not change during gas production.
[f]References are as follows: a, (Uchida et al. 2000); b, (Kulenkampff and Spangenberg 2005); c, (Bily and Dick 1974); d, (Matsumoto et al. 2000); e, (Collett and Wendlandt 2000); f, (Ruppel 1997); g, (Winters 2000); h, (Winters 1995); i, (Uchida et al. 2004); j, (Yamano et al. 1982); k, (Taira et al. 1991); l, (Yun et al. 2010); m, (Collett et al. 2008); n, (Mandal et al. 2014); o, (Kumar et al. 2014); p, (Winters et al. 2008); q, (Hovland et al. 1995); r, (Camerlenghi et al. 1995); s, (Westbrook et al. 1994); t, (von Huene et al. 1987); u, (Kvenvolden and Kastner 1990); v, (Hill and Marsters 1990); w, (Tamaki et al. 1990); x, (Holler 1992); y, (Lee et al. 2011); z, (Kim et al. 2011); aa, (Kwon et al. 2011); ab, (Pflaum et al. 1986); ac, (Thayer et al. 1986); ad, (Bryant et al. 1986); ae, (Milkov and Sassen 2001); af, (Boswell et al. 2009); ag, (Luan et al. 2008); ah, (Dang et al. 2010); ai, (Stern et al. 2011); aj, (Winters et al. 2011); ak, (Hunter et al. 2011); al, (Dai et al. 2011); am, (Yun et al. 2006); an, (Tan et al. 2006); ao, (Liu and Flemings 2006); ap, (Milkov 2004).

Figure 6.1 Coarse and fine-grained particles while the fine mass fraction is small in this sketch. Fines determine the pore size, capillary behavior, electrical sensitivity to pore fluid charges and fluid flow.

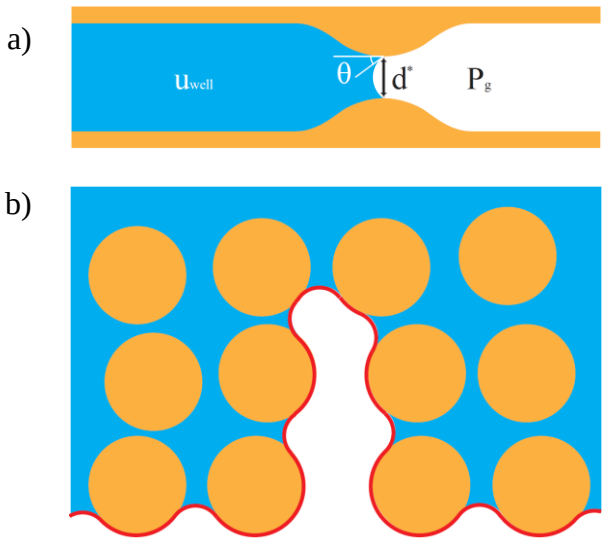

Figure 6.2 Particle level mechanical equilibrium. a) Capillary pressure between gas and water. b) Equilibrium involves skeletal forces (effective stress), water pressure and gas pressure.

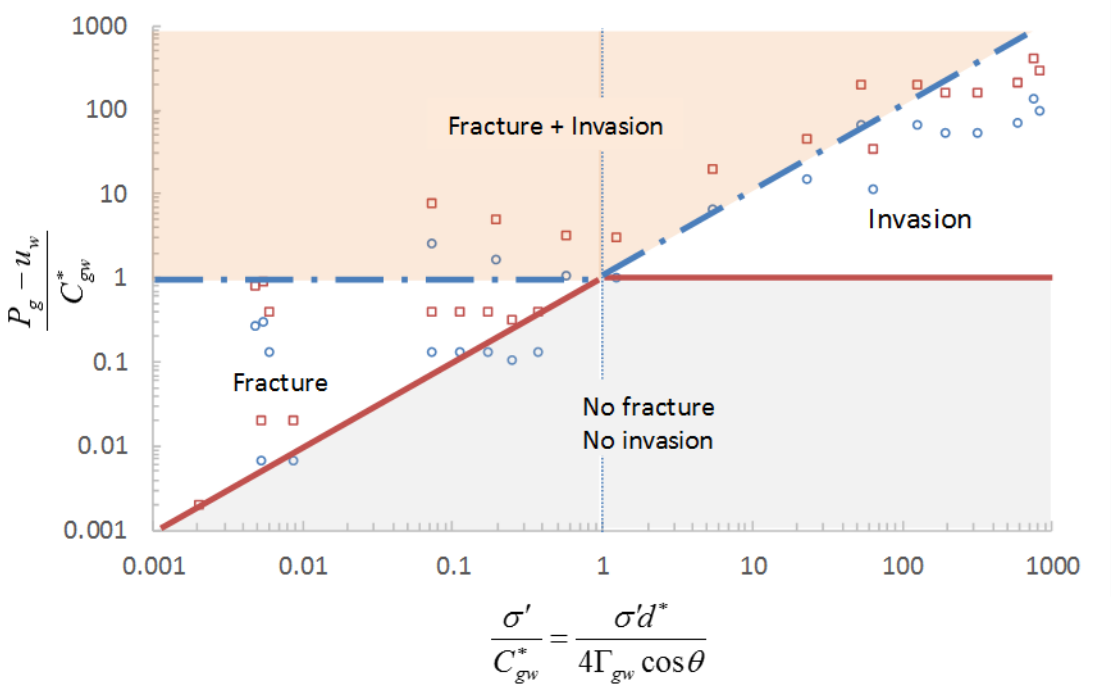

Figure 6.3 Balance between the effective stress σ', characteristic capillary pressure C^*_{gw} and the pressure difference between the gas and water P_g-u_w. Different regions inferred from equilibrium conditions. Dots represent different site conditions (Table 6.1). We assume the pressure difference for all the sites is either 1MPa (○) or 3MPa (□).

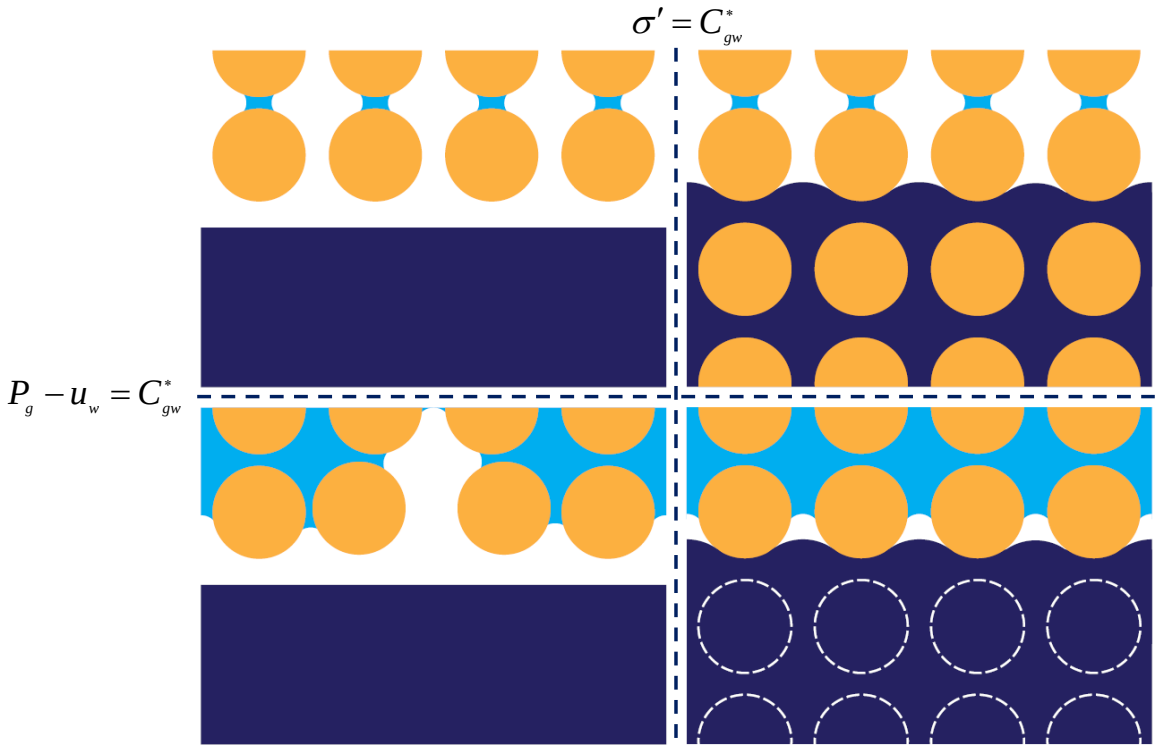

Figure 6.4 Particle-scale distribution of hydrate (dark purple), water (blue), gas (white) and particles (particles) during gas production. a) Y3 and Y4; b) Y2; c) Y1; d) N1 and N2.

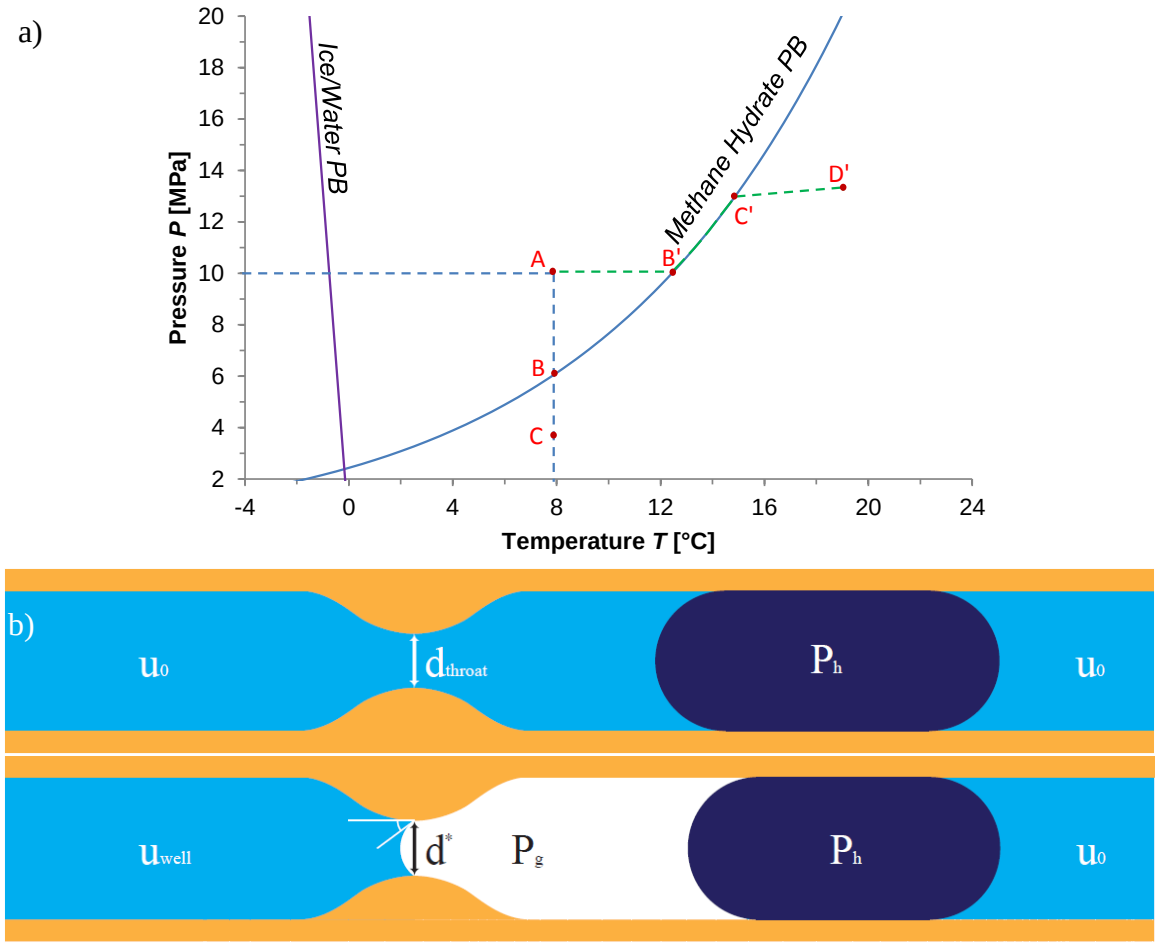

Figure 6.5 Depressurization ABC and thermal stimulation AB'C'D'. a) PT trajectories. b) Capillary pressure between gas and water in the presense of hydrate.

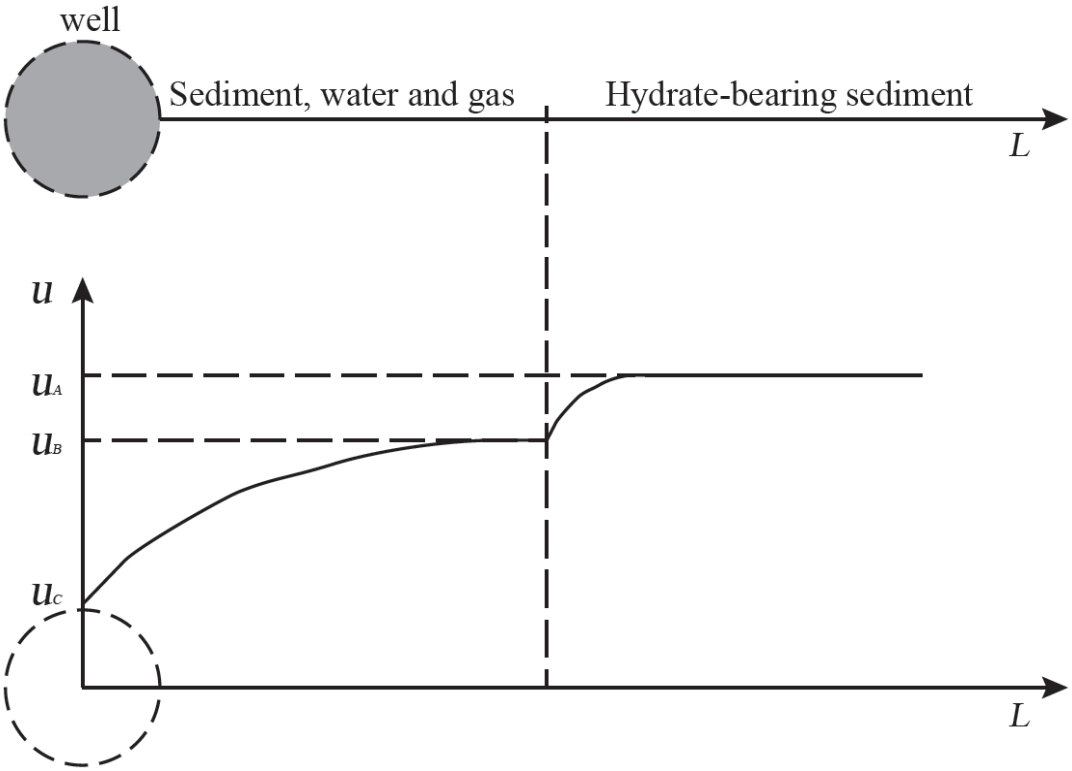

Figure 6.6 Depressurization driven gas production from hydrate-bearing sediments. Pressures u_A, u_B and u_C correspond to the fluid pressure at points A, B and C in Figure 6.5a.

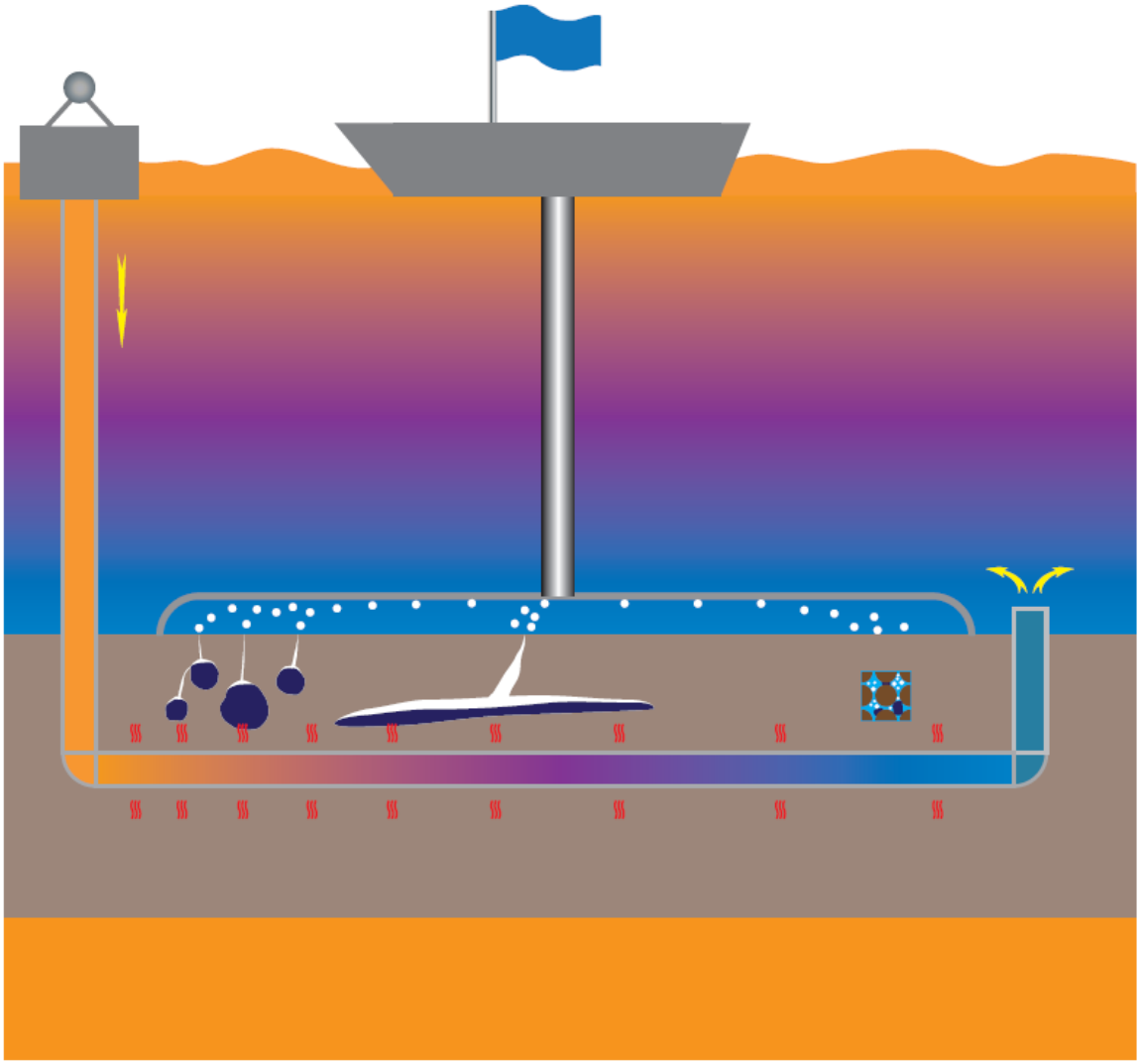

Figure 6.7 Gas production by thermal stimulation complemented with umbrella capture.

CHAPTER 7

CONCLUSIONS

The total amount of carbon trapped in gas hydrate reservoirs exceeds the sum of conventional oil, coal and gas resources. Fine-grained sediments host the majority of the world's total hydrate. However, gas hydrates in fine-grained sediments remain highly unexplored in comparison to coarse-grained sediments. The aims of this research were to increase the knowledge base of hydrate formation and dissociation in fine-grained sediments, to develop laboratory techniques to emulate natural hydrate formation in fine-grained sediments, to predict the physical properties of hydrate-bearing fine-grained sediments using numerical simulations and analytical tools and to explore gas production alternatives to recover methane from fine-grained sediments. The main conclusions generated from this research follow.

Hydrate formation in fine-grained sediments.

Gas hydrate formation from dissolved gas is inherently gas limited. Furthermore, small pores in fine-grained sediments and the finite space in small pores inhibits hydrate nucleation due to the limited amount of dissolved gas present in a single pore.

In addition, small pores result in a low hydraulic conductivity and high capillary effect. Low hydraulic conductivity limits the gas supply to the hydrate formation front to diffusive transport. The capillary effect between hydrate and water influences both the chemical and mechanical balance between hydrate mass and the environment. The chemical consequence of the capillary effect is that hydrates with curved surfaces are in a relatively unstable state in comparison to hydrates with flat surfaces. Therefore, stable hydrate with curved surfaces demands relatively higher pressure, lower temperature or larger gas concentration in pore fluids.

A hydrate mass with curved surfaces experiences higher pressure than the surrounding water. This unbalanced pressure reacts on the soil skeleton. Consequently,

hydrate formation consolidates the sediments due to cryogenic suction. When the capillary pressure exceeds the effective stress, hydrate mass displaces soil particles and exhibit a segregated morphology.

Note that the chemical balance is consistent with the mechanical balance. Large effective stress and small pores could prevent hydrate formation without sufficient temperature depression.

The capillary effect between water and gas could generate gas-driven openings in the sediments. Consequently, methane supply to the hydrate formation front could be either through diffusion dominated dissolved methane transport or through gas-driven openings. Hydrate formation by diffusion-controlled methane supply can exhibit Liesegang bands. Hydrate formation in gas-filled openings exhibits two patterns: a hydrate shell along gas-sediments interface and an exo-pore pattern.

Laboratory hydrate formation in fine-grained sediments.

Hydrate formation in fine-grained sediments is subject to the limitation in nucleation, the capillary effect and the slow supply rate of guest molecules. Sufficient temperature depression overcomes capillary effects. Therefore, laboratory experiments focus on the exploration of different strategies to accelerate the guest molecule supply to the gas hydrate formation front. These strategies include the use of THF as guest molecules, the selection of intra-porous diatoms for local gas storage, and gas injection directly into the sediments. In addition, we use long-term experiments to study diffusion-controlled hydrate formation and ice-hydrate transformation experiments for controlled nucleation topology. Experimental results reveal:

- If it was not for the fact that we have seen hydrates in fine-grained sediments, we would have long ago given up on trying to form hydrate in the lab.
- Gas hydrate can form in fine-grained sediments in laboratory conditions with appropriate strategies to guarantee continuous contact between gas and water, although it is challenging and slow in fine-grained sediments.

- Freshly formed hydrate with large quantities in fine-grained sediments is highly porous.
- Gas driven fractures relax the compression at the opening tip, increase the local void ratio and facilitate hydrate invasion into the sediments.
- The formed hydrate accumulations do not inherit the original morphology of the ice in ice-hydrate transformation experiments: hydrate grows around the first nuclei on the surface of ice lenses and combines supplied gas with extracted water around the nuclei.

Physical properties of hydrate-bearing fine-grained sediments.

Laboratory and in-situ measurements of physical properties require devices and protocols under high-pressure and low-temperature conditions. In addition, the mismatch between the measurements scale and the representative specimen size could result in biased results. Therefore, theoretical models and numerical experiments are critical in the estimation of the physical properties of hydrate-bearing fine-grained sediments.

The segregated hydrate morphology in fine-grained sediments results in a hydrate distribution that does not agree with geometrical assumptions in effective medium theories.

Cryogenic suction during hydrate formation over consolidates the sediments and alters their physical properties.

Numerical simulations in this research consider both hydrate morphology and cryogenic suction. The strength analyses of hydrate-bearing sediments use frictional and non-slip interfaces between hydrates and sediments. These two interfaces correspond to stable hydrate-sediment conditions and dissociation state respectively.

Simulation results in this study show.

- Laplacian field controlled physical properties (K_T, K_{hyd}) and the bulk modulus of lens-structured hydrate-bearing sediments do not fall within Hashin-Shtrikman bounds.

- The strength of stable hydrate-bearing fine-grained sediments increases due to the contribution of cryogenic suction and consolidation and the relatively high strength of the hydrate mass.
- The strength of hydrate-bearing sediments during gas production dramatically decreases when slippage occurs along the gas-filled hydrate-sediment interface.

Hydrate dissociation and gas production from fine-grained sediments.

Capillarity plays a critical role in gas production from fine-grained sediments.

- Gas production in fine-grained sediments that use conventional well techniques is not technically viable.
- Chemical stimulation and CO_2-CH_4 replacement in fine-grained sediments are inefficient and uneconomical.
- Surface mining in shallow sediments combined with thermal stimulation is a potential method to produce gas from fine-grained hydrate-bearing sediments.

REFERENCES

Adamson, A., and Gast, A. (1997). "The solid–liquid interface-contact angle." *Physical chemistry of surfaces*, 4, 333-361.

Adamson, A. W., and Gast, A. P. (1967). "Physical chemistry of surfaces."

Alikarami, R., Andò, E., Gkiousas-Kapnisis, M., Torabi, A., and Viggiani, G. (2015). "Strain localisation and grain breakage in sand under shearing at high mean stress: insights from in situ X-ray tomography." *Acta Geotech.*, 10(1), 15-30.

Alonso, E., and Ramon, A. (2013). "Heave of a railway bridge induced by gypsum crystal growth: field observations." *Géotechnique*, 63(9), 707.

Alshibli, K., Cil, M. B., Kenesei, P., and Lienert, U. (2013). "Strain tensor determination of compressed individual silica sand particles using high-energy synchrotron diffraction." *Granular matter*, 15(5), 517-530.

Alshibli, K. A., Batiste, S. N., Swanson, R. A., Sture, S., Costes, N. C., and Lankton, M. R. (1999). "Quantifying void ratio variation in sand using computed tomography."

Alshibli, K. A., and Sture, S. (1999). "Sand shear band thickness measurements by digital imaging techniques." *Journal of computing in civil engineering*, 13(2), 103-109.

Alvarez, R. E., and Macovski, A. (1976). "Energy-selective reconstructions in x-ray computerised tomography." *Phys. Med. Biol.*, 21(5), 733.

Anderson, G. K. (2003). "Enthalpy of dissociation and hydration number of carbon dioxide hydrate from the Clapeyron equation." *The Journal of Chemical Thermodynamics*, 35(7), 1171-1183.

Anderson, G. K. (2004). "Enthalpy of dissociation and hydration number of methane hydrate from the Clapeyron equation." *The Journal of Chemical Thermodynamics*, 36(12), 1119-1127.

Anderson, R., Tohidi, B., and Webber, J. B. W. (2009). "Gas hydrate growth and dissociation in narrow pore networks: capillary inhibition and hysteresis phenomena." *Geological Society, London, Special Publications*, 319(1), 145-159.

Anderson, S., Peyton, R., and Gantzer, C. (1990). "Evaluation of constructed and natural soil macropores using X-ray computed tomography." *Geoderma*, 46(1-3), 13-29.

Anderson, S. H., and Gantzer, C. J. (1989). "Determination of soil water content by X-ray computed tomography and magnetic resonance imaging." *Irrigation Science*, 10(1), 63-71.

Ando, E., Hall, S. A., Viggiani, G., Desrues, J., and Bésuelle, P. (2012). "Grain-scale experimental investigation of localised deformation in sand: a discrete particle tracking approach." *Acta Geotech.*, 7(1), 1-13.

Archer, D. (2007). "Methane hydrate stability and anthropogenic climate change." *Biogeosciences Discussions*, 4(2), 993-1057.

Baez, L. A., and Clancy, P. (1994). "Computer Simulation of the Crystal Growth and Dissolution of Natural Gas Hydratesa." *Ann. N. Y. Acad. Sci.*, 715(1), 177-186.

Baker, S. R., and Friedman, G. M. (1969). "A non-destructive core analysis technique using X-rays." *Journal of Sedimentary Research*, 39(4).

Berger, M. J., Hubbell, J.H., Seltzer, S.M., Chang, J., Coursey, J.S., Sukumar, R., Zucker, D.S., and Olsen, K. (2010). "XCOM: Photon Cross Section Database (version 1.5)." National Institute of Standards and Technology.

Berryman, J. G. (1980). "Long-wavelength propagation in composite elastic media I. Spherical inclusions." *The Journal of the Acoustical Society of America*, 68(6), 1809-1819.

Berryman, J. G. (1980). "Long-wavelength propagation in composite elastic media II. Ellipsoidal inclusions." *The Journal of the Acoustical Society of America*, 68(6), 1820-1831.

Berryman, J. G. (1995). "Mixture theories for rock properties." *Rock physics & phase relations: A handbook of physical constants*, 205-228.

Berryman, J. G., and Berge, P. A. (1996). "Critique of two explicit schemes for estimating elastic properties of multiphase composites." *Mechanics of Materials*, 22(2), 149-164.

Bertels, S. P., DiCarlo, D. A., and Blunt, M. J. (2001). "Measurement of aperture distribution, capillary pressure, relative permeability, and in situ saturation in a rock fracture using computed tomography scanning." *Water Resources Research*, 37(3), 649-662.

Bily, C., and Dick, J. (1974). "Naturally occurring gas hydrates in the Mackenzie Delta, NWT." *Bulletin of Canadian Petroleum Geology*, 22(3), 340-352.

Bloom, M., Russell, M. J., Kustau, A., Mandayam, S., and Sukumaran, B. (2010). "Measurement of Porosity in Granular Particle Distributions Using Adaptive Thresholding." *IEEE Transactions on Instrumentation and Measurement*, 59(5), 1192-1199.

Boswell, R. (2009). "Is Gas Hydrate Energy Within Reach?" *Science*, 325(5943), 957-958.

Boswell, R., and Collett, T. (2006). "The Gas Hydrates Resource Pyramid." *Fire in the Ice*, 1-4.

Boswell, R., Collett, T., Dallimore, S., and Frye, M. (2012). "Geohazards Associated with Naturally-Occurring Gas Hydrate." *Fire-In-The-Ice Methane Hydrate Newsletter*, 12(1), 1.

Boswell, R., and Collett, T. S. (2011). "Current perspectives on gas hydrate resources." *Energy & environmental science*, 4(4), 1206-1215.

Boswell, R., Kleinberg, R., Collett, T., and Frye, M. (2007). "Exploration priorities for marine gas hydrate resources." *Fire in the Ice: Methane hydrate newsletter*, 7(2), 11-13.

Boswell, R., Shelander, D., Lee, M., Latham, T., Collett, T., Guerin, G., Moridis, G., Reagan, M., and Goldberg, D. (2009). "Occurrence of gas hydrate in Oligocene Frio sand: Alaminos Canyon Block 818: Northern Gulf of Mexico." *Marine and Petroleum Geology*, 26(8), 1499-1512.

Bouma, A. H. (1964). "Notes on X-ray interpretation of marine sediments." *Marine geology*, 2(4), 278-309.

Bowden, F., and Hughes, T. "The mechanism of sliding on ice and snow." *Proc., Proceedings of the Royal Society of London A: Mathematical, Physical and Engineering Sciences*, The Royal Society, 280-298.

Bryant, W., Wetzel, A., and Sweet, W. (1986). "Geotechnical properties of intraslope basin sediments, Gulf of Mexico, deep-sea-drilling-project Leg-96, site 619." *Initial Rep Deep Sea*, 96, 819-824.

Calvert, S., and Veevers, J. (1962). "Minor structures of unconsolidated marine sediments revealed by X-radiography." *Sedimentology*, 1(4), 287-295.

Camerlenghi, A., Lucchi, R., and Rothwell, R. "Grain-size analysis and distribution in Cascadia Margin sediments, northeastern Pacific." *Proc., Proceedings-Ocean drilling program scienfitic results*, National Science Foundation 3-32.

Chalmers, G. (2005). "Structural Shielding Design for Medical Imaging X-ray Facilities (NCRP Report No 147)." IOP Publishing.

Chand, S., Minshull, T. A., Gei, D., and Carcione, J. M. (2004). "Elastic velocity models for gas-hydrate-bearing sediments—A comparison." *Geophysical Journal International*, 159(2), 573-590.

Charalampidou, E.-M., Hall, S. A., Stanchits, S., Lewis, H., and Viggiani, G. (2011). "Characterization of shear and compaction bands in a porous sandstone deformed under triaxial compression." *Tectonophysics*, 503(1), 8-17.

Charalampidou, E., Hall, S., Stanchits, S., Lewis, H., and Viggiani, G. "Characterization of shear and compaction bands in sandstone using X-ray tomography and digital image analysis." *Proc., Proceedings of the 3rd International Workshop on X-Ray CT for Geomaterials, GEOX*, 59-66.

Chen, H., and Grey, C. P. (2008). "Molten Salt Synthesis and High Rate Performance of the "Desert-Rose" form of LiCoO2." *Advanced Materials*, 20(11), 2206-2210.

Cho, Y., Moseley, D. J., Siewerdsen, J. H., and Jaffray, D. A. (2005). "Accurate technique for complete geometric calibration of cone-beam computed tomography systems." *Med. Phys.*, 32(4), 968-983.

Chong, S.-H., and Santamarina, J. C. (2016). "Soil Compressibility Models for a Wide Stress Range." *Journal of Geotechnical and Geoenvironmental Engineering*, 142(6), 06016003.

Clennell, M. B., Hovland, M., Booth, J. S., Henry, P., and Winters, W. J. (1999). "Formation of natural gas hydrates in marine sediments: 1. Conceptual model of gas hydrate growth conditioned by host sediment properties." *Journal of Geophysical Research: Solid Earth*, 104(B10), 22985-23003.

Coles, M., Hazlett, R., Spanne, P., Soll, W., Muegge, E., and Jones, K. (1998). "Pore level imaging of fluid transport using synchrotron X-ray microtomography." *Journal of Petroleum Science and Engineering*, 19(1), 55-63.

Collett, T. S. (2002). "Energy resource potential of natural gas hydrates." *AAPG bulletin*, 86(11), 1971-1992.

Collett, T. S., Riedel, M., Cochran, J. R., Boswell, R., Kumar, P., and Sathe, A. (2008). "Indian continental margin gas hydrate prospects: results of the Indian National Gas Hydrate Program (NGHP) expedition 01."

Collett, T. S., and Wendlandt, R. F. "Formation evaluation of gas hydrate-bearing marine sediments on the Blake Ridge with downhole geochemical log measurements." *Proc., Proceedings of the Ocean Drilling Program, Scientific Results*, 199-215.

Compton, A. H., and Allison, S. K. (1935). "X-rays in Theory and Experiment."

Cook, A. E., Goldberg, D., and Kleinberg, R. L. (2008). "Fracture-controlled gas hydrate systems in the northern Gulf of Mexico." *Marine and Petroleum Geology*, 25(9), 932-941.

Correns, C. W., and Steinborn, W. (1939). "Experimente zur Messung und Erklärung der sogenannten Kristallisationskraft." *Zeitschrift für Kristallographie-Crystalline Materials*, 101(1-6), 117-133.

Cussler, E. L. (2009). *Diffusion: mass transfer in fluid systems*, Cambridge university press.

Dai, S., Lee, C., and Carlos Santamarina, J. (2011). "Formation history and physical properties of sediments from the Mount Elbert Gas Hydrate Stratigraphic Test Well, Alaska North Slope." *Marine and Petroleum Geology*, 28(2), 427-438.

Dai, S., Santamarina, J. C., Waite, W. F., and Kneafsey, T. J. (2012). "Hydrate morphology: Physical properties of sands with patchy hydrate saturation." *Journal of Geophysical Research: Solid Earth*, 117(B11), B11205.

Dallimore, S., Yamamoto, K., Wright, J., and Bellefleur, G. (2012). *Scientific results from the JOGMEC/NRCan/Aurora Mallik 2007-2008 Gas Hydrate Production Research Well Program, Mackenzie Delta, Northwest Territories, Canada*.

Dang, H., Luan, X.-W., Chen, R., Zhang, X., Guo, L., and Klotz, M. G. (2010). "Diversity, abundance and distribution of amoA-encoding archaea in deep-sea methane seep sediments of the Okhotsk Sea." *FEMS microbiology ecology*, 72(3), 370-385.

Dash, J., Fu, H., and Wettlaufer, J. (1995). "The premelting of ice and its environmental consequences." *Reports on Progress in Physics*, 58(1), 115.

Desrues, J. (2004). "Tracking strain localization in geomaterials using computerized tomography." *X-ray CT for Geomaterials*, 15-41.

Durham, W. B., Kirby, S. H., Stern, L. A., and Zhang, W. (2003). "The strength and rheology of methane clathrate hydrate." *Journal of Geophysical Research: Solid Earth*, 108(B4).

Ebinuma, T., Kamata, Y., Minagawa, H., Ohmura, R., Nagao, J., and Narita, H. "Mechanical Properties of Sandy Sediment Containing Methane Hydrate." *Proc., Fifth International Conference on Gas Hydrates*, 958-961.

Espinoza, D. N., and Santamarina, J. C. (2010). "Water-CO2-mineral systems: Interfacial tension, contact angle, and diffusion—Implications to CO2 geological storage." *Water Resources Research*, 46(7), W07537.

Feldkamp, L., Davis, L., and Kress, J. (1984). "Practical cone-beam algorithm." *JOSA A*, 1(6), 612-619.

Fetter, C. W., and Fetter, C. (1999). *Contaminant hydrogeology*, Prentice hall New Jersey.

Fletcher, N. (1958). "Size effect in heterogeneous nucleation." *The Journal of chemical physics*, 29(3), 572-576.

Food, U., and Administration, D. (2015). "CFR-code of federal regulations title 21." *Current good manufacturing practice for finished pharmaceuticals Part*, 211.

Fukahori, D., Saito, Y., Morinaga, D., Ogata, M., and Sugawara, K. (2010). "Study on Water Flow in Rock by Means of the Tracer-aided X-rays CT." *Advances in X-ray Tomography for Geomaterials*, 285-292.

Fukahori, D., Sato, A., and Sugawara, K. (2006). "Development of a new X-ray CT permeation test system and application to porous rocks." *Proceedings of 2006 GeoCongress*.

Gardner, J. V., Malik, M., and Walker, S. (2009). "Plume 1400 Meters High Discovered at the Seafloor off the Northern California Margin." *Eos, Transactions American Geophysical Union*, 90(32), 275-275.

Ghosh, R., Sain, K., and Ojha, M. (2010). "Effective medium modeling of gas hydrate-filled fractures using the sonic log in the Krishna-Godavari basin, offshore eastern India." *Journal of Geophysical Research: Solid Earth*, 115(B6), B06101.

Gluyas, J., and Swarbrick, R. (2013). *Petroleum geoscience*, John Wiley & Sons.

Grass, M., Köhler, T., and Proksa, R. (2000). "3D cone-beam CT reconstruction for circular trajectories." *Phys. Med. Biol.*, 45(2), 329.

Grozic, J. (2010). "Interplay between gas hydrates and submarine slope failure." *Submarine mass movements and their consequences*, Springer, 11-30.

Hall, S. A., Wright, J., Pirling, T., Andò, E., Hughes, D. J., and Viggiani, G. (2011). "Can intergranular force transmission be identified in sand?" *Granular Matter*, 13(3), 251-254.

Hamblin, W. K. (1962). "X-ray radiography in the study of structures in homogeneous sediments." *Journal of Sedimentary Research*, 32(2).

Handa, Y. P., and Stupin, D. Y. (1992). "Thermodynamic properties and dissociation characteristics of methane and propane hydrates in 70-.ANG.-radius silica gel pores." *The Journal of Physical Chemistry*, 96(21), 8599-8603.

Hashemi, H., Javanmardi, J., Zarifi, M., Eslamimanesh, A., and Mohammadi, A. H. (2012). "Experimental study and thermodynamic modelling of methane clathrate hydrate dissociation conditions in silica gel porous media in the presence of methanol aqueous solution." *The Journal of Chemical Thermodynamics*, 49, 7-13.

Hashin, Z., and Shtrikman, S. (1962). "A Variational Approach to the Theory of the Effective Magnetic Permeability of Multiphase Materials." *Journal of Applied Physics*, 33(10), 3125-3131.

Hashin, Z., and Shtrikman, S. (1963). "A variational approach to the theory of the elastic behaviour of multiphase materials." *Journal of the Mechanics and Physics of Solids*, 11(2), 127-140.

Hauk, V. (1997). *Structural and residual stress analysis by nondestructive methods: Evaluation-Application-Assessment*, Elsevier.

Helgerud, M., Waite, W. F., Kirby, S., and Nur, A. (2009). "Elastic wave speeds and moduli in polycrystalline ice Ih, sI methane hydrate, and sII methane-ethane hydrate." *Journal of Geophysical Research: Solid Earth*, 114(B2).

Henry, P., Thomas, M., and Clennell, M. B. (1999). "Formation of natural gas hydrates in marine sediments: 2. Thermodynamic calculations of stability conditions in porous sediments." *Journal of Geophysical Research: Solid Earth*, 104(B10), 23005-23022.

Hill, P., and Marsters, J. "Controls on physical properties of Peru continental margin sediments and their relationship to deformation styles." *Proc., Suess, E., von Huene, R., et al., Proc. ODP, Sci. Results*, 623-632.

Hill, R. (1952). "The elastic behaviour of a crystalline aggregate." *Proceedings of the Physical Society. Section A*, 65(5), 349.

Hillig, W. B. (1998). "Measurement of interfacial free energy for ice/water system." *Journal of Crystal Growth*, 183(3), 463-468.

Hofmann, D., Preuss, G., and Mätzler, C. (2015). "Evidence for biological shaping of hair ice." *Biogeosciences*, 12(14), 4261-4273.

Holler, P. R. "Consolidation characteristics and permeabilities of sediments from Japan Sea (Sites 798 and 799)." *Proc., Proc. Ocean Drill. Program Sci. Results, 127*, 1123-1133.

Hornbach, M. J., Lavier, L. L., and Ruppel, C. D. (2007). "Triggering mechanism and tsunamogenic potential of the Cape Fear Slide complex, US Atlantic margin." *Geochemistry, Geophysics, Geosystems*, 8(12).

Hovland, M., Lysne, D., and Whiticar, M. "Gas hydrate and sediment gas composition, hole 892A1." *Proc., Proceedings of the Ocean Drilling Program, Scientific Results*.

Huang, D., and Fan, S. (2005). "Measuring and modeling thermal conductivity of gas hydrate-bearing sand." *Journal of Geophysical Research: Solid Earth*, 110(B1), n/a-n/a.

Hunter, R. B., Collett, T. S., Boswell, R., Anderson, B. J., Digert, S. A., Pospisil, G., Baker, R., and Weeks, M. (2011). "Mount Elbert gas hydrate stratigraphic test well, Alaska North Slope: Overview of scientific and technical program." *Marine and Petroleum Geology*, 28(2), 295-310.

Huysmans, M., and Dassargues, A. (2005). "Review of the use of Péclet numbers to determine the relative importance of advection and diffusion in low permeability environments." *Hydrogeol J*, 13(5-6), 895-904.

Ionita, C. N., Hoffmann, K. R., Bednarek, D. R., Chityala, R., and Rudin, S. (2008). "Cone-beam micro-CT system based on LabVIEW software." *J. Digit. Imaging*, 21(3), 296-305.

Jaeger, R. G. (1968). *Engineering Compendium on Radiation Shielding: Shielding Fundamentals and Methods*, Springer-Verlag.

Jang, J., and Santamarina, J. C. (2016). "Hydrate bearing clayey sediments: Formation and gas production concepts." *Marine and Petroleum Geology*, 77, 235-246.

Jin, Y., Nagao, J., Hayashi, J., Shimada, W., Ebinuma, T., and Narita, H. (2008). "Observation of Xe Hydrate Growth at Gas−Ice Interface by Microfocus X-ray Computed Tomography." *The Journal of Physical Chemistry C*, 112(44), 17253-17256.

Johnston, S. M., Johnson, G. A., and Badeaa, C. T. (2008). "Geometric calibration for a dual tube/detector micro-CT system." *Med. Phys.*, 35(5), 1820-1829.

Kak, A. C., and Slaney, M. (1988). *Principles of computerized tomographic imaging*, IEEE press.

Kalender, W. A. (2006). "X-ray computed tomography." *Phys. Med. Biol.*, 51(13), R29.

Kashchiev, D., and Firoozabadi, A. (2002). "Nucleation of gas hydrates." *Journal of crystal growth*, 243(3), 476-489.

Katsuki, D., Ohmura, R., Ebinuma, T., and Narita, H. (2006). "Formation, growth and ageing of clathrate hydrate crystals in a porous medium." *Philosophical Magazine*, 86(12), 1753-1761.

Kawamoto, R., Andò, E., Viggiani, G., and Andrade, J. E. (2016). "Level set discrete element method for three-dimensional computations with triaxial case study." *Journal of the Mechanics and Physics of Solids*, 91, 1-13.

Kim, G. Y., Yi, B. Y., Yoo, D. G., Ryu, B. J., and Riedel, M. (2011). "Evidence of gas hydrate from downhole logging data in the Ulleung Basin, East Sea." *Marine and Petroleum Geology*, 28(10), 1979-1985.

Kim, Y., Ryu, S., Yang, S., and Lee, C. (2003). "Liquid water-hydrate equilibrium measurements and unified predictions of hydrate-containing phase equilibria for methane, ethane, propane, and their mixtures." *Ind. Eng. Chem. Res.*, 42(11), 2409-2414.

Konrad, O., and Lankau, T. (2005). "Solubility of Methane in Water: The Significance of the Methane−Water Interaction Potential." *The Journal of Physical Chemistry B*, 109(49), 23596-23604.

Kulenkampff, J., and Spangenberg, E. (2005). "Physical properties of cores from the JAPEX/JNOC/GSC et al. Mallik 5L-38 gas hydrate production research well under simulated in situ conditions using the field laboratory experimental core analysis system (FLECAS)." *Bulletin-Geological Survey of Canada*, 585, 87.

Kumar, A., Maini, B., Bishnoi, P., Clarke, M., Zatsepina, O., and Srinivasan, S. (2010). "Experimental determination of permeability in the presence of hydrates and its effect on the dissociation characteristics of gas hydrates in porous media." *Journal of Petroleum Science and Engineering*, 70(1), 114-122.

Kumar, P., Collett, T. S., Boswell, R., Cochran, J. R., Lall, M., Mazumdar, A., Ramana, M. V., Ramprasad, T., Riedel, M., and Sain, K. (2014). "Geologic implications of gas hydrates in the offshore of India: Krishna–Godavari Basin, Mahanadi Basin, Andaman Sea, Kerala–Konkan Basin." *Marine and Petroleum Geology*, 58, 29-98.

Kuster, G. T., and Toksöz, M. N. (1974). "Velocity and attenuation of seismic waves in two-phase media: Part I. Theoretical formulations." *Geophysics*, 39(5), 587-606.

Kvalstad, T. J., Andresen, L., Forsberg, C. F., Berg, K., Bryn, P., and Wangen, M. (2005). "The Storegga slide: evaluation of triggering sources and slide mechanics." *Marine and Petroleum Geology*, 22(1), 245-256.

Kvenvolden, K. A. (1988). "Methane Hydrate - a Major Reservoir of Carbon in the Shallow Geosphere." *Chemical Geology*, 71(1-3), 41-51.

Kvenvolden, K. A., and Kastner, M. (1990). "Gas hydrates of the peruvian outer continental margin."

Kwon, T.-H., Cho, G.-C., and Santamarina, J. C. (2008). "Gas hydrate dissociation in sediments: Pressure-temperature evolution." *Geochemistry, Geophysics, Geosystems*, 9(3), Q03019.

Kwon, T.-H., Lee, K.-R., Cho, G.-C., and Lee, J. Y. (2011). "Geotechnical properties of deep oceanic sediments recovered from the hydrate occurrence regions in the Ulleung Basin, East Sea, offshore Korea." *Marine and Petroleum Geology*, 28(10), 1870-1883.

Lee, C., Yun, T. S., Lee, J.-S., Bahk, J. J., and Santamarina, J. C. (2011). "Geotechnical characterization of marine sediments in the Ulleung Basin, East Sea." *Engineering Geology*, 117(1), 151-158.

Lee, J., Yun, T., Santamarina, J., and Ruppel, C. (2007). "Observations related to tetrahydrofuran and methane hydrates for laboratory studies of hydrate-bearing sediments." *Geochemistry, Geophysics, Geosystems*, 8(6).

Lee, J. Y., Jung, J. W., Lee, M. H., Bahk, J. J., Choi, J., Ryu, B. J., and Schultheiss, P. (2013). "Pressure core based study of gas hydrates in the Ulleung Basin and implication for geomechanical controls on gas hydrate occurrence." *Marine and Petroleum Geology*, 47(0), 85-98.

Lee, J. Y., Yun, T. S., Santamarina, J. C., and Ruppel, C. (2007). "Observations related to tetrahydrofuran and methane hydrates for laboratory studies of hydrate-bearing sediments." *Geochemistry, Geophysics, Geosystems*, 8(6), Q06003.

Lee, M., and Collett, T. (2005). "Assessments of gas hydrate concentrations estimated from sonic logs in the JAPEX/JNOC/GSC et al. Mallik 5L-38 gas hydrate research production well." *Bulletin-Geological Survey of Canada*, 585, 118.

Lenoir, N., Marello, S., Viggiani, G., Bésuelle, P., Desrues, J., and Di Michiel, M. (2004). "X-ray micro tomography characterization of strain localization upon deviatoric loading of saturated fine-grained stiff soils." *X-ray CT for Geomaterials (GeoX2003), Balkema*, 147-155.

Lester, H., and Aborn, R. (1925). "Behaviour under stress of iron crystal in steel." *Army Ordnance*, 6, 120.

Li, L., Xing, Y., Chen, Z., Zhang, L., and Kang, K. (2011). "A curve-filtered FDK (C-FDK) reconstruction algorithm for circular cone-beam CT." *Journal of X-ray science and technology*, 19(3), 355-371.

Li, Y., and Somorjai, G. A. (2007). "Surface Premelting of Ice." *The Journal of Physical Chemistry C*, 111(27), 9631-9637.

Lim, K.-W., Kawamoto, R., Andò, E., Viggiani, G., and Andrade, J. E. (2016). "Multiscale characterization and modeling of granular materials through a computational mechanics avatar: a case study with experiment." *Acta Geotech.*, 11(2), 243-253.

Liu, X., and Flemings, P. B. (2006). "Passing gas through the hydrate stability zone at southern Hydrate Ridge, offshore Oregon." *Earth and Planetary Science Letters*, 241(1–2), 211-226.

Liu, X., and Flemings, P. B. (2011). "Capillary effects on hydrate stability in marine sediments." *Journal of Geophysical Research*, 116(B7), 0-Citation B07102.

Lu, W., Chou, I. M., and Burruss, R. C. (2008). "Determination of methane concentrations in water in equilibrium with sI methane hydrate in the absence of a vapor phase by in situ Raman spectroscopy." *Geochim. Cosmochim. Acta*, 72(2), 412-422.

Luan, X., Jin, Y., Obzhirov, A., and Yue, B. (2008). "Characteristics of shallow gas hydrate in Okhotsk Sea." *Science in China Series D: Earth Sciences*, 51(3), 415-421.

Makogon, I. U. F. (1997). *Hydrates of Hydrocarbons*, PennWell Books.

Mandal, R., Dewangan, P., Ramprasad, T., Kumar, B., and Vishwanath, K. (2014). "Effect of thermal non-equilibrium, seafloor topography and fluid advection on BSR-derived geothermal gradient." *Marine and Petroleum Geology*, 58, 368-381.

Masad, E., Saadeh, S., Al-Rousan, T., Garboczi, E., and Little, D. (2005). "Computations of particle surface characteristics using optical and X-ray CT images." *Computational Materials Science*, 34(4), 406-424.

Mason, B. J. (1971). *The Physics of Clouds*, Oxford, Clarendon Press.

Massoudi, R., and King, A. D. (1974). "Effect of pressure on the surface tension of water. Adsorption of low molecular weight gases on water at 25.deg." *The Journal of Physical Chemistry*, 78(22), 2262-2266.

Massoudi, R., and King Jr, A. (1974). "Effect of pressure on the surface tension of water. Adsorption of low molecular weight gases on water at 25. deg." *The Journal of Physical Chemistry*, 78(22), 2262-2266.

Matsumoto, R., Uchida, T., Waseda, A., Uchida, T., Takeya, S., Hirano, T., Yamada, K., Maeda, Y., and Okui, T. "2. Occurrence, structure, and composition of natural gas hydrate recovered from the Blake Ridge, Northwest Atlantic." *Proc., Proceedings of the Ocean Drilling Program. Scientific Results*, Ocean Drilling Program, 13-28.

Mavko, G., Mukerji, T., and Dvorkin, J. (2009). *The Rock Physics Handbook: Tools for Seismic Analysis of Porous Media*, Cambridge University Press.

McDonald, J. E. (1953). "Homogeneous nucleation of supercooled water drops." *Journal of Meteorology*, 10(6), 416-433.

Mengesha, W., and Valentine, J. (2002). "Benchmarking NaI (Tl) electron energy resolution measurements." *IEEE Trans. Nucl. Sci.*, 49(5), 2420-2426.

Merino, E. (1984). "Survey of geochemical self-patterning phenomena." *Chemical instabilities*, Springer, 305-328.

Milkov, A. V. (2004). "Global estimates of hydrate-bound gas in marine sediments: how much is really out there?" *Earth-Science Reviews*, 66(3), 183-197.

Milkov, A. V., and Sassen, R. (2001). "Estimate of gas hydrate resource, northwestern Gulf of Mexico continental slope." *Marine Geology*, 179(1), 71-83.

Montemagno, C., and Pyrak-Nolte, L. (1999). "Fracture network versus single fractures: measurement of fracture geometry with X-ray tomography." *Physics and Chemistry of the Earth, Part A: Solid Earth and Geodesy*, 24(7), 575-579.

Moridis, G. J. (2008). "Toward production from gas hydrates: current status, assessment of resources, and simulation-based evaluation of technology and potential." *Lawrence Berkeley National Laboratory*.

Moridis, G. J., Collett, T. S., Boswell, R., Kurihara, M., Reagan, M. T., Koh, C., and Sloan, E. D. (2009). "Toward Production From Gas Hydrates: Current Status, Assessment of Resources, and Simulation-Based Evaluation of Technology and Potential." *SPE Res Eval & Eng*, 12(5), 745-771.

Moridis, G. J., Kowalsky, M. B., and Pruess, K. (2007). "Depressurization-induced gas production from class-1 hydrate deposits." *SPE Reservoir Evaluation & Engineering*, 10(05), 458-481.

Myerson, A. (2002). *Handbook of Industrial Crystallization*, Butterworth-Heinemann.

Østergaard, K. K., Anderson, R., Llamedo, M., and Tohidi, B. (2002). "Hydrate phase equilibria in porous media: effect of pore size and salinity." *Terra Nova*, 14(5), 307-312.

Otani, J., and Obara, Y. (2004). *Xray CT for Geomaterials: Soils, Concrete, Rocks International Workshop on Xray CT for Geomaterials, Kumamoto, Japan*, CRC Press.

Palomino, A. M., and Santamarina, J. C. (2005). "Fabric map for kaolinite: effects of pH and ionic concentration on behavior." *Clays and Clay minerals*, 53(3), 211-223.

Panetta, D., Belcari, N., Del Guerra, A., and Moehrs, S. (2008). "An optimization-based method for geometrical calibration in cone-beam CT without dedicated phantoms." *Phys. Med. Biol.*, 53(14), 3841-3861.

Park, K.-P., Bahk, J.-J., Kwon, Y., Kim, G.-Y., Riedel, M., Holland, M., Schultheiss, P., and Rose, K. (2008). "Korean national Program expedition confirms rich gas hydrate deposit in the Ulleung Basin, East Sea." *Fire in the Ice: Methane Hydrate Newsletter*, 8(2), 6-9.

Paull, C. K., Matsumoto, R., J, W. P., and Party, L. S. *Proc., Proceedings, Ocean Drilling Program, Initial reports*, Ocean Drill. Program. College Station.

Paull, C. K., Ussler, W., Borowski, W. S., and Spiess, F. N. (1995). "Methane-rich plumes on the Carolina continental rise: Associations with gas hydrates." *Geology*, 23(1), 89-92.

Peyton, R., Haeffner, B., Anderson, S., and Gantzer, C. (1992). "Applying X-ray CT to measure macropore diameters in undisturbed soil cores." *Geoderma*, 53(3-4), 329-340.

Pflaum, R. C., Brooks, J. M., Cox, H. B., Kennicutt II, M. C., and Sheu, D.-D. (1986). "Molecular and isotopic analysis of core gases and gas hydrates, deep sea drilling project leg 961 ".

Plaschke, M., Schäfer, T., Bundschuh, T., Ngo Manh, T., Knopp, R., Geckeis, H., and Kim, J. (2001). "Size characterization of bentonite colloids by different methods." *Anal. Chem.*, 73(17), 4338-4347.

Prince, J. L., and Links, J. M. (2006). *Medical imaging signals and systems*, Pearson Prentice Hall Upper Saddle River, NJ.

Pyrak-Nolte, L. J., Montemagno, C. D., and Nolte, D. D. (1997). "Volumetric imaging of aperture distributions in connected fracture networks." *Geophys. Res. Lett.*, 24(18), 2343-2346.

Radhakrishnan, R., and Trout, B. L. (2002). "A new approach for studying nucleation phenomena using molecular simulations: Application to CO2 hydrate clathrates." *The Journal of Chemical Physics*, 117(4), 1786-1796.

Ramseier, R. O. (1967). "Self-Diffusion of Tritium in Natural and Synthetic Ice Monocrystals." *Journal of Applied Physics*, 38(6), 2553-2556.

Rangayyan, R. M. (2004). *Biomedical image analysis*, CRC press.

Rasband, W. (1997). "ImageJ software." *National Institutes of Health: Bethesda, MD, USA*, 2012.

Rebuffel, V., and Dinten, J.-M. (2007). "Dual-energy X-ray imaging: benefits and limits." *Insight-non-destructive testing and condition monitoring*, 49(10), 589-594.

Rees, E. V. L., Priest, J. A., and Clayton, C. R. I. (2011). "The structure of methane gas hydrate bearing sediments from the Krishna–Godavari Basin as seen from Micro-CT scanning." *Marine and Petroleum Geology*, 28(7), 1283-1293.

Remeysen, K., and Swennen, R. (2006). "Beam hardening artifact reduction in microfocus computed tomography for improved quantitative coal characterization." *International Journal of Coal Geology*, 67(1), 101-111.

Rempel, A. W. (2007). "Formation of ice lenses and frost heave." *Journal of Geophysical Research*, 112.

Rezvani, N., Aruliah, D., Jackson, K., Moseley, D., and Siewerdsen, J. (2007). "SU-FF-I-16: OSCaR: An Open-Source Cone-Beam CT Reconstruction Tool for Imaging Research." *Med. Phys.*, 34(6), 2341-2341.

Rit, S., Oliva, M. V., Brousmiche, S., Labarbe, R., Sarrut, D., and Sharp, G. C. "The Reconstruction Toolkit (RTK), an open-source cone-beam CT reconstruction toolkit based on the Insight Toolkit (ITK)." *Proc., Journal of Physics: Conference Series*, IOP Publishing, 012079.

Roscoe, K. H. (1970). "The influence of strains in soil mechanics." *Geotechnique*, 20(2), 129-170.

Rosenbaum, E. J., English, N. J., Johnson, J. K., Shaw, D. W., and Warzinski, R. P. (2007). "Thermal Conductivity of Methane Hydrate from Experiment and Molecular Simulation." *The Journal of Physical Chemistry B*, 111(46), 13194-13205.

Ruppel, C. (1997). "Anomalously cold temperatures observed at the base of the gas hydrate stability zone on the US Atlantic passive margin." *Geology*, 25(8), 699-702.

Ruppel, C., and Pohlman, J. (2008). "Climate change and the global carbon cycle: Perspectives and opportunities." *Fire in the Ice: Methane Hydrate Newsletter*, 8(1), 5-8.

Salvatore, E., Andò, E., Modoni, G., and Viggiani, G. (2016). "Micromechanical Study of Cyclically Loaded Sands with x-ray Microtomography and Digital Image Correlation." *Procedia Engineering*, 158, 92-97.

Scheel, M., Seemann, R., Brinkmann, M., Di Michiel, M., Sheppard, A., Breidenbach, B., and Herminghaus, S. (2008). "Morphological clues to wet granular pile stability." *Nature Materials*, 7(3), 189-193.

Scherer, G. W. (1999). "Crystallization in pores." *Cement and Concrete Research*, 29(8), 1347-1358.

Schnaar, G., and Brusseau, M. L. (2006). "Characterizing pore-scale configuration of organic immiscible liquid in multiphase systems with synchrotron X-ray microtomography." *Vadose Zone J.*, 5(2), 641-648.

Schoderbek, D., Farrell, H., Hester, K., Howard, J., Raterman, K., Silpngarmlert, S., Martin, K., Smith, B., and Klein, P. (2013). "ConocoPhillips gas hydrate production test final technical report." *United States Department of Energy*.

Selman, J., and Thomas, C. (1985). "The fundamentals of x-ray and radium physics."

Seo, Y., Lee, H., and Ryu, B. J. (2002). "Hydration number and two-phase equilibria of CH4 hydrate in the deep ocean sediments." *Geophys. Res. Lett.*, 29(8).

Servio, P., and Englezos, P. (2002). "Measurement of dissolved methane in water in equilibrium with its hydrate." *Journal of Chemical & Engineering Data*, 47(1), 87-90.

Seshadri, K., Wilder, J. W., and Smith, D. H. (2001). "Measurements of Equilibrium Pressures and Temperatures for Propane Hydrate in Silica Gels with Different Pore-Size Distributions." *The Journal of Physical Chemistry B*, 105(13), 2627-2631.

Shin, H., and Santamarina, J. C. (2011). "Open-mode discontinuities in soils." *Géotechnique Letters*, 95-99.

Sloan, E. D., and Koh, C. (2007). *Clathrate Hydrates of Natural Gases, Third Edition*, CRC Press.

Steiger, M. (2005). "Crystal growth in porous materials—I: The crystallization pressure of large crystals." *Journal of Crystal Growth*, 282(3–4), 455-469.

Stern, L. A., Lorenson, T. D., and Pinkston, J. C. (2011). "Gas hydrate characterization and grain-scale imaging of recovered cores from the Mount Elbert Gas Hydrate Stratigraphic Test Well, Alaska North Slope." *Marine and Petroleum Geology*, 28(2), 394-403.

Subramanian, S. (2000). "Measurement of Clathrate hydrates Containing Methane and Ethane Using Raman Spectroscopy." Doctoral, Colorado School of Mines, Glden, CO.

Suess, E., Torres, M., Bohrmann, G., Collier, R., Rickert, D., Goldfinger, C., Linke, P., Heuser, A., Sahling, H., and Heeschen, K. (2001). "Sea floor methane hydrates at Hydrate Ridge, Cascadia margin." *Natural gas hydrates: occurrence, distribution, and detection*, 87-98.

Sultan, N., Bohrmann, G., Ruffine, L., Pape, T., Riboulot, V., Colliat, J. L., De Prunelé, A., Dennielou, B., Garziglia, S., Himmler, T., Marsset, T., Peters, C. A., Rabiu, A., and Wei, J. (2014). "Pockmark formation and evolution in deep water Nigeria: Rapid hydrate growth versus slow hydrate dissolution." *Journal of Geophysical Research: Solid Earth*, 119(4), 2679-2694.

Sultan, N., Marsset, B., Ker, S., Marsset, T., Voisset, M., Vernant, A. M., Bayon, G., Cauquil, E., Adamy, J., Colliat, J. L., and Drapeau, D. (2010). "Hydrate dissolution as a potential mechanism for pockmark formation in the Niger delta." *Journal of Geophysical Research: Solid Earth*, 115(B8), n/a-n/a.

Sun, R., and Duan, Z. (2007). "An accurate model to predict the thermodynamic stability of methane hydrate and methane solubility in marine environments." *Chemical Geology*, 244(1–2), 248-262.

Taira, A., Hill, I., Firth, J. V., Berner, U., and Bruckmann, W. (1991). "Proceedings of the Ocean Drilling Program, Initial Reports."College Station, Tex, 71-269.

Tamaki, k., Pisciotto, K. A., and Allan, J. (1990). "Proceedings of the Ocean Drilling Program, Initial Reports."College Station, Tex.

Tan, B., Germaine, J., and Flemings, P. "Data report: Consolidation and strength characteristics of sediments from ODP Site 1244, Hydrate Ridge, Cascadia continental margin." *Proc., Proc. Ocean Drill. Program Sci. Results*, 1-148.

Taylor, C. J., Miller, K. T., Koh, C. A., and Sloan, E. D. (2007). "Macroscopic investigation of hydrate film growth at the hydrocarbon/water interface." *Chemical Engineering Science*, 62(23), 6524-6533.

Te Wu, T. (1966). "The effect of inclusion shape on the elastic moduli of a two-phase material." *International Journal of Solids and Structures*, 2(1), 1-8.

Thayer, P., Roberts, H., Bouma, A., and Coleman, J. (1986). "Sedimentology and petrology of mississippi fan depositional-environments, deep-sea-drilling-project leg 96." *Initial Rep Deep Sea*, 96, 489-503.

Thomson, W. (1872). "4. On the Equilibrium of Vapour at a Curved Surface of Liquid." *Proceedings of the Royal Society of Edinburgh*, 7, 63-68.

Tohidi, B., Anderson, R., Clennell, M. B., Burgass, R. W., and Biderkab, A. B. (2001). "Visual observation of gas-hydrate formation and dissociation in synthetic porous media by means of glass micromodels." *Geology*, 29(9), 867-870.

Uchida, T., Dallimore, S., and Mikami, J. (2000). "Occurrences of Natural Gas Hydrates beneath the Permafrost Zone in Mackenzie Delta: Visual and X-ray CT Imagery." *Ann. N. Y. Acad. Sci.*, 912(1), 1021-1033.

Uchida, T., Ebinuma, T., and Ishizaki, T. (1999). "Dissociation condition measurements of methane hydrate in confined small pores of porous glass." *The Journal of Physical Chemistry B*, 103(18), 3659-3662.

Uchida, T., Ebinuma, T., Kawabata, J. i., and Narita, H. (1999). "Microscopic observations of formation processes of clathrate-hydrate films at an interface between water and carbon dioxide." *Journal of crystal growth*, 204(3), 348-356.

Uchida, T., Ebinuma, T., Takeya, S., Nagao, J., and Narita, H. (2001). "Effects of Pore Sizes on Dissociation Temperatures and Pressures of Methane, Carbon Dioxide, and Propane Hydrates in Porous Media." *The Journal of Physical Chemistry B*, 106(4), 820-826.

Uchida, T., Ebinuma, T., Takeya, S., Nagao, J., and Narita, H. (2002). "Effects of pore sizes on dissociation temperatures and pressures of methane, carbon dioxide, and propane hydrates in porous media." *The Journal of Physical Chemistry B*, 106(4), 820-826.

Uchida, T., Lu, H., and Tomaru, H. (2004). "Subsurface occurrence of natural gas hydrate in the Nankai Trough area: Implication for gas hydrate concentration." *Resource Geology*, 54(1), 35-44.

Uchida, T., Takeya, S., Chuvilin, E. M., Ohmura, R., Nagao, J., Yakushev, V. S., Istomin, V. A., Minagawa, H., Ebinuma, T., and Narita, H. (2004). "Decomposition of methane hydrates in sand, sandstone, clays, and glass beads." *Journal of Geophysical Research: Solid Earth*, 109(B5).

Valenza, J. J., and Scherer, G. W. (2006). "Mechanism for salt scaling." *J. Am. Ceram. Soc.*, 89(4), 1161-1179.

Van Geet, M., Swennen, R., and Wevers, M. (2000). "Quantitative analysis of reservoir rocks by microfocus X-ray computerised tomography." *Sedimentary Geology*, 132(1), 25-36.

Vanorio, T., Prasad, M., and Nur, A. (2003). "Elastic properties of dry clay mineral aggregates, suspensions and sandstones." *Geophysical Journal International*, 155(1), 319-326.

Viggiani, G., And, ograve, E., Takano, D., and Santamarina, J. (2015). "Laboratory X-ray Tomography: A Valuable Experimental Tool for Revealing Processes in Soils."

Viggiani, G., Lenoir, N., Bésuelle, P., Di Michiel, M., Marello, S., Desrues, J., and Kretzschmer, M. (2004). "X-ray microtomography for studying localized deformation in fine-grained geomaterials under triaxial compression." *Comptes Rendus Mécanique*, 332(10), 819-826.

von Helmholtz, R. (1886). "Untersuchungen über Dämpfe und Nebel, besonders über solche von Lösungen." *Annalen der Physik*, 263(4), 508-543.

von Huene, R., Suess, E., Emeis, K.-C., Staff Scientist, L., Philip, D., and Garrison, L. E. (1987). "Ocean Drilling Program Leg 112 Preliminary Report, Peru Continental Margin." Ocean Drill. Program, College Station, Tex.

Waite, W. F., Santamarina, J. C., Cortes, D. D., Dugan, B., Espinoza, D. N., Germaine, J., Jang, J., Jung, J. W., Kneafsey, T. J., Shin, H., Soga, K., Winters, W. J., and Yun, T. S. (2009). "Physical properties of hydrate-bearing sediments." *Reviews of Geophysics*, 47(4), RG4003.

Walpole, L. (1969). "On the overall elastic moduli of composite materials." *Journal of the Mechanics and Physics of Solids*, 17(4), 235-251.

Walsh, J. (1965). "The effect of cracks on the compressibility of rock." *Journal of Geophysical Research*, 70(2), 381-389.

Wang, X., Wong, B. S., and Tui, C. G. "X-ray image segmentation based on genetic algorithm and maximum fuzzy entropy." *Proc., Robotics, Automation and Mechatronics, 2004 IEEE Conference on*, IEEE, 991-995.

Warzinski, R. P., Gamwo, I. K., Rosenbaum, E. J., Myshakin, E. M., Jiang, H., Jordan, K. D., English, N. J., and Shaw, D. W. (2008). "Thermal properties of methane hydrate by experiment and modeling and impacts upon technology." *Proceedings of the 6th International Conference on Gas Hydrates*Vancouver, British Columbia, CANADA.

Watanabe, N., Ishibashi, T., Ohsaki, Y., Tsuchiya, Y., Tamagawa, T., Hirano, N., Okabe, H., and Tsuchiya, N. (2011). "X-ray CT based numerical analysis of fracture flow for core samples under various confining pressures." *Engineering Geology*, 123(4), 338-346.

Watanabe, Y., Lenoir, N., Hall, S. A., and Otani, J. (2013). "Strain Field Measurements in Sand under Triaxial Compression Using X-Ray CT Data and Digital Image Correlation." *Advances in Computed Tomography for Geomaterials*, John Wiley & Sons, Inc., 76-83.

Wensrich, C., Kisi, E., and Luzin, V. (2013). "Non-contact stress measurement in granular materials via neutron and X-ray diffraction: theoretical foundations." *Granular Matter*, 15(3), 275-286.

Wensrich, C., Kisi, E., Zhang, J., and Kirstein, O. (2012). "Measurement and analysis of the stress distribution during die compaction using neutron diffraction." *Granular Matter*, 14(6), 671-680.

Westacott, R. E., and Rodger, P. M. (1998). "A local harmonic study of clusters of water and methane." *Journal of the Chemical Society, Faraday Transactions*, 94(23), 3421-3426.

Westbrook, G. K., Carson, B., J, M. R., and Party, L. S. *Proc., Proceedings, Ocean Drilling Program, Initial reports*, Ocean Drill. Program. College Station.

Westbrook, G. K., Carson, B., Musgrave, R., and others, A. "Proceedings of the Ocean Drilling Program, Vol. 146, Initial Reports Part 1, Cascadia Margin." Ocean Drilling Program.

Wildenschild, D., Vaz, C., Rivers, M., Rikard, D., and Christensen, B. (2002). "Using X-ray computed tomography in hydrology: systems, resolutions, and limitations." *Journal of Hydrology*, 267(3), 285-297.

Winters, W. "Stress history and geotechnical properties of sediment from the cape fear diapir, blake ridge diapir, and blake ridge." *Proc., Proceedings of the Ocean Drilling Program: Scientific results*, The Program, 421.

Winters, W. "Data report: effects of drying methods and themperatures on water content and porosity of sediment from the blake ridge " *Proc., Proceedings of the Ocean Drilling Program. Scientific results*, Ocean Drilling Program, 431-434.

Winters, W., Waite, W., Mason, D., and Kumar, P. (2008). "Physical properties of repressurized samples recovered during the 2006 national gas hydrate program expedition offshore India."

Winters, W., Walker, M., Hunter, R., Collett, T., Boswell, R., Rose, K., Waite, W., Torres, M., Patil, S., and Dandekar, A. (2011). "Physical properties of sediment from the Mount Elbert gas hydrate stratigraphic test well, Alaska North Slope." *Marine and Petroleum Geology*, 28(2), 361-380.

Wood, A. B. (1964). *A textbook of sound*, G. Bell and sons.

Wood, W. T., Gettrust, J. F., Chapman, N. R., Spence, G. D., and Hyndman, R. D. (2002). "Decreased stability of methane hydrates in marine sediments owing to phase-boundary roughness." *Nature*, 420(6916), 656-660.

Xu, W., and Ruppel, C. (1999). "Predicting the occurrence, distribution, and evolution of methane gas hydrate in porous marine sediments." *Journal of Geophysical Research: Solid Earth*, 104(B3), 5081-5095.

Yamamoto, K., and Dallimore, S. (2008). "Aurora-JOMEC-NRCan Mallik 2006-2008 Gas Hydrate Research Project Progress." *Fire in the Ice*, 8(3), 1-5.

Yamamoto, K., Inada, N., Kubo, S., Fujii, T., and Suzuki, K. (2012). "Pressure core sampling in the Eastern Nankai Trough." *Natural Gas & Oil*, 304, 285-4541.

Yamamoto, K., Terao, Y., Fujii, T., Ikawa, T., Seki, M., Matsuzawa, M., and Kanno, T. "Operational overview of the first offshore production test of methane hydrates in the Eastern Nankai Trough." *Proc., Offshore Technology Conference*, Offshore Technology Conference.

Yamano, M., Uyeda, S., Aoki, Y., and Shipley, T. (1982). "Estimates of heat flow derived from gas hydrates." *Geology*, 10(7), 339-343.

Yang, K., Kwan, A. L., Miller, D. F., and Boone, J. M. (2006). "A geometric calibration method for cone beam CT systems." *Med. Phys.*, 33(6), 1695-1706.

Yang, S., Cho, S., Lee, H., and Lee, C. (2001). "Measurement and prediction of phase equilibria for water+ methane in hydrate forming conditions." *Fluid Phase Equilibria*, 185(1), 53-63.

Yester, M., and Barnes, G. "Geometrical limitations of computed tomography (CT) scanner resolution." *Proc., Application of Optical Instrumentation in Medicine VI*, International Society for Optics and Photonics, 296-303.

You, K., Kneafsey, T. J., Flemings, P. B., Polito, P., and Bryant, S. L. (2015). "Salinity-buffered methane hydrate formation and dissociation in gas-rich systems." *Journal of Geophysical Research: Solid Earth*, 120(2), 643-661.

Yun, T. S., Fratta, D., and Santamarina, J. C. (2010). "Hydrate-bearing sediments from the Krishna− Godavari Basin: physical characterization, pressure core testing, and scaled production monitoring." *Energy & Fuels*, 24(11), 5972-5983.

Yun, T. S., Lee, C., Lee, J.-S., Bahk, J. J., and Santamarina, J. C. (2011). "A pressure core based characterization of hydrate-bearing sediments in the Ulleung Basin, Sea of Japan (East Sea)." *Journal of Geophysical Research: Solid Earth*, 116(B2), B02204.

Yun, T. S., Narsilio, G. A., and Carlos Santamarina, J. (2006). "Physical characterization of core samples recovered from Gulf of Mexico." *Marine and Petroleum Geology*, 23(9–10), 893-900.

Zatsepina, O. Y., and Buffett, B. (2001). "Experimental study of the stability of CO 2-hydrate in a porous medium." *Fluid Phase Equilibria*, 192(1), 85-102.

Zeng, Y., Payton, R., Gantzer, C., and Anderson, S. (1996). "Fractal dimension and lacunarity of bulk density determined with X-ray computed tomography." *Soil Sci Soc Am J*, 60(6), 1718-1724.

Zhang, G., Yang, S., Zhang, M., Liang, J., Lu, J., Holland, M., and Schultheiss, P. (2014). "GMGS2 expedition investigates rich and complex gas hydrate environment in the South China Sea." *Fire in the Ice*, 14(1), 1-5.

Zhong, Y., and Rogers, R. E. (2000). "Surfactant effects on gas hydrate formation." *Chemical Engineering Science*, 55(19), 4175-4187.

Zhou, H., Peng, X., Peth, S., and Xiao, T. Q. (2012). "Effects of vegetation restoration on soil aggregate microstructure quantified with synchrotron-based micro-computed tomography." *Soil and Tillage Research*, 124, 17-23.

VITA

LIANG LEI

Liang Lei was born in Xunxian, Henan Province, China. He received a B.A. in Civil Engineering from Tongji University, Shanghai, China in July 2009 and a M.A. in Geotechnical Engineering from Tongji University in March 2012 before coming to Georgia Tech to pursue a doctorate in Geotechnical Engineering. He is expected to receive his Ph.D. degree in Civil Engineering (Geosystems Engineering Group) in December 2016.